SETCOR
Conferences & Events

http://www.setcor.org/conferences/NANOTECH-DUBAI-2013

Nanotech Dubai 2013 International Conference Proceeding

CVD Grown Multilayer Graphene on Copper Film - A Versatile Approach.

Hatem Abuhimd[1], Mushtaq A. Dar[2], Mohamed Tarek Abdelaty[3]

[1]National Nanotechnology Center, King Abdulaziz City for Science and Technology
P.O Box 6086, Riyadh 11442, Saudi Arabia
habuhimd@kacst.edu.sa
[2] Center of Excellence for Research in Engineering Materials, Advanced Manufacturing Institute,
King Saud University, P.O Box 800, Riyadh 11421, Saudi Arabia
mdar@ksu.edu.sa
[3] Mechanical Engineering department, College of Engineering, Alfaisal University,
P.O. Box 50927, Takhasusi Road , Riyadh, Saudi Arabia
mabdelaty@alfaisal.edu

ABSTRACT

In recent years, research on graphene has attracted the scientific community mostly because of its interesting and unique properties and its atomic-scale thickness, in case of multilayer graphene. Graphene is considered to be the potential candidate for next generation electronic devices (1-4). Chemical vapor deposition (CVD) on the metal substrates attracted researchers in graphene growth. The technique is unique, inexpensive, high quality and viable for large area graphene growth. The as-grown graphene can be transferred to other substrates (5). In this work, copper foil was used as a catalyst for graphene preparation.

In the experimentation process, Cu foil (9 µm thick, 99.99%) was purchased from MTI, USA as the substrate for graphene growth. Prior to use the samples were cleaned ultrasonically in acetone, ethanol and double distilled water. The samples were loaded into the CVD quartz tube. The temperature set for the Cu substrate was 1000 °C in 40 min in an ambient gas atmosphere with hydrogen (H_2) (99.99% purity) and argon (Ar) (99.99% purity) to avoid oxidation of the Cu.

Then carbon containing gas (CH_4) (99.99%) purity) was flown for 5 min. Finally, the Cu substrate is cooled down to room temperature. The synthesized graphene layers on the Cu was investigated by X ray diffraction (XRD), Scanning electron microscopy (SEM), transmission electron microscopy (TEM), atomic force microscopy (AFM) and Raman microscopy. The results show that the grain size of the resulting graphene obtained was found to rise up to 50 microns (Fig. 1).

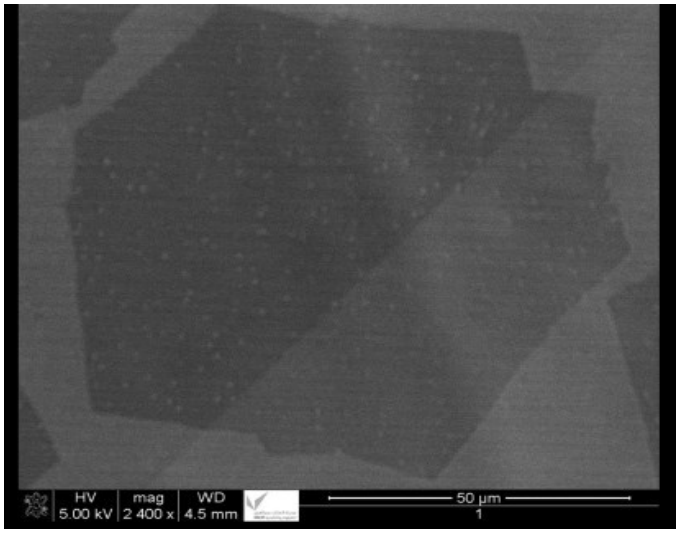

Fig. 1. A representative SEM image of the CVD grown graphene on copper.

Raman spectroscopy analysis confirmed that multilayer graphene was formed, and were almost defect free. AFM measurements were employed to understand the surface of the grown graphene (Fig. 2). The Average root mean square (RMS) roughness of Graphene on Cu foil surface as estimated from AFM is ~22.74 nm.

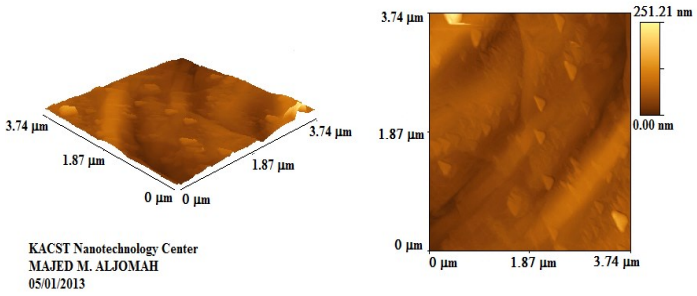

Fig.2 AFM image of the multilayer graphene sheets

References:

1. M. Batzill, Surface Science Reports, 67 (2012) 83–115.
2. Y. Li, M. Li, T. Gu, F. Bai, Y. Yu, M. Trevor, Y. Yu, Appl. Surf. Sci., In Press.
3. E. Kibena, M. Mooste, J. Kozlova, M.Marandi, V. Sammelselg, K. Tammeveski, Electro. Communications, 35 (2013) 26–29.
4. F. Hauquier, D.Alamarguy, P. Viel, S. Noël, A. Filoramo, V. Huc, F. Houzé, S. Palacin, App. Surf. Sci. 258 (2012) 2920– 2926.
5. Z. G. Wang, Y. F. Chen, P.J. Li, X. Hao, Y. Fu, K. Chen, L.X. Huang, D. Liu, Vacuum 86 (2012) 895-898

SETCOR International Conference on Nanotechnology Dubai 2013 (NANOTECH DUBAI 2013) 28-30 October, 2013. Dubai, United Arab Emirates

Experimental study of membrane properties on gas permeation in γ-alumina macroporous ceramic membranes

***Presenting Author**:* Mohammed Nasir Kajama, Email: *mohd_nasiru@yahoo.com,* Centre for Process Integration and Membrane Technology, (CPIMT), School of Engineering, The Robert Gordon University, Aberdeen, AB10 7GJ. United Kingdom

***Corresponding Author**:* Professor Edward Gobina, Email: *e.gobina@rgu.ac.uk,* Centre for Process Integration and Membrane Technology, (CPIMT), School of Engineering, The Robert Gordon University, Aberdeen, AB10 7GJ. United Kingdom

Abstract

A 6000nm γ-alumina macroporous ceramic membrane was repaired with boehmite solution (ALOOH) using the repeated dip-coating method. The permeance of hydrogen and carbon dioxide were obtained through the membrane against average pressure at room temperature for the support membrane, cracked membrane, first and second dip membrane. The permeance of the support membrane ranged between 1.50 – 3.04 x 10^{-7} mol m^{-2} s^{-1} Pa^{-1}. However, due to a crack that occurred during the removal of the membrane from the reactor, the permeance increased to 2.96 – 5.82 10^{-7} mol m^{-2} s^{-1} Pa^{-1}. After exposing boehmite solution to the membrane, the surface was improved to some degree and surface cracks are also lowered. This also decreased the permeance to 1.26 – 3.39 x 10^{-8} mol m^{-2} s^{-1} Pa^{-1} after the second dip. The permselectivities of CO_2 over H_2 at room temperature was also obtained which were higher than the Knudsen selectivity.

Keywords: Ceramic membranes, Gas permeation, Hydrogen and Carbon dioxide selectivity.

1.0 Introduction

Carbon dioxide is one of the many greenhouse gases which contributes to global warming. Membrane technology has been suggested as a substitute to the use of conventional separation processes (e.g. dehydration, gas adsorption, distillation among others) due to their unique attributes such as thermal and mechanical stability, as well as harsh chemical resistance [1, 2]. The employment of inorganic membranes in the industry has extended the application of membranes for hydrogen production, CO_2 recovery as well as H_2S removal from associated gas feed streams because of their simplicity and low energy requirement [3].

There are several methods for porous membrane modification including; dip-coating, chemical vapour deposition, and pulsed layer deposition [4, 5, 6]. Out of the mentioned modification methods, dip-coating method has many merits over the other methods such as its simplicity, uniform surface and the ability of controlling the pore structure of the membrane [4]. However, a lot of research is still needed to examine membrane modification through dip-coating method in order to elucidate the morphological effects of dip-coated membranes. Membranes defects are formed during preparation stages. It can be formed either during dipping, drying, calcination process and sealing [7] or even during the process of inserting and removing it from the reactor. Any defect in a macroporous membrane (pore diameter > 50 nm) can be regarded as a crack. For example, a defect is considered in the presence of super-micropores (0.7 nm < pore diameter < 2 nm) instead of ultra-micropores (pore diameter < 0.7 nm) [7]. It is known that any amount of defect on the membrane can significantly lower the membrane selectivity.

Lambropoulos et al. [8] repaired γ-alumina and silica membranes at 573 K by CVD process with a $TEOS/O_3$ counter reactant configuration. The defect was characterised with a permeability technique and a novel mercury intrusion. However, Gopalakrishnan et al. [9] applied a hybrid processing method for hydrogen-selective membrane preparation. They applied a primary sol-gel silica layer for the CVD zone thickness reduction, and a CVD modification with tetramethoxysilane (TMOS) and O_2 at 873 K. After which they only examined H_2/N_2 selectivity to be 2300 at 873 K. Pejman et al. [4] modified the surface of ceramic supports to facilitate the deposition of defect-free overlying micro and mesoporous membrane. They investigated the effects of dipping time, heating rate, and number of coated layers on microstructure of the modified layers in their study. They have achieved a smoother surface and the cracks size was reduced dramatically after two dip-coating steps.
In this paper, we repaired a crack on a γ-alumina ceramic membrane with boehmite solution (ALOOH), also carbon dioxide separation and the effects of permeation properties such as; permeation pressure was examined.

2.0 Experimental

A γ-alumina macroporous ceramic membrane supplied by Ceramiques Techniques et Industrielles (CTI SA) France, consisted of (77% α-alumina + 23% TiO_2) with an average pore diameter of 6000 nm was used. The membrane used has 19.8 mm and 25 mm internal and outer diameter respectively, and a permeable length of 318 mm. The pressure applied was between 0.05 to 4 bar at room temperature. Figs. 1 and 2 shows a SEM image of inside and outside surface of the porous ceramic membranes. The membrane's structure can be distinguished which was defect-free before the 1st dip. An SEM of the cross section of the same membrane is also shown in Fig. 3. During the removal of the membrane from the reactor; the membrane was cracked Fig. 4 i.e. after gas permeation before the modification.

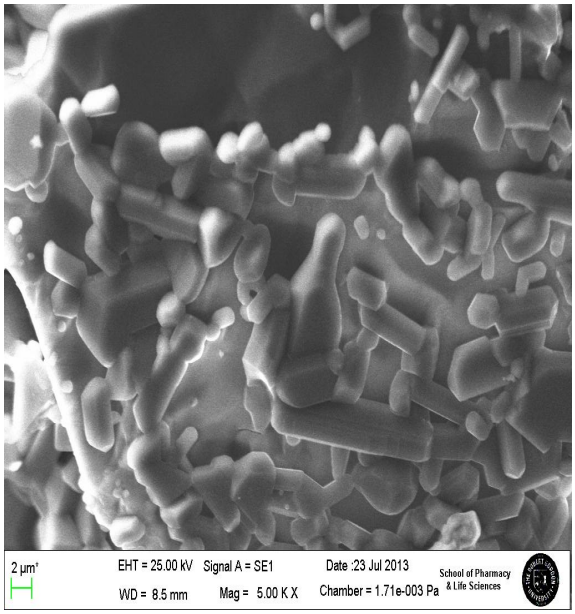

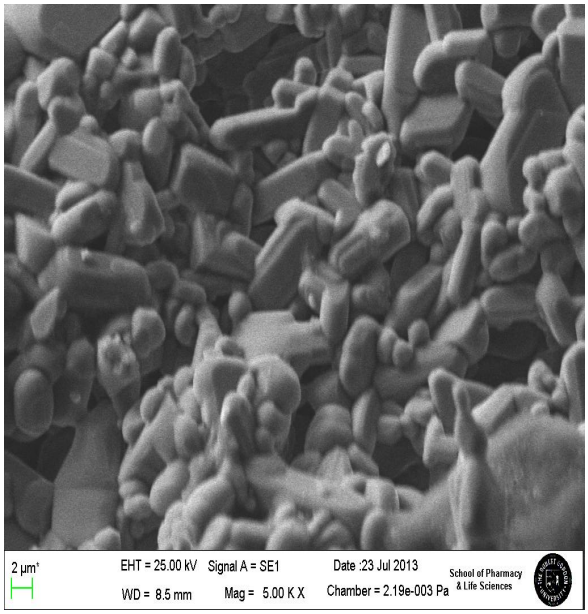

Figure 1: SEM image of the inside surface. **Figure 2:** outside surface of ceramic membrane

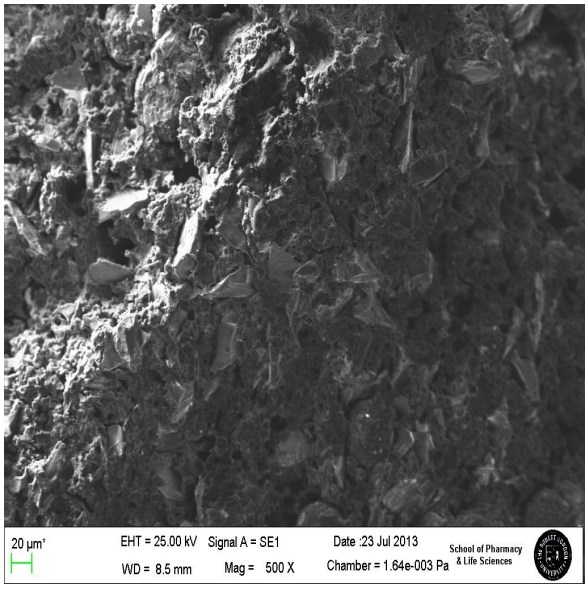

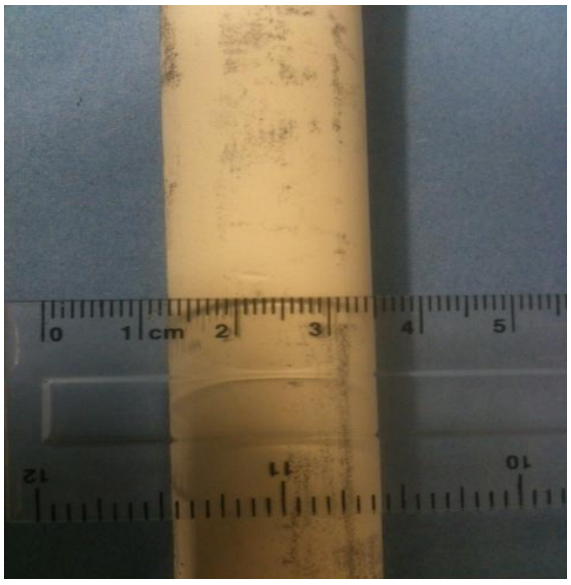

Figure 3: SEM image of the cross section of the membrane. **Figure 4:** Pictorial view of the cracked membrane.

In order to repair the defected surface of the substrate a 36g/1000L boehmite sol was used as γ-alumina source. A dip-coating method was applied to repair the defected membrane. The internal surface of the coarse alumina tube membrane was exposed to boehmite solution for 30 minutes. After this the membrane was air-dried overnight and then heat-treated using the temperature profile shown in Fig. 5. The dipping-drying firing procedure was repeated in order to achieve the required γ -alumina layer on the coarse support. The prepared membrane, glazed at each end, was sealed within the stainless steel reactor using graphite seals.

Single gas permeation measurements were carried out for gas components (H_2 and CO_2) at room temperature using the experimental setup shown in Fig. 6 with the retentate valve fully open to the fume

cupboard. The permeate flow tube was connected to the flowmeter to record gas flow rate. Gas permeance was obtained from the following expression;

$$Q = \left(\frac{q}{A_s \Delta P}\right) \quad (1)$$

Where Q is the Permeance (mol m^{-2} s^{-1} Pa^{-1}); q is the molar flow (mol/sec); A is the membrane area (m^2); and ΔP is the pressure difference (Pa) across the membrane.

The permselectivity of the membrane was also obtained using equation (2);

$$S_{ij} = Q_i/Q_j \quad (2)$$

Where S_{ij} is the permselectivity of i to j; Q_i is the permeance of i (mol m^{-2} s^{-1} Pa^{-1}); Q_j is the permeance of j (mol m^{-2} s^{-1} Pa^{-1}).

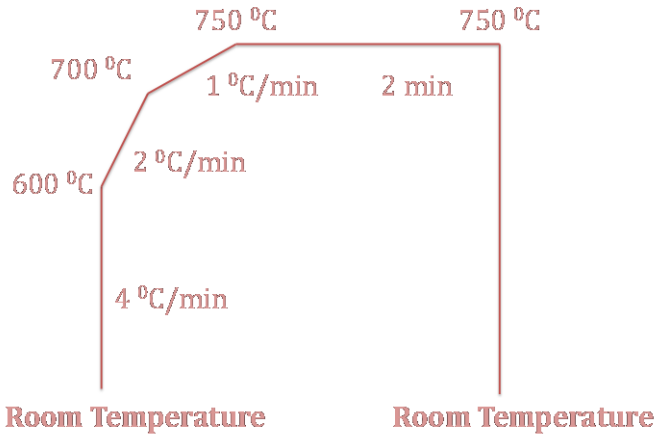

Figure 5: Membrane's Heat-Treatment Profile. **Figure 6:** Stainless Steel Tubular Membrane Reactor.

3.0 Results and Discussion

Fig. 7 shows the results of carbon dioxide permeance through the multilayered alumina membrane against average pressure at room temperature for the support membrane, cracked membrane, first and second dip repaired with boehmite solution stages. It can be seen that the permeance of the support is 1.50 – 3.04 x 10^{-7} mol m^{-2} s^{-1} Pa^{-1}. However, due to the crack which occurred during the removal of the membrane from the reactor, the permeance increased to 2.96 – 5.82 10^{-7} mol m^{-2} s^{-1} Pa^{-1}. After exposing boehmite solution to the membrane, the surface was improved to some degree, surface cracks are also lowered, and the permeance decreased to 1.26 – 3.39 x 10^{-8} mol m^{-2} s^{-1} Pa^{-1} after the second dip which is almost parallel to the x-axis which indicates the applicability of Knudsen diffusion mechanism.

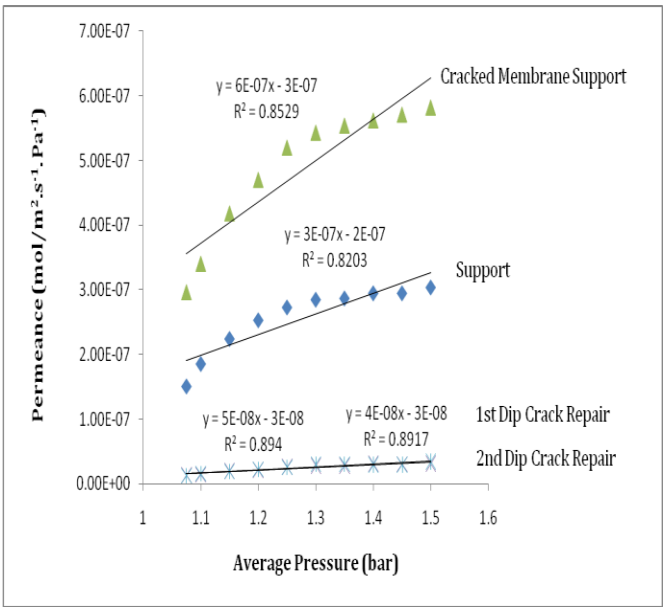

Figure 7: Permeance Against Average Pressure for Carbon Dioxide at Room Temperature.

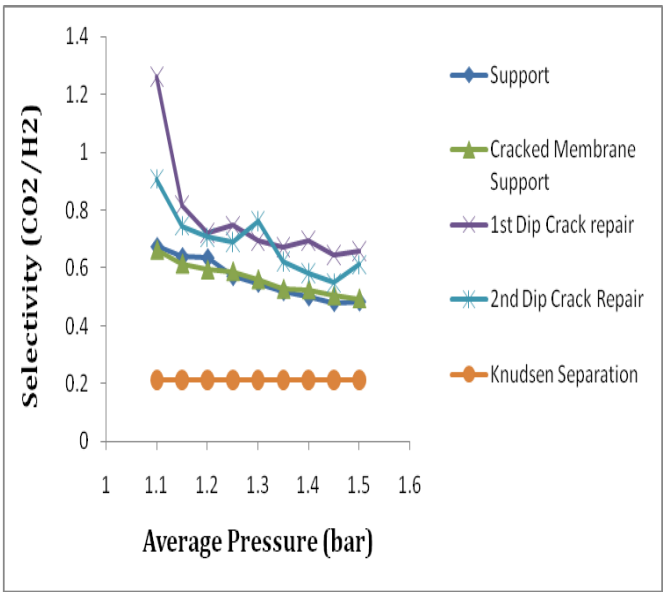

Figure 8: Selectivity of CO_2/H_2 Against Average Pressure at Room Temperature

The permselectivities of CO_2 over H_2 at room temperature is shown in Fig. 8. It can be seen that the selectivities obtained are higher than the Knudsen selectivity. After exposing the support to the boehmite solution the permeance decreased (Fig. 7), although a significant increase in the selectivities (Fig. 8) was achieved at ambient temperature which corroborates with the result obtained by Koutsonikolas et al. [6] on the chemical vapour infiltration **(**CVI) modification method for H_2/N_2, H_2/CO_2 and H_e/N_2 at 300 ^{0}C. An increase in permselectivities of CO_2/H_2 is expected significantly at temperatures above 25 ^{0}C and these would have a substantial energy efficiency benefit for ceramic membrane processes.

4.0 Conclusions

A simple but effective technique to modify nanostructure ceramic membranes which involves dip-coating method was studied and involved the use of boehmite solution to modify the membrane. Several parameters such as dipping time, number of coating, heating rate on the nanostructure were investigated. A high temperature heat-treatment was applied in order to repair defects in the commercial membranes, and to improve the permselectivity of these membranes above Knudsen regime selectivity. Single gas permeation tests were used to examine the permeance of the membrane. After the first and second modifications with boehmite solution, permeance decreased significantly which indicates the presence of Knudsen diffusion mechanism.

Acknowledgements

The authors gratefully acknowledge Petroleum Technology Development Fund (PTDF) Nigeria for funding this research, and School of pharmacy & Life Sciences RGU for the SEM results.

References

[1] R. P. Singh, J. D. Way, K. C. McCarley, Development of a model surface flow membrane by modification of porous Vycor glass with a fluorosilane, Ind. Eng. Chem. Res (2004); 43: 3033-3040.
[2] LI. Anwu, Z. Hongbin, GU. Jinghua, X. Guoxing, Preparation of γ-Al_2O_3 composite membrane and examination of membrane defects, Science in China (Series B) (1997); 40(1): 31-36.
[3] Y. Yildirim, R. Hughes, The efficient combustion of O-xylene in a Knudsen controlled catalytic membrane reactor, Trans IChemE (2002); 80(Part B): 159-164.
[4] A. N. Pejman, B. A. Akbar, J. Elham, P. Majid, A. A. Masoumeh, An optimum routine for surface modification of ceramic supports to facilitate deposition of defect-free overlaying micro and meso (nano) porous membrane, Iran. J. Chem. Eng., 30, 3 (2011) 63-73.
[5] J.M. Benito, A. Conesa, F. Rubio, M.A. Rodr´ıguez, Preparation and characterization of tubular ceramic membranes for treatment of oil emulsions, Journal of the European Ceramic Society 25 (2005) 1895-1903.
[6] D. Koutsonikolas, S. Kaldis, G.P. Sakellaropoulos, M. H. V. Loon, R. W.J. Dirrix, R. A. Terpstra, Defects in microporous silica membranes: Analysis and repair, Separation and Purification Technology, 73 (2010) 20-24.
[7] D. Koutsonikolas, S. Kaldis, G.P. Sakellaropoulos, M. H. V. Loon, R. W.J. Dirrix, R. A. Terpstra, Defects in microporous silica membranes: Analysis and repair, Separation and Purification Technology, 73 (2010) 20-24.
[8] A. Lambropoulos, G. Romanos, Th. Steriotis, J. Nolan, F. Katsaros, E. Kouvelos, G. Charalambopoulou, N. Kanellopoulos, Application of an innovative mercury intrusion technique and relative permeability to examine the thin layer pores of sol–gel and CVD post-treated membranes, Microporous and Mesoporous Materials, 99 (2007) 206-215.
[9] S. Gopalakrishnan, Y. Yoshino, M. Nomura, B. N. Nair, S-I. Nakao, A hybrid processing method for high performance hydrogen-selective silica membranes, Journal of Membrane Science, 297 (2007) 5-9.

Flexible InGaAs based Solar Cells using controlled spalling technology

Abdulrahman M. Albadri*, Ibrahim A. Alhomoudi, and Abdelmajid Salhi
National Nanotechnology Center
King Abdulaziz city for science and technology, P. O. Box 6086, Riyadh, Saudi Arabia
* email: aalbadri@kacst.edu.sa

Abstract
In this work, we developed flexible single junction (SJ) InGaAs solar cells using controlled spalling technology. The spalling process was implemented by applying a metal stressor to predetermine the fracture thickness, and a handling polyimide tape to assure spalling controllability. Upright and inverted structures were processed and compared against the bulk structure. A comparable efficiency of 23.5% was obtained for the flexible cells under one sun intensity.

1. Introduction

Flexible solar cells have been of a much interest due to their low cost and weight. In contrast to conventional solar cells, flexible cells utilize a very thin layer (3-4 um) of the base material (GaAs) that has high absorption properties. Over half of the total cost of cell fabrication is due to the substrate material which is mainly used for epitaxial growth and not part of photon absorption. This motivates the use of high efficiency thin film solar cells by exfoliating them from the substrate wafer. There have been many techniques to lift-off the thin GaAs film from the substrate wafer such as long time used epitaxial lift-off [1] or recent controlled spalling technology [2]. A combination of high efficiency and less utilized materials is crucial in achieving the roadmap of less than $1/W cost for terrestrial solar systems. In addition to that, satellite systems mandate the use of light weight solar panels. A very reliable technique (Controlled spalling technology) to obtain thin films with high uniformity and reproducibility has been considered. Controlled spalling technology (CST) allows the kerf-free removal of thin crystalline Si, Ge and III-V layers at room-temperature [3].

Here we present the use of controlled spalling technology to obtain a flexible SJ InGaAs based solar cell. We first grew the epitaxial layers of the SJ InGaAs structure on Ge wafer. After that, we apply the spalling technique to get the thin film out of the Ge wafer. There were two approaches considered in this work. One is the upright conventional structure where the spalled film needs to be bonded to either rigid or flexible substrate after spalling. The second approach is to grow an inverted structure so that the spalled film utilizes the Ni/polyimide tape stack as back contact/handling substrate without Ni removal.

2. Experimental

a. Controlled spalling technology

This technique requires a stressor layer (metal) at a predetermined depth by manipulating the thickness and stress. Initiating a specific orientation to control the spalling process has been used to improve the spalling process and hence the spalled surface smoothness. Fig.1 shows a schematic representation of the spalling process of a thin semiconductor film (could be a complete PV structure).

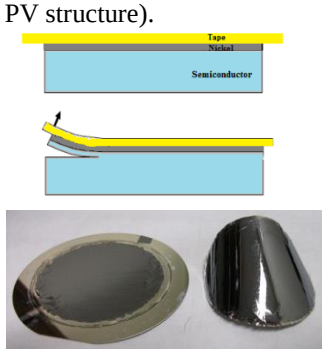

Fig. 1. Schematic illustration for the spalling process along with successful spalled film.

b. SJ InGaAs based solar cell structure

Both upright and inverted SJ InGaAs structures have been fabricated to demonstrate flexile solar cells [4]. Fig.2 illustrates an inverted SJ InGaAs based solar cell structure that have been grown for the purpose of spalling process on 4”

diameter p-type Ge (100) wafer with 180 µm thick using the Veeco K475 MOCVD system. This can be realized by growing a perfectly-lattice matched structure eliminating the most common mismatch-related dislocations. The layer stacks' uniformities and free-dislocations were verified by X-ray diffraction, Photoluminescence, and AFM. SIMS analysis was performed to characterize the doping concentration throughout the different layers.

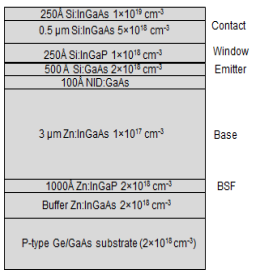

Fig. 2. Schematic illustration of the SJ InGaAs solar cell structure.

3. Results and discussion

A SJ InGaAs bulk cell was processed and high efficiency of about 23.5% was achieved, and the IV curve along with EQE plot are shown in Fig. 3.

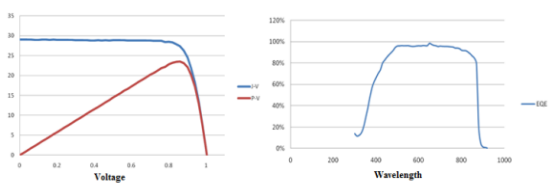

Fig. 3. IV and EQE of the SJ InGaAs solar cell.

A comparison between the upright and the inverted structures is outlined in Table 1.

Table 1. Upright versus inverted structures

	Inverted structure	Upright structure
Growth process	Emitter suffers long temp. process besides Zn diffusion	Emitter is last grown, so it is optimized
Post process temperature	< 200 °C for contact alloying when polyimide tape is used	The tape is removed, so contacts can be alloyed at standard alloying temp. (~400 °C)
Back contact	Ni stressor used as back contact	Conductive silver based epoxy
Support substrate	Handling Polyimide tape works a support layer	Bonded to Si substrate or flexible polymer substrate

As for the upright structure, the film was successfully exfoliated then bonded on a host silicon wafer and the process is outlined in Fig. 4.

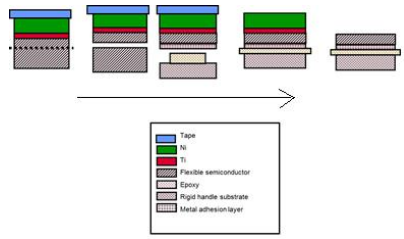

Fig. 4. Spalling and bonding process of SJ upright structure.

It was examined at 1 sun and an efficiency of ~20% was achieved. The Jsc is lower due the use of wider fingers for CPV applications. Note that this process requires a removal of the Ni stressor and the polyimide tape. On the other hand, an inverted InGaAs structure was processed where the growth sequence is reversed. In this case the Ni film can be exploited as a back contact and the polyimide tape helps in handling the thin cell. A comparable efficiency of 23 % to the bulk structure was successfully obtained

4. Conclusions

Thin films of InGaAs were developed using controlled spalling technology. Two structures were considered for the flexible cell illustration. Upright and inverted structure were successfully processed and tested. An efficiency of ~23.5% for the bulk and the spalled structure was verified.

5. References

[1] J. J. Schermer, et al., "Epitaxial lift-off for large area thin film III/V devices," *Phys. Stat. Sol. (a)*, vol. 202, pp. 501–508, 2005

[2] Z. Suo and J. Hutchinson, Int. J. Solids Struct., vol. 25, pp. 1337, (1989).

[3] S. Bedell, et al., IEEE J. Photovoltaics, vol. 2, p. 141, (2012).

[4] J. Geisz, et al., Appl. Phys. Lett., vol. 91, p. 023502, (2007).

Evaluation of antibiotics as the target-sensitive component of nanobiomarkers

Alexander V. Beskorovaynyy, Andrei A. Novikov, Pavel A. Gushchin, Evgeniy V. Ivanov

Gubkin Russian State University of Oil and Gas, 65 Leninsky prospect, Moscow, Russia
ivanov166@list.ru

Introduction

Gold nanorods attract research interest due to its tunable longitudinal plasmon resonance (Figure 1).

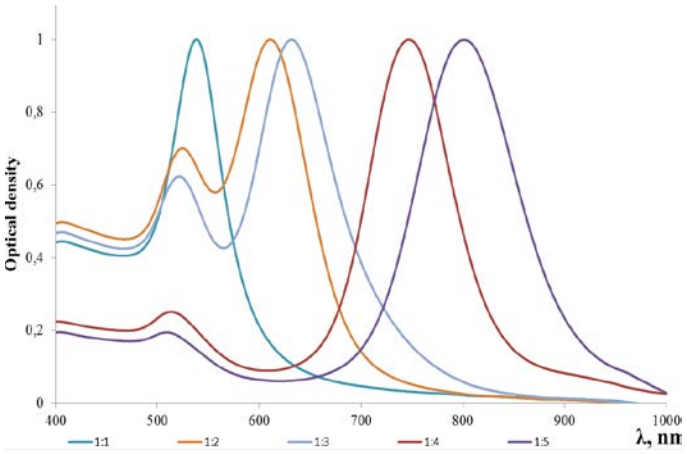

Figure 1. Optical density spectrum for gold nanorods wis different aspect ratio (from 1:1 to 1:5)

Due to their unique optical properties, nanorods are widely used in biomedical studies for gene delivery, imaging of cells, photothermal therapy and biosensing [1]. Gold nanoparticles demand to be conjugated in order to provide specificity to cancer cells or pathogenic bacteria. Usually this is done by coupling nanoparticles with antibodies to specific receptors, but the high cost of antibodies severely constrains the usage of such conjugates [2]. However, nanoparticles could be coupled with the much cheaper alternative – various antibiotics [3, 4]. Antibiotic-coupled gold nanorods are the potent therapeutic antimicrobial agents and promising biosensors [5].

Experimental

In our work, gold nanoparticles of different shape (see pictures 1 and 2) were coupled with various antibiotics via PEGylation and consequent NHS/EDC-promoted reaction.

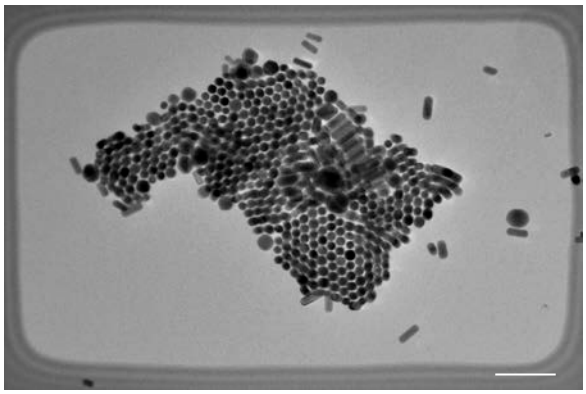

Picture 1. Gold nanospheres (bar is 200 nm)

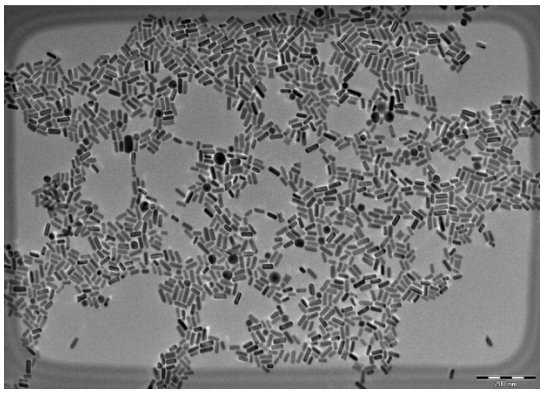

Picture 2. Gold nanorods wis aspect ratio 3:1 (bar is 200 nm)

The gold nanoparticles conjugation with penicillin, chloramphenicol and ciprofloxacin was performed *via* HS-PEG-NH_2 mediated coupling, and the gold nanoparticles conjugation with amikacin was performed by HS-PEG-COOH. The structure formulae of antibiotics used are shown on Figure 2.

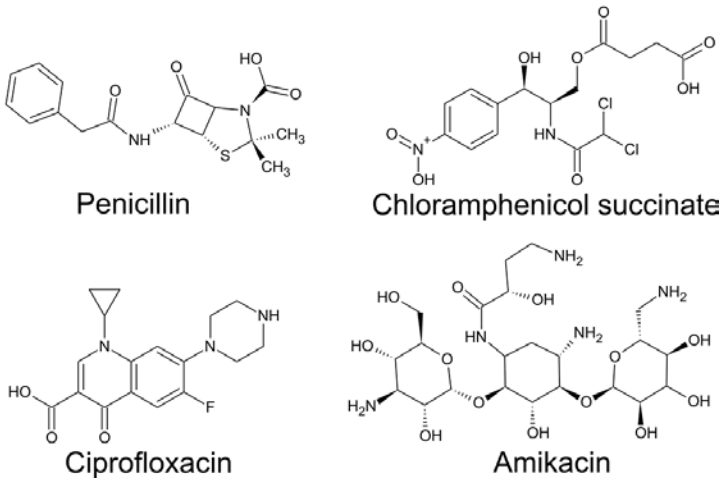

Figure 2. Structure formulae of used antibiotics.

Nanobiosensors were synthesized according to Figure 3 and evaluated for the contrasting of *Escherichia coli* and *Staphylococcus aureus.*

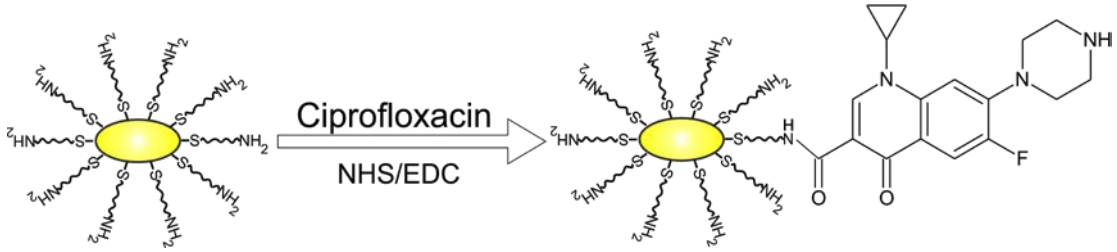

Figure 3. Schematic illustration of nanobiosensor producing.

Results and discussion

All of the obtained antibiotic-coupled nanoparticles have the affinity for bacterial cell wall, except the penicillin-conjugated ones (see picture 4).

Conjugates with penicillin are unable to detect *S. aureus* because they were destroyed by the bacterial penicillinase. Thus, antibiotic-coupled gold nanoparticles could be used not only for the pathogen contrasting, but also for the express evaluation of bacterial susceptibility to certain anibiotics.

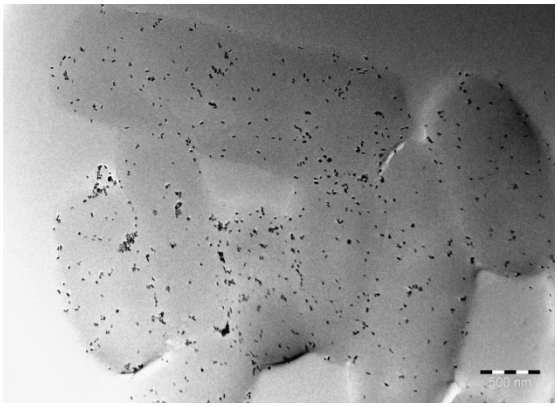

Picture 4. E.coli cells contrasted by nanoconjugates of Au nanorods and amikacin.

Aknowlegments

This work was supported by Ministry of Education and Science of the Russian Federation (project 11.G34.31.0070), and also by the Russia president grant (project 14.124.13.7577-MK).

References

[1] L. Shi et al., Angewandte Chemie. 125, 23 (2013) 6127-6130.
[2] I.-H. Cho, J. Irudayaraj, International journal of food microbiology. 164, 1 (2013) 70-75.
[3] L. Rastogi, A.J. Kora, Materials Science and Engineering: C. 32, 6 (2012) 1571-1577.
[4] S. Karthick et al, Innovare Journal of Medical Science. 1, 2 (2013) 7-11.
[5] W.-C. Huang, P.-J. Tsai, Y.-C. Chen Nanomedicine. 2, 6 (2007) 777-787.

Experimental Design and Artificial Neural Network Metamodel for the Gas-Phase, One-Step Acetone Self-Condensation Over Novel Composite Catalysts of Ruthenium/Activated Charcoal/Nano-Zinc Oxide

Hatem Abuhimd[1], **Abdulaziz A. Bagabas**[2]
[1]National Nanotechnology Center, King Abdulaziz City for Science and Technology
P.O Box 6086, Riyadh 11442, Saudi Arabia
habuhimd@kacst.edu.sa
[2]Petrochemicals Research Institute, King Abdulaziz City for Science and Technology
P.O Box 6086, Riyadh 11442, Saudi Arabia
abagbas@kacst.edu.sa

Abstract

Acetone (dimethyl ketone, DMK) self-condensation is industrially important for the synthesis of many fine chemicals such as mesityl oxide (MO), methyl isobutyl ketone (MIBK), phorone (PH), isophorone (IPH), and diisobutyl ketone (DIBK) [1]. Several of palladium- and platinum-based multifunctional catalysts have been investigated extensively for both the liquid- and gas-phase processes [2]. However, to the best of our knowledge, ruthenium-based multifuntional catalysts have been examined by Bagabas and his co-workers for the first time in the gas-phase, one-step DMK self-condensation to methyl isobutyl ketone (MIBK) [3]. They prepared novel composite catalysts by mechanical mixing of commercially available 5 wt% nano-ruthenium supported on activated charcoal (Ru/AC) with their lab-synthesized *nano*-zinc oxide (*n*-ZnO) at different weight ratios. They performed DMK self-condensation under atmospheric pressure, in a tubular glass fixed-bed micro-reactor, under DMK and H2 continuous flow, at temperature in the range of 523 to 648 K. Addition of *n*-ZnO to Ru/AC resulted in a pronounced increase in the degree of dispersion of Ru and in the acidic/basic sites concentration ratio. For the one-step synthesis of MIBK at 623 K, the composite catalyst with 2.5 wt % Ru loading was an active and selective bi-functional composite catalyst with balanced acid/base and hydrogenation properties. At 523 K, isopropyl alcohol, product of DMK-direct hydrogenation, was produced in high selectivity for all investigated composite catalysts. They found that gas-phase DMK self-condensation into MIBK was a function of catalyst identity, reaction temperature, DMK flow rate, and hydrogen (H_2) flow rate [3].

In this study, we carried out a practicality assurance of MIBK by an experimental design and an artificial neural network (ANN) meta-model. Our objective was to evaluate all input variables theoretically and experimentally to find out the statistically significant ones.

The proposed methodology had two distinct stages. Stage 1 focused on building a meta-model of the process using the experimental data and an artificial neural network (ANN) technique, which is a multilayer perceptron (MLP). The meta-model in this context captures an overarching behavior of the process by broadly encompassing the data available at hand. Using the meta-model, stage 2 generated multiple runs for a full-factorial experimental design.

Artificial Neural Network Design Phase:

The following steps make up the stage 1 of the research methodology:

- Eliminating experimental data records with missing data.
- Normalizing the values of each process control variable in [0, 1] range. This transformation brings all control variables into the same numerical range to give equal weight to each variable in clustering process described below.
- Using the records retained in the previous step, train the neural networks for estimating the performance variables; given that control variable vectors are most likely positioned densely in the input space, the neural networks are likely to learn the mapping between process inputs and outputs accurately.
- Computing the estimation errors, i.e., the paired differences between the actual process outputs and neural-network-estimated process responses.
- Using the records retained in the previous step, retrain the neural networks for estimating the process outputs; these trained neural networks serves as computer models of the process.
- Computing the paired difference between the actual process outputs and the neural-network estimated process responses.

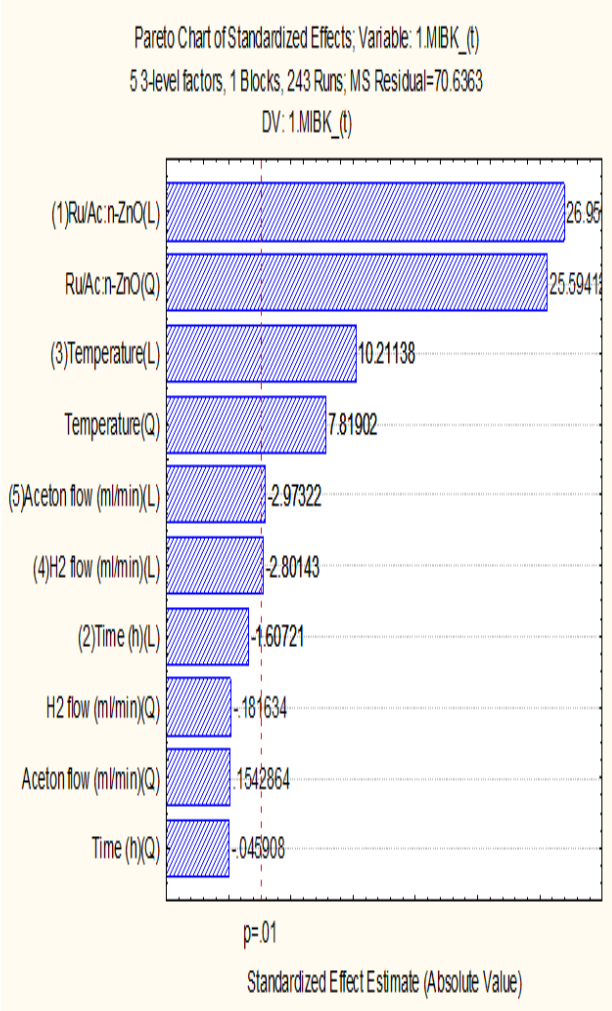

Figure 1: Pareto Chart of the statistical Analysis

- Conducting the t-test on paired differences with a level of significance of α = 0.05, which can be tightened or relaxed if necessary. H0:μd = 0 and H1:μd > 0, where μd is the mean of the paired differences. Compute t0, the t-statistic for the paired difference. If |t0| > tα/2, then reject H0; otherwise we fail to reject H0, which would statistically mean no evidence for the difference between the behavior of the meta-model and that of the actual process.

Design of Experiment (DOE) Phase:

After building the multi-layer perceptron based process meta-model, we performed a design of experiment study. The following steps were used to conduct the study:

- Finding the min-, mid- and max-points of each input variable for the records used in training the neural networks in phase 1.
- Creating the three level settings for the DOE using the min-, med-, and max-
- Points of the input variables.
- Conducting DOE analysis using the DOE runs.

The obtained results herein showed that the catalytic performance depended on the composite catalyst identity, reaction temperature, DMK flow rate, and H_2 flow rate. The composite catalyst identity (the Ru/AC:*n*-ZnO ratio) was the most significant factor, followed by temperature, DMK flow rate, and H_2 flow rate. Time did not prove to be a significant factor, as can be observed from the Pareto chart in figure 1.

Acknowledgement

The authors would like to acknowledge King Abdulaziz City for Science and Technology for funding this work.

References

[1] Rodrigues, A. C. C.; Monteiro, J. L. F., Appl. Catal. A, 362 (2009), 185-192.
[2] Unnikrishnan, R.; Narayanan, S., J. Mol. Catal. A Chem. 144 (1999) 173.
[3] Bagabas, A.; Mostafa, M.; Al-Rabiah, A; Akhmedov, V., US Patent 8,110,708 B2 (2012).
[4] Abuhimd, H., Uddin, G. M., Zeid, A., Jung, Y. J., & Kamarthi, S. (2013). *T. I. J. Adv. Man. Tech.*, *64*(1-4), 545-553.

Nanotech Dubai 2013: Nano for Better
Conference and Exhibition
28-31 October, 2013, Dubai, UAE

Polymer-Graphene Nanocomposites: Effect of the Matrix and Processing Conditions

Ahmed A. Abdala and Chris Macosko

Department of Chemical Engineering, the Petroleum Institute, Abu Dhabi, UAE

Permanent Address: Faculty of Petroleum and Mining Engineering, Suez Canal University, Suez, Egypt

Authors' e-mails: aabdala@pi.ac.ae

ABSTRACT

The combination of graphene extraordinary mechanical, thermal, and electrical properties and the ability to disperse graphene in various polymer matrices has led a new era of polymer nanocomposites. Although, incorporation of graphene into polymer matrices leads to a substantial enhancement in the mechanical, electrical, and thermal properties, the level of enhancement is greatly affected by the degree of graphene dispersion into the polymer matrix and the nature of the interface between graphene and the matrix. These two factors are controlled by the graphene-matrix compatibility (the polarity of the matrix) and the processing method. Examples that demonstrate the effects of these two parameters on graphene dispersion as well as the morphological, mechanical, and electrical are presented and discussed. To study the effect of the matrix chemistry, we used a nonpolar matrix, linear low density polyethylene, and its maleated analogous. The effect of the processing method (melt versus solvent blending) on the dispersion of graphene into the matrix and the composite properties are also analyzed. Our results prove that solvent blending improves the graphene dispersion provides better enhancement of the mechanical and electrical properties. Moreover, the functionalization of the PE matrix promotes the dispersion of graphene into the matrix and yield a higher improvement in the mechanical properties.

INTRODUCTION

Polymers have a range of attractive properties such as low density, softness, elasticity, high toughness, ease of processing, corrosion resistance, electrical and chemical insulating properties. However, many applications require enhanced or additional functional properties such as strength and stiffness, dimensionally stability, electrical, and thermal conductivity, thermal stability, flame retardancy, and diffusion resistance. One way to enhance polymers in order to meet these special application requirements is to incorporate filler into the polymer matrix, i.e. forming polymer composites. In particular,

polymer nanocomposites which include the incorporation of nanosize fillers into the polymer matrix can enhance mechanical properties, thermal stability, electrical and thermal conductivity, and barrier properties of polymers. Examples of nanofillers include Layered silicate (clay), nanosize carbon black and carbon fibers, carbon nanotubes, and graphene.

Graphene is a single layer of carbon atoms arranged in a honeycomb lattice which represents the 2-D carbon allotrope. Graphene is considered as the mother of all carbon based materials of all other dimensionality, e.g. the 0-D bukyminister, the 1-D carbon nanotube, and the 3-D graphite (Geim, 2007). Although graphene has been known since 1947, attempts to its experimental isolation was faced with experimental difficulties and misbelieve that it will be thermally unstable due to its low thermal stability due to its atomic thin structure. Geim and Novoselov have provided the first demonstration for successful isolation of graphene (Novoselov, 2004).

Graphene has a number of unique properties that are very interesting for both fundamental studies and future applications. The surface area of graphene is 2630 m^2/g. In terms of mechanical properties, graphene is second to none. Its measured tensile strength of 130 GPa is 100 times the strength of steel (Lee, 2008) and the measured modulus of defect free graphene is 1.2 TPa is 6 times the modulus of steel (Lee, 2008). The electrical and thermal transport properties of graphene are very unique. Graphene has room temperature electrical conductivity of $6x10^3$ S/m (Du, 2008) and thermal conductivity of $5x10^3$ W/m.K (Balandin, 2008). Single layer graphene is very transparent as it only absorbs 2.3% of the incident light (Nair, 2008).

Graphene was initially isolated from graphite using the micromechanical method. Nowadays, graphene is produced using a large number of both bottom-up and top-down methods. Bottom-up methods build graphene sheets from compounds that include carbon. These methods include carbon vapor deposition (CVD), arc-discharge, epitaxial growth of SiC, self-assembly, and reduction of CO_2 (Kim, 2010). These methods typically provide small scale production of high quality and large size graphene sheets. These methods produce monolayer and multiple layer graphene suitable for electronic applications and fundamental studies. On the other hand, top-down methods separate graphene from directly from graphite or graphite derivative. These methods are suitable for “large scale” production of small size pure or chemically modified graphene suitable for applications that require large graphene quantities, e.g. polymer nanocomposites. Examples of the top-down methods include the micromechanical cleavage method, direct sonication of graphite, Electrochemical method, supercritical CO_2 exfoliation of graphite, super acid dissolution of graphite, solvothermal reduction of graphite oxide (GO), chemical reduction of graphite oxide, and thermal exfoliation/reduction of graphite oxide. Currently, the most promising methods for large scale production of graphene are based on the exfoliation and reduction of GO. GO was first

prepared over 150 years ago by Brodie (Brodie, 1859). Analogous to graphite, which is composed of stacks of graphene sheets, GO is composed of graphene oxide sheets stacked with an interlayer spacing between 6 and 10 Å depending on the water content.

GO is built of pristine aromatic "islands" separated by aliphatic regions containing epoxide and hydroxyl groups and double bonds as shown in Fig. 1 (Lerf, 1998). GO has C/O atomic ratio of 2/1.

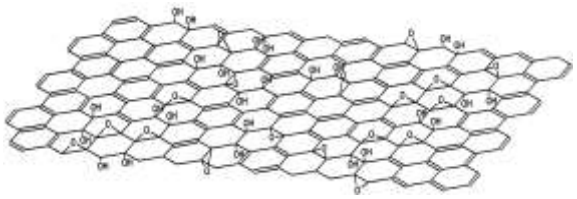

Fig.1. Proposed chemical structure of GO (Lerf, 1998)

The thermal exfoliation GO leads not only to separation of the graphene oxide sheets but also to reduce their oxygen content such that the C/O atomic ratio increases to about 10/1. This reduction process is necessary to restore the electrical properties of graphene as GO is electrically nonconductive but thermally reduced graphene (TRG) is highly conductive (MacAllister, 2007).

Polymer nanocomposite was one of the first areas that benefited from the discovery of graphene. In the first polymer graphene nanocomposite, Stankvoich *et al.* demonstrated that electrically conductive polystyrene (PS) can be made with a very low loading of chemically modified graphene (Stankovich, 2006). As shown in Fig. 2, PS-graphene nanocomposite percolates at 0.1 vol.% loading of chemically reduced graphene. Moreover, very high conductivity of 2.5 S/m was achieved with a loading of 2.5 vol.%.

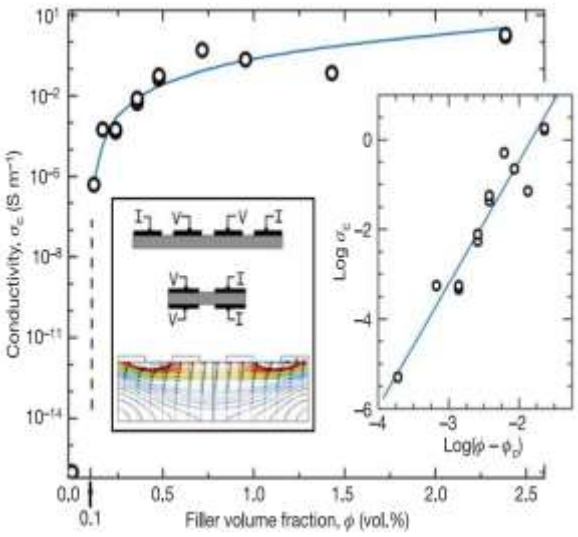

Fig.2. Electrical conductivity of polystyrene-graphene composite as function of graphene loading. (Stankovich, 2006)

In this article, we investigate the effect of the processing method and PE matrix functionalization on the morphological, mechanical, and electrical properties of PE nanocomposites with thermally reduced graphene (TRG).

EXPERIMENTAL METHODS

Materials:

Natural flake graphite (-10 mesh, 99.9%, Alfa Aesar), Sulfuric Acid (95-97%, J.T. Bakers), Hydrochloric Acid (37%, Reidel- deHaen), Hydrogen Peroxide (30% solution, BDH), Potassium Permanganate and Sodium Nitrate (Fisher Scientific) are used as received. Commercial LLDPE resin, Affinity PE was obtained from the Dow Chemical Co. PE is a low-density PE copolymer of ethylene and octene (24 wt % octene content, density: 0.87 g/cm^3, melt flow index: 5 g/10 min at 190 °C). Its weight (M_w) and number (M_n) averaged molecular weight are 201 and 67 kg/mol, respectively. The same PE, but grafted with MA (PE-MA, 0.8 wt % MA content) was also provided by the Dow Chemical Co. MA grafting was conducted in reactive extrusion with peroxides. M_w and M_n of PE-MA are 176 and 71 kg/mol, respectively. For TRG synthesis, natural flake graphite (-10 mesh, 99.9%) was purchased from Alfa Aesar.

Methods

Preparation of TRG

Graphite is oxidized using Staudenmaier method (Staudenmaier, 1898) as follows: graphite (5 g) is placed in ice-cooled flask containing a mixture of H_2SO_4 (90 ml) and HNO_3 (45 ml). Potassium chlorate (55 g) is added slowly to the cold reaction mixture. The reaction is stopped after 96 h by pouring the reaction mixture into deionized water (4 L). 5% HCl solution is used to wash the produced graphite oxide (GO) until no sulfite ions are detected. The mixture is then washed with water till no chloride ions are detected. GO is dried in a vacuum oven over night. TRG is produced by simultaneous exfoliation/reduction of GO by rapid heating at 1000^o C in a tube furnace under flow of nitrogen for 30 s.

Nanocomposite Preparation

PE-TRG and functionalized PE-TRG composites with TRG loading from 0.5 wt.% to 3 wt.% are prepared by melt and solvent blending methods. In melt blending, PE and PE functionalized with maleic anhydride are blending with TRG at 180 ºC in DACA microcompounder at 200 rpm speed for 8 minutes under N_2 purge. In solvent blending method, PE and PE-MA are dissolved in toluene refluxed at 110º C. TRG dispersion in toluene is mixed with PE toluene solution and stirred. The composite is solvent casted over heated plate 70-80º C.

Nanocomposite Characterization

Wide-angle X-ray diffractograms of graphite, GO, and TRG were obtained using a Bruker-AXS (SIEMENS) D5005 X-ray diffractometer (CuKα radiation, 45kV and 40 mA) in the 2θ range of 5 – 30° at scan rate of 0.02 °/s.

Scanning Electron Microscope (e-SEM, FEI Quanta 250) was used to study the morphology of TRG. TRG samples for SEM imaging were prepared by applying the powder directly to a carbon adhesive tape.

Transmission electron microscopy (TEM) was used to investigate the dispersion of TRG in different PE samples. Composite films embedded in an epoxy matrix (TRA-BOND 2115, Tra-Con) were microtomed (Leica Ultracut) at –90 °C into 85-100 nm thick slices using a diamond knife and transferred onto 400 mesh copper grids.

The degree of crystallinity of PE was determined by differential scanning calorimetry (DSC, TA Instruments Q1000). 5-10 mg of thin films was loaded into non-hermetic aluminum pans. Scanning was performed from -100 °C to 250 °C at the rate of 10 °C/min.

Dc surface resistance of the composite films was measured with an 11-probe meter (PRS-801, Prostat). In order to ensure sample uniformity, geometric averages of the resistance measured from 3-4 different spots from each side of the films are reported.

The tensile modulus of the composites was evaluated with Rheometrics Solids Analyzer (RSA II, TA Instruments). 3-4 mm wide strips cut from the solvent cast or compression molded films were mounted between the film fixtures of RSA II. Tensile deformation at 0.0005 /s was applied to the specimen and static Young's modulus was determined from the slopes of stress-strain responses of the composites at 0.5-1.5 % strain.

RESULTS AND DISCUSSION

TRG Characterization

The morphology of the as prepared and dispersed TRG is examined using SEM and TEM as shown in Fig. 3. The fluffy aggregated and unlayered structure of TRG is evident in the SEM images, Fig. 3-a. The aggregation of the TRG as shown by the SEM images is expected for the as prepared TRG which was never dispersed in a liquid. On the other hand, the TEM image of TRG (Fig. 3-b) reveals that TRG is composed of thin and large sheets with paper-like structure. Large volume expansion upon exfoliation is clearly shown in Fig 3-c.

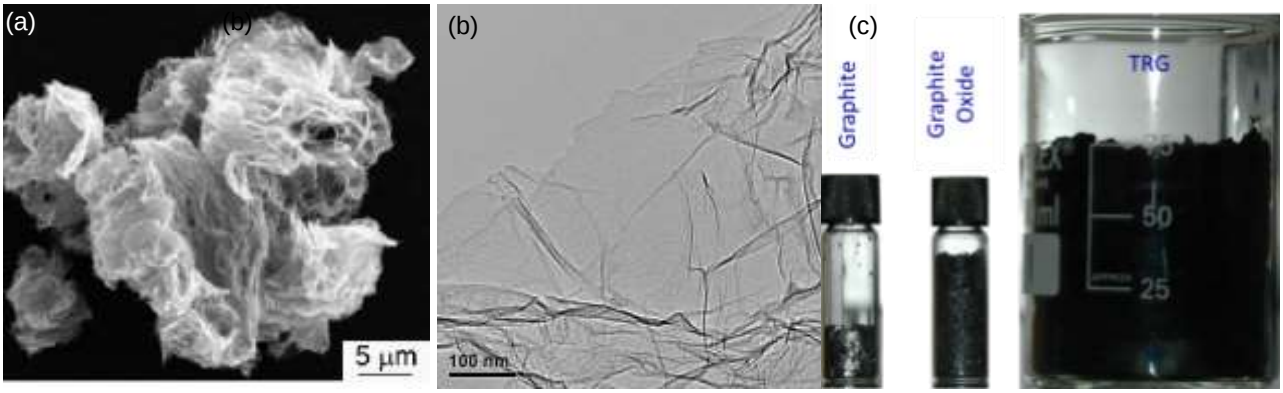

Fig. 3: SEM image (a) and TEM Image (b) of TRG and electronic image showing the volume of 0.5 g of graphite, GO, and TRG (c).

The structural changes due to oxidation of graphite and exfoliation of GO is followed by XRD. Fig. 4shows the diffraction patterns for graphite, GO, and TRG. The diffraction pattern for graphite has a strong 002 peak at 2 θ = 26.4 corresponding to the interlayer d-spacing of 0.335 nm. On the other hand, GO pattern shows the shift of the 002 peak to at 2 θ = 11.4 indicating expansion of the interlayer spacing to 7.4 nm. Alternatively, TRG diffraction pattern does not show any diffraction peaks confirming the complete exfoliation of the reduced graphene layers.

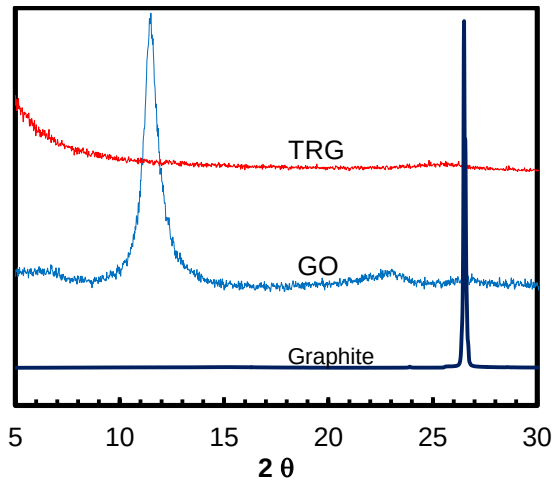

Fig. 4: XRD diffraction pattern of graphite, GO, and TRG.

Composite Morphology and TRG Dispersion

The morphology of the nanocomposites is examined with TEM. Based on TEM micrographs, the role of PE functionalization and blending method on the dispersion of TRG is discussed in the next few sections.

Electron micrographs of melt blended PE and PE-MA containing 1 wt % TRG are provided in Fig. 5. Unlike fully isolated, single graphene sheets blended in solution (Fig. 6-a and b), complete exfoliation is rarely observed for the melt compounded TRG/PE (Fig. 5-a and b). In Fig. 5-a and b, areas highly

concentrated with graphene stacks are distinguished from regions which lack graphene suggesting local concentration fluctuation. In melt compounding, graphene dispersion could not be improved by MA grafting on PE. In contrast to TRG layers well exfoliated in solvent blended PE-MA (Fig. 5-c and d), melt processed samples appear predominantly phase separated (Fig. 6-c and d). Note that the morphology of melt compounded TRG/PE is distinguished from that of solvent blended TRG in un-functionalized PE. While TRG aggregates formed after solvent mixing with PE show some degree of inter-particle connectivity (Fig. 6-a and b), aggregates in melt blended PE are mostly isolated from one another (Fig. 5). These morphological differences may explain the observed trend in the electrical conductivity of solvent and melt blend samples as will be discussed later.

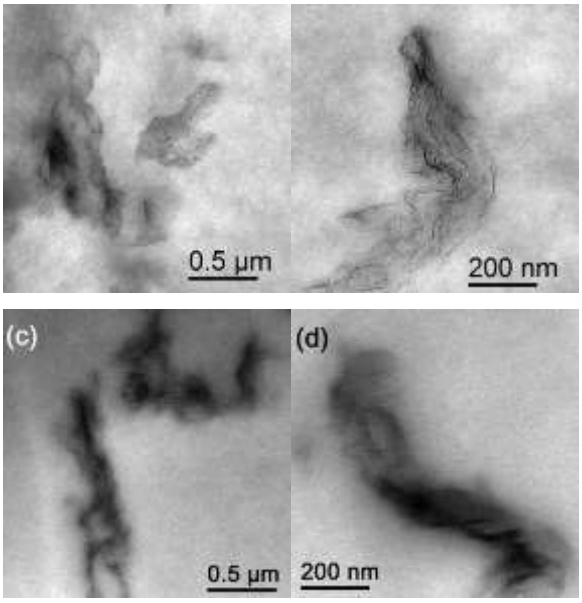

Fig. 5. TEM micrographs of 1 wt.% TRG melt blended with PE (a, b) and PE-MA (c, d)

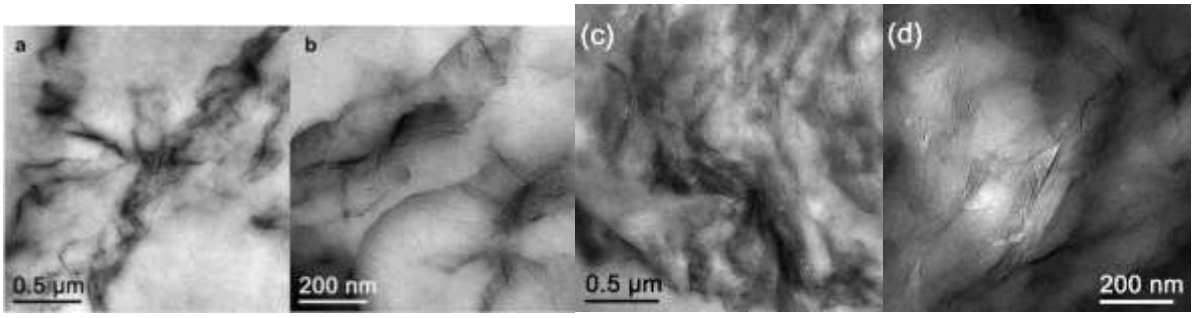

Fig. 6. TEM micrographs of 1 wt.% TRG solvent blended with PE (a, b) and PE-MA (c, d)

Mechanical Properties

Different loading of TRG was incorporated into PE and PE-MA via melt and solvent compounding. The increase in Young's modulus for the composite samples is shown in Fig. 7. For all composite samples, the

modulus is higher than that of pure polymer. Moreover, the increase in Young's modulus increases with TRG loading irrespective of the blending method and polymer type. However, the modulus improvement is more significant for solvent blended samples. The moduli for PE-MA samples are higher than those for the unfunctionalized samples for the same solvent blending method. These results are consistent with the morphology of the composite samples observed by TEM as discussed in the previous section.

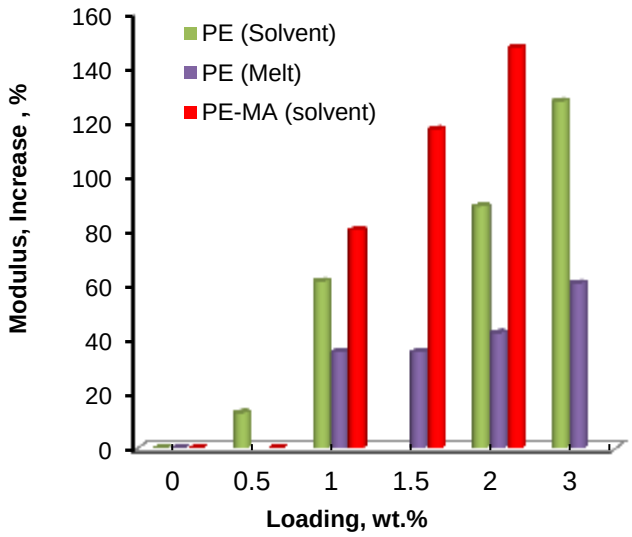

Fig. 7: increase in the modulus for PE-TRG and PE-MA-TRG composites with different TRG loading and blending methods.

The mechanical properties of semi-crystalline polymers including PE can be affected by the degree of crystallinity. The crystallinity of LLDPE and TRG composites was estimated by DSC measurements. The crystallinity of PE was 16% for both solvent cast and melt pressed films and was not appreciably influenced by either graphene dispersion or functionalization with MA. Therefore, reinforcement with graphene is solely responsible for the improved tensile stiffness of the composites.

Electrical Conductivity

Sample spanning pathways for electrical conduction can be formed via percolation of graphene in the polymer matrix. Surface resistance of PE and PE-MA composite samples with different loading of TRG blended by melt and solvent blending is shown in Fig. 8. As shown in the figure, the addition of TRG decreases the surface resistance regardless of blending method or polymer functionalization. However, for all TRG loadings, the surface resistance of solvent blended samples is lower than that of the melt blended sample. This is consistent with the morphology of the solvent and melt blended samples. TRG loading required for electrical percolation for solvent blended samples, both PE and PE-MA), is about 0.5

wt.% (0.2 vol.%). In contrast, the percolation loading of melt blended samples is about five times higher, i.e. 2.5 wt. % (1.0 vol.%).

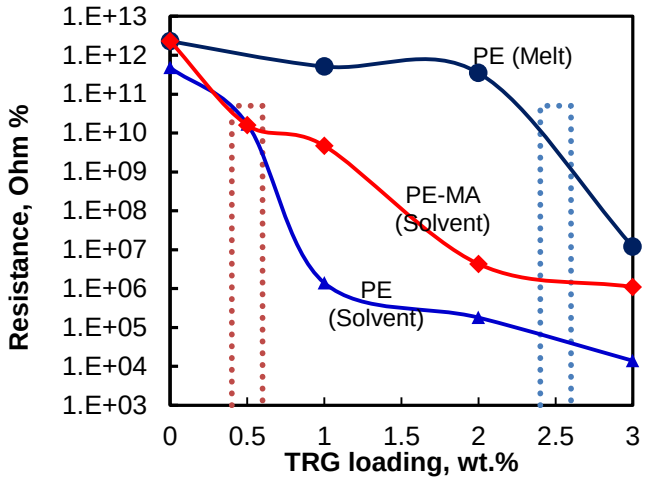

Fig. 8: Electrical resistance for PE-TRG and PE-MA-TRG composites with different TRG loading and blending methods.

A rather negative influence of PE functionalization on conductivity improvement is observed for PE-MA composites. In Fig. 8, a greater decrease in electrical resistance by TRG incorporation was achieved with PE than PE-MA for solvent blended samples. Even with seemingly better dispersion from TEM analysis, TRG in PE-MA resulted in higher electrical resistance than for TRG in PE throughout the entire concentration.

CONCLUSIONS

We have demonstrated that blending method and functionalization of the polymer matrix plays a critical role in the dispersion of TRG into PE matrix. Solvent blended TRG with PE greatly improved the dispersion of TRG compared to the melt blending case. Functionalized PE with Maleic anhydride also improves the dispersion of TRG in PE. The improved TRG dispersion has clearly been reflected in the level of enhancement of the mechanical and electrical properties of the composites. Electrical conductivity percolation was achieved at low loading when solvent blending is used, i.e. 0.5 wt.%. On the other hand, the percolation limit for melt blended samples was 2.5 wt.%, which is 5 times higher than that for solvent blended samples. Although incorporation of TRG enhanced the stiffness of PE regardless of the blending method or matrix functionalization, the level of enhancement was higher for solvent blended samples compared to melt blended samples and also higher for functionalized sample compared to unfunctionlized PE. The results suggest that enhancing the dispersion of TRG in the matrix is crucial for improved composite properties.

Acknowledgement

The author Appreciate the contribution of Dr. Hynwoo Kim, Department of Chemical Engineering and Materials Science, University of Minnesota. Financial support from the Abu Dhabi-Minnesota Institute for Research Excellence (ADMIRE) is also acknowledged.

REFERENCES

Brodie, B. C. 1859. On the Atomic Weight of Graphite. Philos. Trans. R. Soc. London 149:249–259.

Balandin, A. A., S. Ghosh, W. Bao, I. Calizo, D. Teweldebrhan, D., F. Miao, and C. N. Lau. 2008. Superior Thermal Conductivity of Single-Layer Graphene. Nano Letters 8: 902-907.

Du, X., I. Skachko, A. Barker, and E. Y. Andrei. 2008. Approaching Ballistic Transport in Suspended Graphene. Nature Nanotechnology 3: 491-495

Geim, A. K. and K. S. Novoselov. 2007. The Rise of Graphene. Nature Mater. 6: 183–191.

Kim H, A. A. Abdala, and C.W. Macosko. 2010. Graphene/Polymer Nanocomposites. Macromolecules 43:6515-.6530.

Lee, C., X. Wei, J. Kysar, and J. Hone. 2008. Measurement of the Elastic Properties and Intrinsic Strength of Monolayer Graphene. Science 321: 385-388.

Lerf, A.; H. He, M. Forster, and J. Klinowski. 1998. Structure of Graphite Oxide Revisited. J. Phys. Chem. B 102: 4477–4482.

McAllister M. J., J. L. Li, D. H. Adamson, H. C. Schniepp, A. A. Abdala, J. Liu, M. Herrera-Alonso, D. L. Milius, R. Car, R. K. Prud'homme, I. A. Aksay. 2007. Single Sheet Functionalized Graphene by Oxidation and Thermal Expansion of Graphite .Chem Mater 19:4396-4404.

Nair, R. R., P. Blake, A. N. Grigorenko, K. S. Novoselov, T. J. Booth, T. Stauber, N. M. R. Peres, and A. K. Geim. 2008. Fine Structure Constant Defines Visual Transparency of Graphene. *Science* **320**: 1308

Novoselov, K. S.; A. K. Geim, S. V. Morozov, D. Jiang, D. Y. Zhang, S. V. Dubonos, I. V. Grigorieva, A. A. Firsov. 2004. Electric Field Effect in Atomically Thin Carbon Films. Science 306: 666–669.

Ramanathan T, A. A. Abdala, S. Stankovich, D. A. Dikin, M. Herrera-Alonso, R. D. Piner, D. H. Adamson, H. C. Schniepp, X. Chen, R. S. Ruoff, S. T. Nguyen, I. A. Aksay, R. K. Prud'Homme, and L. C. Brinson. 2008. Functionalized Graphene Sheets for Polymer Nanocomposites. Nat Nanotechnol 3:327-331.

Stankovich S, D. A. Dikin, G. H. B. Dommett, K. M. Kohlhaas, E. J. Zimney, E. A. Stach, R. D. Piner, S. T. Nguyen, and R. S. Ruof. 2006. Graphene-based composite materials . Nature 442:282-286.

Staudenmaier, L. 1898. Method for the Preparation of Graphitic Acid. Ber. Dtsch. Chem. Ges. 31:1481–87.

Yttria- and lanthanum-doped zirconium dioxide nanofibers: the efficient way to increase specific surface area

Ing. Aneta Krausová[1)],Ing. JaroslavaMorávková Ph.D[1)], Ing.MiroslavTejkl Ph.D[1)],

Ing. PetrSazama Ph.D[2)]

[1)]PARDAM s.r.o., R&D Laboratory & Production facility: Soškova 1562, 592 31, Nové Město na Moravě, Czech Republic

[2)]ÚFCH JH AV ČR, Dolejškova 2155/3, 182 23, Praha 8, Czech Republic

1. Introduction

Zirconia has an excellent combination of electrical, thermal and mechanical properties. Its unique properties are largely based on the crystal structures. These advantages make zirconia materials suitable for potential applications as transparent optical devices, electrochemical capacitor electrodes, oxygen sensors, fuel cells, advanced ceramics and special catalysts [1, 2]. Depending on the preparation method and thermal treatment, several crystalline phases can be obtained [3]. The transformation between these phases is very important for the processing and mechanical properties of zirconia. In order to obtain the stable tetragonal or cubic phase of zirconia at room temperature, many studies have been focused on doping of zirconia. It is known that a variety of cations can serve as stabilizers. These dopants prevent from the undesirable transformation from the tetragonal to the monoclinic phase. Yttrium as a one of the most famous dopant enhances electrical conductivity and influences also the growth and the size of crystalline grains and as a consequence also the specific surface area [5-10].

2. Experimental

For comparison yttria- and lanthanum-doped and undoped zirconia were prepared using two technologies: electrospinning and forcespinning. For electrospinning Nanospider NS (Elmarco, The Czech Republic) was used, forcespinning was realized using laboratory machine Cyclone L1000M/D (FibeRio Technology Corporation, Texas). Experiments were concluded at the R&D and Production Centre of Pardam company, which is located in Nové Město na Moravě in the Czech Republic. For forcespinning as the precursor Zirconyloxychloride was used, while the electrospinning solutions were based on Zirconium propoxide. Granular polyvinyl pyrrolidone was used as the polymeric component. Yttrium and Lanthanum nitrate were used to achieve defined molar ratio of Y/Zr and La/Zr. The prepared nanofibers were calcined and the resulting structure of fibers was characterized by SEM. The specific surface areas were measured using BET and X-ray diffraction was used to determine the crystalline phase.

3. Results and discussion

The way of spinning certainly influences the appearance and the properties of the nanofibers. The diameter of forcespun nanofibers is larger and there also some sintered pieces, which come probably from the beads and drops contained in the precursor nanofibers**.** To determine phase changes depending on the various molar ratio dopants and zirconia the X-ray diffraction was measured. Using RIR method it was found that forcespun undoped zirconia contains more tetragonal phase than electrospun zirconia. These results indicate that forcespun undoped zirconia is more stable and so it was also predicted that the specific surface area of forcespun undoped zirconia could be larger. It was found that the amount of tetragonal phase

increases with the increasing concentration of dopants and that the concentration ≥ 4 mol. % of dopants causes pure tetragonal phase of zirconia. The measurements of the specific surface areas show that whereas the specific surface area of forcespun doped zirconia increases with increasing concentration of dopants, the specific surface area of electrospun doped zirconia achieved local maximum implying that higher concentration of dopants than (1 - 2 mol.%) decreases the specific surface area. In both cases lanthanum-doped ZrO_2 provides higher value of specific surface area than yttria-doped ZrO_2, so doping with lanthanum seems to be more convenient.

4. Conclusion

In conclusion, it was found that the addition of dopants can greatly increase the specific surface area. Lanthanum as a dopant seems to be more effective than yttria, but the choice depends also on following application. Although the diameter of forcespun fibers is markedly higher, the specific surface is higher too. It is probably influenced by the different structure of electrospun and forcespun fibers, which is formed by calcination treatment and depends on the composition of precursors, dopants, spinning solution and technology itself. The largest specific surface area (70 m^2/g) was achieved by spinning of 8 mol. % lanthanum-doped zirconia. This is the very attractive result because the specific surface area of pure zirconia is almost three times lower. In summary, depending on the desired specific surface area, price or special requirements ″ zirconia - nanofibers - tailor - made ″ can be prepared.

5. References

1. Li, L.; Zhang, P.; et al. Phase transformation and morphological evolution of electrospun zirconia nanofibers during thermal annealing. *Ceramics International* **2010**, *36*, 589–594.

2. Ruiz-Rosas, R.; et al. Methanol decomposition on electrospun zirconia nanofibers. *Catal. Today* **2012**, *187*, 77–87.

3. Uslu, I.; et al. Synthesis and Characterization of Boron Doped Alumina Stabilized Zirconia Fibers. *Fibers and Polymers* **2001**, *12* (3), 303–309.

4. Kan, Y.; et al. Yb_2O_3 and Y_2O_3 co-doped zirconia ceramics. *J. Eur. Ceram. Soc.* **2006**, *26* (3), 3607–3612.

5. Li, P.; et al. Effect of Dopants on Zirconia stabilization-An X-ray absorption study: I, Trivalent Dopants. *J. Am. Ceram. Soc.* **1994**, *77* (1), 118–128.

6. Álvarez, M.; et al. Structural and Textural Study on ZrO2-Y2O3 Powders. *J. Eur. Ceram. Soc.* **1998**, *18* (1), 1201–1210.

7. Tunc, T.; et al. Fabrication and Characterization of Boron Doped Yttria-stabilized Zirconia Nanofibers. *Polymer Engineering and Science* **2013**.

8. Santos, V.; et al. Correlation between thermal treatment and tetragonal/monoclinic nanostructured zirconia powder obtained by sol-gel process. *Rev. Adv. Mater. Sci.* **2008**,*17*, 62–70.

9. Kosacki, I.; et al. Electrical conductivity of nanocrystalline ceria and zirconia thin films. *Solid State Ionics* **2000**, *136*, 1225–1233.

10. Li, J.; et al. Hollow fibers of yttria-stabilized zirconia (8YSZ) prepared by calcination of electrospun composite fibers. *Mater.Lett.* **2008**, *62*, 2396–2399.

Nanotech Dubai 2013: SETCOR International Conference on Nanotechnology Dubai 2013
28 - 30 October, 2013, Dubai, United Arab Emirates

Tomonaga-Luttinger Liquid and Coulomb Blockade in a Single Walled Carbon Nanotube aligned on a Quartz Substrate

El-Hadi Sadki[1], Tohru Watanabe[2], Takahide Yamaguchi[2], and Yoshihiko Takano[2]

[1] Physics Department, United Arab Emirates University, PO. Box 17551, Al-Ain, United Arab Emirates
[2] National Institute for Materials Science (NIMS), 1-2-1 Sengen, Tsukuba, Ibaraki 305-0047, Japan

Abstract

In this work, the electrical transport properties of an aligned single walled carbon nanotube (SWNT) on an ST-cut quartz substrate are measured. The temperature dependence of the SWNT's electrical resistance shows metallic behavior from room temperature to 120 K, and an increase at lower temperatures down to 2K. The low temperature behavior can be explained in terms of the theories of Tomonaga-Luttinger liquid and Coulomb blockade. These results elucidate the electrical properties of SWNTs in this unique configuration, and pave the way towards prospective device applications.

Keywords: Carbon nanotubes, Aligned carbon nanotubes, ST-cut quartz, Tomonaga-Luttinger liquid, Coulomb blockade

1. Introduction

Single walled carbon nanotubes (SWNTs), with their miniature size, low structural defects and various other superior properties [1-5], are very attractive nanomaterials as basis for future electronic devices [6, 7]. However, there are still many technical obstacles towards the realization of SWNT-based devices, such as the difficulty of their positioning on a substrate, as well as the lack of control of their chirality, which eventually defines their electronic properties. Furthermore, synthesized SWNTs by chemical vapor deposition (CVD) on a substrate are usually short (around 10 μm) and randomly dispersed, which makes it difficult for device fabrication. Recently, it has been reported that arrays of long (hundreds of microns) and horizontally highly aligned SWNTs could be synthesized on some single crystal substrates, such as ST-cut quartz [8] and sapphire [9]. This is an important breakthrough, as the length of the synthesized SWNTs, and their high alignment, makes their electrical characterization and device fabrication much more accessible than ever before. Indeed, a field-effect transistor (FET) has been demonstrated using aligned SWNT arrays on an ST-cut quartz substrate [8]. It is also noted that the latest Raman and photoluminescence data suggest that these SWNTs have predominantly uniform properties [10, 11]. However, and despite a lot of research work on SWNT array on ST-cut quartz [10, 12], no data has been reported so far on the electrical properties or device fabrication of a single isolated SWNT on these substrates. We believe this is important in order to understand the underlying physics of the SWNTs in this unique configuration, which is crucial for any prospective device applications. The lack of published data on an individual SWNT could be attributed to the technical difficulty in applying standard electron-beam lithography method for the fabrication of electrical terminals on an individual SWNT on these substrates, as it is usually inseparable from the other SWNTs in the arrays.

In this work, we present a method for the fabrication of electrical terminals on individual an SWNT aligned on an ST-quartz substrate, and the measurement of its electrical transport properties from room temperature down to 2 K. The method consists of CVD synthesis of an individual SWNT from evaporated metal catalyst pad, and shadow mask evaporation [13-15] of metallic electrical contacts on the SWNT. The dimensions of the catalyst pad are optimized to yield on average one long and horizontally aligned single SWNT after CVD synthesis. In contrast to standard electron-beam lithography technique, this method has the advantage of not exposing the SWNTs to any electron beam irradiation or chemicals that are reported to damage or/and contaminate the SWNTs [16, 17]. Furthermore, in order to minimize any damage or contamination of the SWNT before electrical properties measurements, scanning electron microscopy (SEM), Raman spectroscopy mapping and atomic force microscopy (AFM) are performed only after all the electrical properties measurements are achieved. The electrical properties of an individual SWNT are measured using four terminals method, and compared with theoretical predictions.

2. Experimental methods

Figure 1 shows a schematic of the process of the synthesis of an individual SWNT and the fabrication of the electrical terminals on top of it. Titanium (Ti) film, with 2 μm thickness, is used as a shadow mask for the evaporation of cobalt catalyst pads. Catalyst pad patterns are milled in the titanium film using a focused ion beam (FIB) system. The cobalt catalyst is evaporated through the titanium mask's patterns by electron beam (EB) evaporation, with a thickness of 2.0 nm, measured by a calibrated thickness monitor in the evaporator. After catalyst deposition, SWNTs are synthesized by thermal CVD method using a double zone furnace equipped with a quartz tube of 27 mm in inner diameter. ST-cut quartz substrates are placed at the center of the downstream side of the furnace. A typical CVD process is as follows: Substrate is heated in a 200 sccm O_2 flow from room temperature to 900 ^{o}C for 30 minutes and let to settle for 5 minutes. Next, the O_2 flow is stopped and replaced by 300 sccm Ar flow for 10 mins. Then, a 200 sccm H_2 gas is flown for 10 mins. Finally, the H_2 gas is co-flown with 300 sccm CH_4 gas for 15 mins, which leads to SWNTs synthesis. Finally, the sample is left to cool-down to room temperature in a continuous H_2 flow.

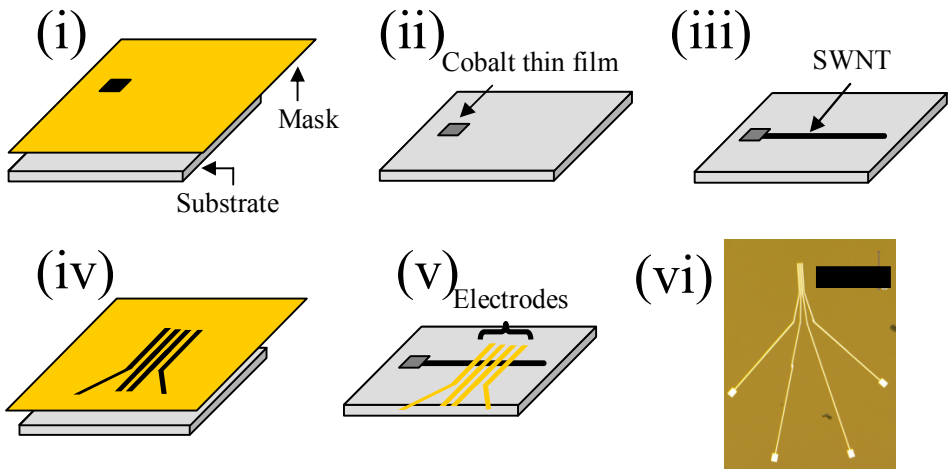

Figure 1 Schematic diagram of the fabrication of terminals on a SWNT using shadow-mask evaporation technique: (i) A metal mask for catalyst pattern is set just above the substrate and cobalt catalyst is thermally evaporated. (ii) Deposited Co catalyst pad on the substrate. (iii) After CVD, SWNT is grown horizontally from the catalyst pad. (iv) A metal mask for electrodes is set just above the substrate (v) After evaporation, electrodes are set on the SWNT. (vi) Optical microscopy image of fabricated terminals. The scale bar is 200 μm.

Electrodes on the SWNT are also fabricated using shadow mask evaporation technique. The metal masks are prepared by the same method as of that used for catalyst pattern. Palladium (Pd) is selected as the material of the electrodes because of its low contact resistance to SWNTs [18, 19]. The Pd electrodes, with a thickness of 50 nm, are EB evaporated in a four-terminal configuration, with a typical distance of 4.0 μm between adjacent electrodes. The electrical properties of the SWNTs are measured from room temperature down to 2 K, using a physical properties measurement system (PPMS) for the temperature control. Voltages of ~ ±1 V are applied by a voltage source through a 10 MΩ resistance connected in series with the sample, and the voltage is measured across the inner-electrodes on the sample by a voltmeter. For imaging and analytical characterization of SWNTs under the terminals, Raman spectral mapping, AFM system and SEM system, are used. Raman spectroscopy is performed with a laser of 532 nm in wavelength and spot size of 0.5 μm. AFM is conducted in cyclic-contact AC mode. In order to synthesize an individual and long SWNT for electrical characterization, the catalyst's pad dimensions are to be controlled accordingly. Figure 2 (a) shows an SEM image of SWNTs synthesized from a catalyst pad of 100 x 10 μm in area. A lot of SWNTs are obtained in this case, with average lengths of more than 100 μm. On the other hand, as shown in Figure 2 (b), if a catalyst pad of 10 x 2 μm is used, only one or a few SWNTs are obtained, with typically the emergence of an individual SWNT of more than 100 μm in length. Figure 2 (c) shows deposited electrodes on another SWNT synthesized from the same pad's dimensions of 10 x 2 μm.

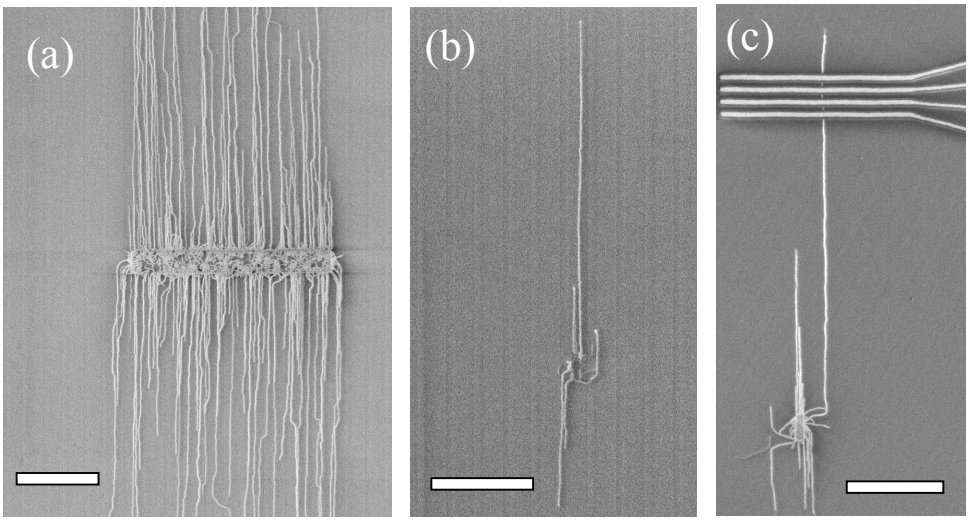

Figure 2 SEM images of SWNTs synthesized from different catalyst pads. Size of catalyst pad is 100 x 10 μm in (a), 10 x 2 μm in (b), and 10 x 2 μm in (c) with deposited electrodes. All scale bars are 40 μm.

Figure 3 (a) shows the AFM profile of a SWNT between electrodes, with a measured diameter of 0.9 nm. This diameter confirms indeed that this nanotube is single walled. It is noted that with the 2 nm thickness of the Co catalyst used, the obtained SWNTs have typical diameters of less than 1 nm. Figure 3 (c) presents Raman spectroscopy mapping of the same nanotube between the electrodes. In Figure 3(d), Raman spectrum of the nanotube shows a strong G-band peak. On the other hand, D-band peak is not observed. This indicates that the synthesized SWNTs are nearly defect-free.

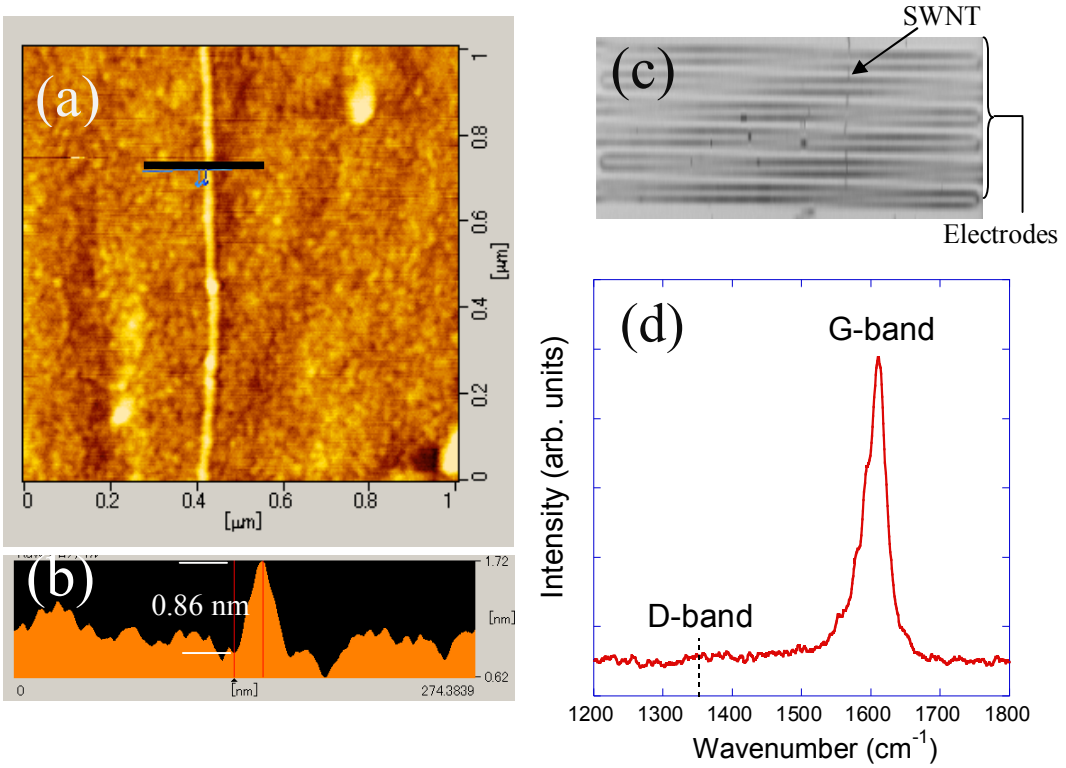

Figure 3 (a) AFM topography image and (b) profile of a SWNT. (c) Raman mapping image measured for a SWNT located between electrodes. The area of G-band peak (1550 – 1650 cm^{-1}) is plotted. Vertical black line shows SWNT location and horizontal wide lines are the terminals. (d) Raman spectrum of the SWNT showing the G-band peak, with the position of the D-band peak shown.

3. Results and discussion

Figure 4(a) shows the result of the temperature dependence of the electrical resistance (normalized to its value at 300 K) of a SWNT measured with an electrical current of 10 nA. The nanotube has a diameter of 0.9 nm, as measured by AFM. The SWNT's resistance decreases with decreasing temperature from room temperature down to about 120 K, and then it increases by decreasing temperature down to 2 K. At the lowest temperature of 2K, the resistance reaches about 4 times its room temperature value of 181 kΩ.

First, the value of the resistance at room temperature is considered. The intrinsic resistance of a SWNT in the diffusive regime (non-ballistic) can be estimated from the formula:

$$R = R_c + R_Q(L/l + 1)$$

where R_c, R_Q ~ 6.45 kΩ, L and l, are the contact resistance between the SWNT and the electrodes, the quantum resistance of a SWNT, the measured length of the SWNT, and the electron's mean free path, respectively [20]. By comparing the 2 and 4-terminal resistances of the sample, and using L = 4 μm (distance between the inner voltage terminals), R_c and l, are estimated to be 8 and 148 and 18 nm, respectively. The deduced mean free path at 300 K is in the same order of magnitude as the reported values for metallic SWNTs with similar diameter [21, 22]. This resistance at high temperatures is attributed to inelastic scattering between electrons and acoustic phonons [22].

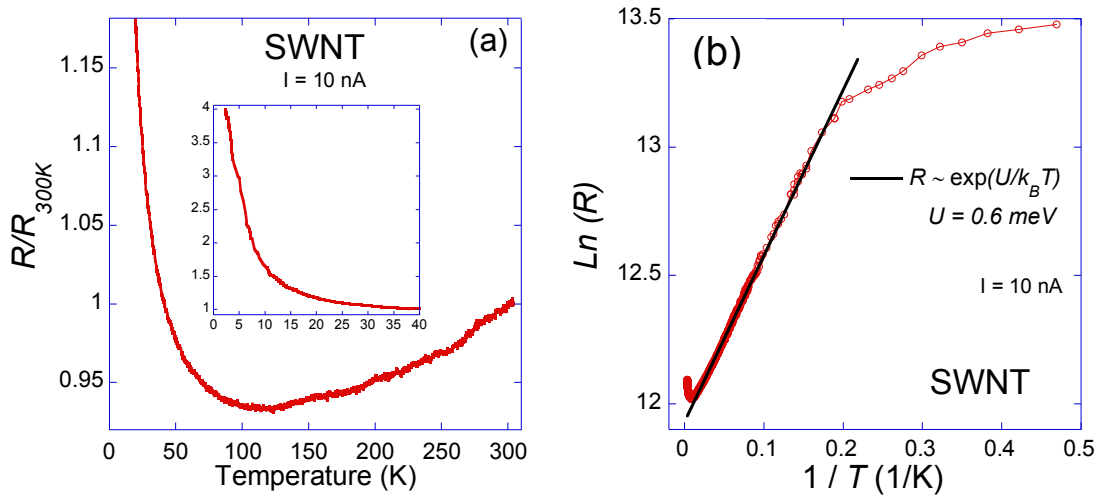

Figure 4 (a) Temperature dependence of the electrical resistance of the nanotube (normalized to its value at 300 K). Insets show the resistance in the low temperatures range. The electrical current is 10 nA in all measurements. (b) Natural logarithm of the resistance versus $1/T$. The solid lines are fits to a thermal activation formula $R \sim \exp(U/k_BT)$, where U is an energy barrier (see text).

The decrease in the resistance of with decreasing temperature from room temperature down to about 120 K is attributed to the metallic nature of this nanotube [23]. To explain the "semiconducting-like" behavior of the resistance versus temperature below 120 K, it is noted that even "metallic" SWNTs can exhibit a "semiconducting" energy gap due their intrinsic curvature [24], mechanical deformation [25], and substrate effects [26]. One possible signature of an energy gap is a thermal activation dependence of the resistance versus temperature, i.e. in the form $R \sim \exp(U/k_BT)$, where U and k_B are an energy barrier and Boltzmann constant, respectively [27]. In order to explore this behavior, a plot of *Ln (R)* versus $1/T$ is shown in figure 4(b), and indeed the curve could be very well fitted to the above activation formula from 60 K down to 5 K, with $U \sim 0.6$ meV. Assuming a standard semiconductor theory [27] this leads to a semiconducting energy gap of $E_g = 2U = 1.2$ meV. Theoretically, there are four (4) "metallic" SWNTs with a curvature-induced energy gap, also called "quasi-metallic" SWNTs, with diameters comparable to our SWNT [28]. These are (8,5), (10,1), (9,3), and (12,0). However, the smallest energy gap is 20 meV for (8,5), which is much higher than the measured E_g. The only remaining SWNT with a diameter comparable to ours is the "metallic" armchair (6,6). Based on the above, it is concluded that the SWNT is most likely to be the metallic armchair (6,6) with an induced small gap due to external effects. Taking into consideration the strong interaction between the nanotube and the substrate, which is the main cause of its alignment on these substrates during CVD growth [29], and the absence of any mechanical deformations (the SWNTs are very straight on the substrate without apparent twisting or curvature), we attribute the induced gap to the effect of the ST-cut quartz substrate. The exact mechanism(s) of interaction between SWNTs and substrate is not well understood and currently is an active area of research [30].

Since SWNTs are considered to be 1D systems, with strong electron-electron interaction, they are predicted to exhibit Tomonaga-Luttinger Liquid (TLL) behavior at low temperatures [31-33]. Furthermore, SWNTs can act as a quantum dot between the metal electrodes, and hence show Coulomb Blockade (CB) tunneling characteristics at sufficiently low temperatures [34-37]. Incidentally, both TLL and CB theories predict the same scaling laws: The resistance R to be proportional to $T^{-\alpha}$ when $eV << k_BT$ (low-bias regime), and to V^{α} when $eV >> k_BT$ (high-bias regime), where V, α, and e, are the voltage drop across the sample, a single scaling coefficient, and the charge of an electron, respectively [36]. In order to extract the values of R in the two different regimes, current-voltage (IV) curves of the sample are measured at various temperatures as shown in Figure 5(a). At high-bias voltages, and low-bias voltage at high temperatures, the IV curves are basically linear with the current I However, at low-bias and low temperatures the IVs are not linear. The origin of this curvature is discussed later.

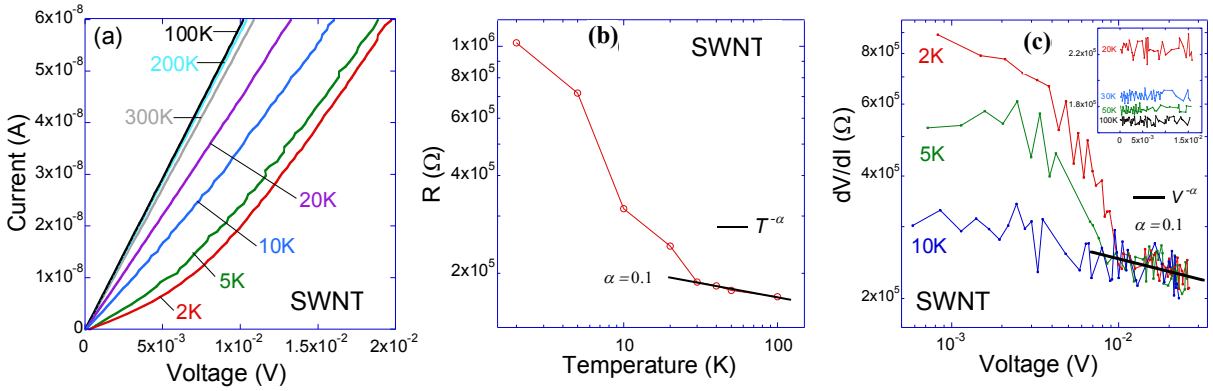

Figure 5 (a) Current-voltage (IV) curves measured at several temperatures from 300 K to 2 K. Solid lines are guides to the eyes. Log-log plots of: (b) the low-bias resistance versus temperature, with data points in circles is the extracted resistance from IV curves at different temperatures, and the solid line is a power law fit $R \sim T^{\alpha}$; (c) High-bias differential resistance versus voltage at 2, 5, and 10 K. The solid line is a power law fit $dV/dI \sim V^{\alpha}$. The inset shows the same data at higher temperatures.

The low bias R is extracted from the IV curves at I = 1 nA, and plotted in a log-log graph versus temperature as shown in Figure 5(b). The data fits well a power law above 30 K, with $\alpha \approx 0.1$. Note that $k_B T$ = 2.59 meV >> eV = 0.29 meV at 30 K. This is in agreement with the regime of validity of the theory. Furthermore, the value of $\alpha \approx 0.1$ is in the same order as the reported values in the literature for SWNTs [31, 36, 37]. Next, R, in the high-bias regime, is extracted from the IV curves at T = 2, 5, and 10 K, and plotted in a log-log graph versus voltage as shown in Figure 5(c). The low temperatures were chosen in order to be as close as possible to the condition $eV >> k_B T$ for this regime. For voltages V higher than about 10 mV, the curve fits well a power law, with $\alpha \approx 0.1$. This is in very good agreement with the extracted value from R versus T in the other regime. Furthermore, knowing that $k_B T \approx 0.9$ meV at T = 10 K, the range of voltages where the power-law fit is found to hold (i.e. above 10 meV), indeed satisfies reasonably well the condition $eV >> k_B T$. The inset of figure 5(c) shows that from 20 K and above the resistance is essentially independent of the applied voltage, i.e. the IV curves are linear, which is exactly what was observed in figure 5(a). Hence, the behavior of the SWNT is consistent with both LLD and CB theories with a scaling exponent $\alpha \approx 0.1$. First, it is noted that the extracted contact resistance, R_c = 8 kΩ, is higher than the quantum resistance R_Q, which satisfies a necessary condition for the occurrence of the CB [38]. Another theoretical condition for achieving CB is to have the charging energy E_c of the SWNT higher than the thermal energy $k_B T$, with $E_c \approx 2.5$ meV/L(μm) on SiO_2 [38]. This yields $E_c \approx 0.6$ meV, which requires a temperature T < 6 K for CB to occur. However, the scaling law is observed up to at least 10 K, which suggests that the observed scaling, at least above 6 K, could be indeed a TLL behavior. It is noted in figure 5(c) that for bias voltages less than about 9 mV at 2 and 5 K, there is an increase in the resistance that could be attributed to enhanced CB effect with reducing bias voltages. This change in R versus V at low-bias voltages could be attributed to a crossover between the TLL and CB regimes [39]. Nevertheless, to experimentally confirm the CB effect, a gate voltage is required to modulate the SWNT's energy levels in order to possibly observe single electron tunneling as evidence for CB [34, 37], which is beyond our current experimental setup.

4. Conclusion

In conclusion, a method is introduced to isolate and measure the electrical properties of an individual SWNT aligned on an ST-cut quartz, from room temperature down to 2 K. The SWNT, with a diameter of 0.9 nm, shows metallic characteristics a high temperatures, and Tomonaga-Luttinger liquid and Coulomb blockade behaviors at low temperatures. These results elucidate some of the electrical properties of SWNTs in this unique configuration, and help pave the way towards prospective device applications.

References

[1] Bachtold A, Hadley P, Nakanishi T, Dekker C: Logic circuits with carbon nanotube transistors. *Science* 2001, 294:1317-1320.
[2] Durkop T, Getty SA, Cobas E, Fuhrer MS: Extraordinary mobility in semiconducting carbon nanotubes. *Nano Letters* 2004, 4:35-39.
[3] Tans SJ, Verschueren ARM, Dekker C: Room-temperature transistor based on a single carbon nanotube. *Nature* 1998, 393:49-52.
[4] Walters DA, Ericson LM, Casavant MJ, Liu J, Colbert DT, Smith KA, Smalley RE: Elastic strain of freely suspended single-wall carbon nanotube ropes. *Applied Physics Letters* 1999, 74:3803-3805.
[5] Yu MF, Files BS, Arepalli S, Ruoff RS: Tensile loading of ropes of single wall carbon nanotubes and their mechanical properties. *Physical Review Letters* 2000, 84:5552-5555.
[6] Berber S, Kwon YK, Tomanek D: Unusually high thermal conductivity of carbon nanotubes. *Physical Review Letters* 2000, 84:4613-4616.
[7] Hong S, Myung S: Nanotube electronics - A flexible approach to mobility. *Nature Nanotechnology* 2007, 2:207-208.
[8] Kang SJ, Kocabas C, Ozel T, Shim M, Pimparkar N, Alam MA, Rotkin SV, Rogers JA: High-performance electronics using dense, perfectly aligned arrays of single-walled carbon nanotubes. *Nature Nanotechnology* 2007, 2:230-236.
[9] Ago H, Nakamura K, Ikeda K, Uehara N, Ishigami N, Tsuji M: Aligned growth of isolated single-walled carbon nanotubes programmed by atomic arrangement of substrate surface. *Chemical Physics Letters* 2005, 408:433-438.
[10] Ding L, Tselev A, Wang JY, Yuan DN, Chu HB, McNicholas TP, Li Y, Liu J: Selective Growth of Well-Aligned Semiconducting Single-Walled Carbon Nanotubes. *Nano Letters* 2009, 9:800-805.
[11] Ishigami N, Ago H, Imamoto K, Tsuji M, Iakoubovskii K, Minami N: Crystal plane dependent growth of aligned single-walled carbon nanotubes on sapphire. *Journal of the American Chemical Society* 2008, 130:9918-9924.
[12] Yuan DN, Ding L, Chu HB, Feng YY, McNicholas TP, Liu J: Horizontally aligned single-walled carbon nanotube on quartz from a large variety of metal catalysts. *Nano Letters* 2008, 8:2576-2579.
[13] Deshmukh MM, Ralph DC, Thomas M, Silcox J: Nanofabrication using a stencil mask. *Applied Physics Letters* 1999, 75:1631-1633.
[14] Ono K, Shimada H, Kobayashi SI, Ootuka Y: A new fabrication method for ultra small tunnel junctions. *Japanese Journal of Applied Physics Part 1-Regular Papers Short Notes & Review Papers* 1996, 35:2369-2371.
[15] Uchihashi T, Ramsperger U, Nakayama T, Aono M: Nanostencil-fabricated electrodes for electron transport measurements of atomically thin nanowires in ultrahigh vacuum. *Japanese Journal of Applied Physics* 2008, 47:1797-1799.
[16] Khamis SM, Jones RA, Johnson ATC: Optimized photolithographic fabrication process for carbon nanotube devices. *Aip Advances* 2011, 1:022106.
[17] Smith BW, Luzzi DE: Electron irradiation effects in single wall carbon nanotubes. *Journal of Applied Physics* 2001, 90:3509-3515.
[18] Javey A, Guo J, Wang Q, Lundstrom M, Dai HJ: Ballistic carbon nanotube field-effect transistors. *Nature* 2003, 424:654-657.
[19] Nosho Y, Ohno Y, Kishimoto S, Mizutani T: Relation between conduction property and work function of contact metal in carbon nanotube field-effect transistors. *Nanotechnology* 2006, 17:3412-3415.
[20] Datta S: *Quantum Transport: Atom to Transistor.* Cambridge University Press; 2013.
[21] Gao B, Chen YF, Fuhrer MS, Glattli DC, Bachtold A: Four-point resistance of individual single-wall carbon nanotubes. *Physical Review Letters* 2005, 95:196802.
[22] Purewal MS, Hong BH, Ravi A, Chandra B, Hone J, Kim P: Scaling of resistance and electron mean free path of single-walled carbon nanotubes. *Physical Review Letters* 2007, 98:186808.
[23] Kane CL, Mele EJ, Lee RS, Fischer JE, Petit P, Dai H, Thess A, Smalley RE, Verschueren ARM, Tans SJ, Dekker C: Temperature-dependent resistivity of single-wall carbon nanotubes. *Europhysics Letters* 1998, 41:683-688.
[24] Kleiner A, Eggert S: Band gaps of primary metallic carbon nanotubes. *Physical Review B* 2001, 63:073408.
[25] Barboza APM, Gomes AP, Archanjo BS, Araujo PT, Jorio A, Ferlauto AS, Mazzoni MSC, Chacham H, Neves BRA: Deformation induced semiconductor-metal transition in single wall carbon nanotubes probed by electric force microscopy. *Physical Review Letters* 2008, 100:256804.
[26] Soares JS, Jorio A: Study of Carbon Nanotube-Substrate Interaction. *Journal of Nanotechnology* 2012, 2012:1-10.

[27] Kittel C: Introduction to Solid State Physics. Wiley; 2004.
[28] Periodic Table of Carbon Nanotubes [http://quantumwise.com/documents/CNT_PeriodicTable.pdf]
[29] Ding L, Zhou W, McNicholas TP, Wang J, Chu H, Li Y, Liu J: Direct Observation of the Strong Interaction Between Carbon Nanotubes and Quartz Substrate. *Nano Research* 2009, 2:903-910.
[30] Chandra B, Perebeinos V, Berciaud S, Katoch J, Ishigami M, Kim P, Heinz TF, Hone J: Low Bias Electron Scattering in Structure-Identified Single Wall Carbon Nanotubes: Role of Substrate Polar Phonons. *Physical Review Letters* 2011, 107:146601.
[31] Bockrath M, Cobden DH, Lu J, Rinzler AG, Smalley RE, Balents L, McEuen PL: Luttinger-liquid behaviour in carbon nanotubes. *Nature* 1999, 397:598-601.
[32] Ishii H, Kataura H, Shiozawa H, Yoshioka H, Otsubo H, Takayama Y, Miyahara T, Suzuki S, Achiba Y, Nakatake M, et al: Direct observation of Tomonaga-Luttinger-liquid state in carbon nanotubes at low temperatures. *Nature* 2003, 426:540-544.
[33] Danilchenko BA, Shpinar LI, Tripachko NA, Voitsihovska EA, Zelensky SE, Sundqvist B: High temperature Luttinger liquid conductivity in carbon nanotube bundles. *Applied Physics Letters* 2010, 97:072106.
[34] Bockrath M, Cobden DH, McEuen PL, Chopra NG, Zettl A, Thess A, Smalley RE: Single-electron transport in ropes of carbon nanotubes. *Science* 1997, 275:1922-1925.
[35] Dayen JF, Wade TL, Rizza G, Golubev DS, Cojocaru CS, Pribat D, Jehl X, Sanquer M, Wegrowe JE: Conductance of disordered semiconducting nanowires and carbon nanotubes: a chain of quantum dots. *European Physical Journal-Applied Physics* 2009, 48:10604.
[36] Kane C, Balents L, Fisher MPA: Coulomb interactions and mesoscopic effects in carbon nanotubes. *Physical Review Letters* 1997, 79:5086-5089.
[37] Postma HWC, Teepen T, Yao Z, Grifoni M, Dekker C: Carbon nanotube single-electron transistors at room temperature. *Science* 2001, 293:76-79.
[38] Reich S, Thomsen C, Maultzsch J: *Carbon Nanotubes: Basic Concepts and Physical Properties.* Wiley; 2008.
[39] Bellucci S, Gonzalez J, Onorato P: Crossover from the luttinger-liquid to coulomb-blockade regime in carbon nanotubes. *Physical Review Letters* 2005, 95:186403.

HIV-AIDS Nanomedicine

Neelotpol Sarkar[a] and Susmita Mitra[b]

Amity Institute of Nanotechnology, Amity University, Sector-125, Noida, India
[a] neelotpol@gmail.com; [b] smitra@amity.edu

The Human Immuno Deficiency Virus (HIV) induced Autoimmune Deficiency Syndrome (AIDS) is considered a major public health threat, and successful treatment as well as control of HIV-AIDS is one of the biggest challenges of the 21st century [1]. According to present statistics AIDS has claimed an estimated 1.8 million lives globally, including more than 250,000 children. In addition, more than 34 million individuals are infected with HIV worldwide and more than 2 million new cases of HIV infection have been reported since. It is more than a decade into the 21th century, yet our combat with HIV is far from over!

From a historical perspective, the existence of the virus and its role in AIDS was recognised as early as the 1980's. The reason for the compromised immune system was related to the tropism of the virus particularly for CD4+ T lymphocyte which plays an important role in regulating the system. This renders the infected population susceptible to life endangering disease. Since the incubation period of HIV ranges from 3yrs to 20yrs, the initial infection is subclinical, and subsequently 70% of the infected population develop serious opportunistic infections such as *Pneumocystis* pneumonia, carcinoma, etc. The symptoms include persistent generalized lymphadenopathy with a sharp drop in CD4+ T cell count to <200 cells/µl of blood. To get an insight into the infection process, the virus structure has to be understood. The viral coat is a lipid membrane which has protruding glycoprotein knobs [a]. The knobs are formed by trimers compromising two subunits: gp120 surface glycoprotein subunit which is exposed to the exterior and gp41 transmembrane glycoprotein which spans the viral membrane. The gp120 subunit has nine disulfide bonds and three are in the vicinity of the CD4+ binding domain of T lymphocyte serving as attractive sites for nanoparticle-viral interaction giving direction to HIV/AIDS Nanomedicine [2].

Till today, there is no specific treatment or vaccine available that suppresses HIV. A Combinational Anti-retroviral Therapy (cARTs) is in use that inhibits multiple viral targets [3]. The important issues related to HIV treatment includes the necessity of patient compliance to a very strict drug regimen, and the side effects associated with off-target exposure to antiretroviral drugs. This is exacerbated by the need for life-long commitment to medication. Also, HIV resides in various sites throughout the body, and there are both cellular and tissue sites that are particularly difficult for drugs to reach. Therefore, to succeed in therapy it is imperative to design means of overcoming these issues.

To date, investigations have resulted in the development of (i) Dendrimer based topical nano-microbicide, SPL7013 (VivaGel) that is non cytotoxic to Vero cells at a concentration as high as 10,000 µg/ml. (ii) A series of candidate solid drug nanoparticles (SDNs) that would allow dose reduction, therapy simplification, reduced cost of drug manufacture and potentially a lower frequency of adverse drug reactions [4]. (iii) Next generation lipid nanocarriers (NLCs) for HIV-AIDS treatment, generated using emulsion template freeze-drying technique. (iv) A number of polymer nanoparticles such as chitosan encapsulated tenofovir, which was well tolerated by vaginal epithelium; raltegravir and efavirez encapsulated in PLGA nanocarriers, that were seen to have mucus penetrating properties and were non-cytotoxic to HeLa cells. (v) Liposomes (eg MC-1220), a hydrophobic NNRTI encapsulated in carbopol liposomal gel, which showed 50-60% protection after SHIV challenge in macaque. (vi) Inorganic nanoparticle such as silver nanoparticles impregnated condoms, that were able to inhibit macrophage (M)- and T lymphocyte (T)-tropic HIV [5]. This development has opened a new door to male controlled nano-microbicides. (vii) Gold nanoparticles that inhibit HIV-1 infection by blocking reverse transcriptase activity. (viii) Nanofibres (eg. cellulose acetate phthalate) a

macromoleculer HIV-1 entry inhibitor with tenofovir that improved antiretroviral activity thereby preventing sexual transmission of HIV. Nanofibres are also under study for oral and parental administration of drug [6].

This nanocarrier-based approach provides flexibility for passive or active targeting; particularly to HIV-infected macrophages. This approach can result in strategies to combat resistance by improving bioavailability and targeting, thereby reducing pill burden while decreasing accumulation in tissues not infected by HIV [7]. With the advent on nanotechnology we look to a brighter future where hope prevails for the vast population suffering from HIV-AIDS.

Reference

[1] http://en.wikipedia.org/wiki/HIV/AIDS

[2] M.J. Forster, B.Mulloy,M.V.Nermut,Molecularmodelling study ofHIV p17gag(MA) protein shell utilising data from electron microscopy and X-ray crystallography, J. Mol. Biol. 298 (2000) 841–857.

[3] http://en.wikipedia.org/wiki/Antiretroviral_drugs

[4] Marco Siccardi et.al., Research Spotlight: Nanomedicines for HIV therapy, 20th Conference on Retroviruses and Opportunistic Infections, Atlanta, GA, (3-6 March 2013)

[5] J. Elechiguerra, J.L. Burt, J.R. Morones, A. Camacho-Bragado, X. Gao, H.H. Lara, M.J. Jose Yacaman, Interaction of silver nanoparticles with HIV-1, Nanobiotechnology 3 (2005) 1–10.

[6] Julianna Lisziewicz, Eniko R. Toke, Nanomedicine application towards the cure of HIV, Nanomedicine: Nanotechnology, Biology and Medicine 9 (2013) pg: 28-38.

[7] Researchers pioneer world's first HIV/AIDS nanomedicines, Kurzweil Accelerating Intelligence, News (September 3, 2012)

Detection and Treatment of Human Cancer: Nanotechnology Application a case study

ONYENANU I. U.[1], ONYIA C. I.[2], OKEKE F. C.[3], ADUBASIM C.A.[4]
[1] Department of Mechanical Engineering, School of Engineering, Anambra State University – Nigeria
[2, 4] Faculty of Sciences, Nnamdi Azikiwe University - Nigeria
[3] Faculty of Dentistry, College of Medicine, University of Nigeria, Enugu Campus
[1]mecury4eva@yahoo.co.uk, [2]chiagozie_onyia@yahoo.com, [3]franciscokeke88@hotmail.com, [4]angelaadubasim@yahoo.co.uk

ABSTRACT
Cancer is a complex disease caused by genetic instability and accumulation of multiple molecular alterations in human beings. Earlier efforts of diagnostic and prognostic classifications do not reflect the whole clinical heterogeneity of tumour and are insufficient to make predictions for successful treatment and patients' outcome. It may be noted that current advances in nanotechnology have offered new hope for cancer detection, prevention and treatment. Nanotechnology has wide-ranging applications such as drug synthesis and delivery, cell surgery and therapy, early disease diagnosis and prevention, biosensors and medical implants. Nanoparticles formulation are advantageous over conventional chemotherapy because they can incorporate multiple diagnostic and therapeutic agents and are associated with significantly less adverse effects due to selective accumulation to tumour tissue. Hence, nanoparticles can further be engineered to target specific tumour cells that express particular cell surface molecules. The selection of appropriate targets, component materials, formulation strategies and characterisation methods are critical to achieving successful outcomes. The study is geared towards reviewing aims at integrating some recent advances of nanotechnology with high potential for improving the cancer detection and treatment in humans.

Keywords: *Nanoparticles, molecular therapy, Nano medicine and nanotechnology.*

***1.0** Overview of Cancer*
Cancer medically known as malignant neoplasm is a broad group of various diseases, all involving unregulated cell growth. The major causes of cancer is; the genetic Instability and the accumulation of multiple molecular alterations in Human Being.

NB: It may be noted that Cancer remains a cause of considerable morbidity and mortality. It results to 13% of all deaths worldwide. It is also estimated that if current trends continues, there will be 22 million new cases of cancer worldwide occurring each year by 2030 *(Cancer Research UK 2013).*

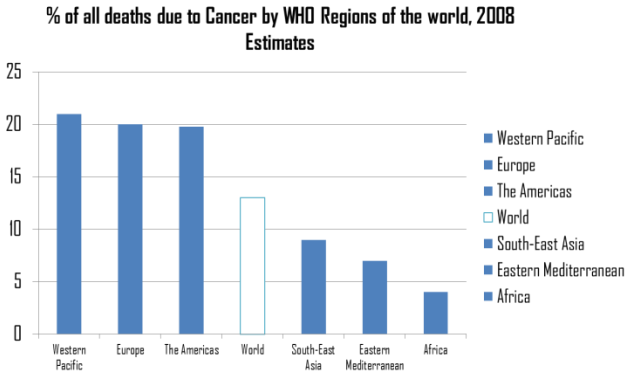

***1.1** Earlier methods of Cancer detection and treatment*
Before the introduction of Nanotechnology, Cancer was detected through early diagnosis and the Screening method which includes;

- The Papanicolau test for women to detect cervical cancer and mammography to detect breast cancer,
- Prostate-specific antigen (PSA) level detection in blood sample for men to detect prostate cancer
- Occult blood detection for colon cancer
- Endoscopy, CT scans, X-ray, ultrasound imaging and MRI for various cancer detection

***NB:** Most of these screening methods are quite costly and not available for many people.*

Table 1: showing the earlier ways of Cancer treatment and their limitations

S/N	Treatment Method	Limitations
1.	Surgery	Sometimes, Only part of the tumour can be removed
2.	Chemotherapeutics	Suffers from non-specific distribution with only a small fraction of drugs reaching the tumour.
3.	Radiation	Tissue damage occurs as a result of Radiation

Recently, the current advances in Nanotechnology have offered new hopes for cancer detection and treatment in Human Beings.

2.0 Nanotechnology and Cancer
The current advances in nanotechnology have offered new hope for cancer detection, prevention and treatment.

***2.1** Detection of Cancer using Nanotechnology*

Scanning and Imaging Cancerous Tumours: Imaging techniques, such as Magnetic Resonance Imaging (MRI) or Computed Tomography (CT) scans, can detect the presence of tumours in the body. Metal oxide nanoparticles, which generate a very strong signal on CT and MRI scans, can be coated with antibodies which bind to a certain receptors which are produced in greater quantities in cancerous cells than in normal cells. The nanoparticles would be concentrated around cancer cells, allowing cancerous tumours to be identified very easily.

Analysing Tissue Samples: If a patient is suspected to have cancer, the only way to verify it for sure is to take a biopsy - a sample of tissue which is analysed for biomarkers - characteristic chemicals created by the disease. A technique called a fluorescent immunoassay (FIA) attaches a fluorescent "label" chemical to these biomarkers, allowing the disease to be detected.

NB: An immunoassay using markers containing quantum dots could provide a much more detailed analysis of a blood or tissue sample.

Nanoscale cantilevers and nanowire sensors can detect biomarkers of cancer from a single cell, which heretofore was unimaginable. These tiny levers which are anchored at one end can be engineered to bind molecules that represent some of the changes associated with cancer.

***2.2** Treatment of Cancer using nanotechnology*

Nanotubes: An interesting property of nanotubes is that they absorb near infrared radiation. This causes them to heat up very quickly. Once the nanotube is attached to the cancer cells, Dai, uses a near infrared laser beams to heat nanotubes until it kills the cancer cells. This method is still at the testing stage.

Gold Nanoshells have a core of silica and a metallic outerlayer. These nanoshells can be injected safely as demonstrated in animal models. Because of their size, nanoshells will preferentially concentrate in cancer lesion sites. This physical selectivity occurs through a phenomenon called Enhanced permeation retention (EPR).

Finally, the nanoparticle method for direct cell destruction to be discussed is the magnetic nanoparticle hyperthermia method *(Jordan et al., 1999).* It is hypothesized that the relatively old concept of hyperthermia can be combined.

***2.3** Impact of Nanotechnology on Cancer Detection and Treatment*

- Nanotechnology protects drugs from being degraded in the body before they reach their target.
- It enhances the absorption of drugs into tumours and into cancerous cells themselves.
- It allows for better control over the timing and distribution of drugs to the tissue, making it easier for Oncologists to assess how well they work.
- It prevents drugs from interacting with normal cells, thus avoiding side effects.

2.4 Implications of Nanotechnology on Cancer Detection and Treatment.

- **Cost:** New technology often doesn't come cheaply, and so far nanomedicines are no exception although the increased costs come with documented advantages.
- **Need for biocompatible and stable Nanoparticles:** The ability to reproducibly manufacture nanomedicines at large scales with high levels of control over the physicochemical properties remains a major obstacle.
- **Environmental impact:** The same material properties that make nanoparticles appealing for cancer therapy and other applications have unintended effects on human health and the environment.

Conclusion

The current advances in nanotechnology have offered new hope for cancer detection, prevention and treatment. By combining the principles of Engineering, Computer, Chemistry and Medicine – particularly in the context of an improved understanding of fundamental biology – the field of nanotechnology will move closer to making the elusive 'magic bullet' a reality.

REFERENCES

1. National cancer Institute <http://nano.cancer.gov/learn/now/>
2. Jemal A, Siegel R, Xu J, Ward E. Cancer statistics, 2010. CA Cancer J Clin 2010; 60: 277–300.
3. Tanaka T, Decuzzi P, Cristofanilli M, *et al*. Nanotechnology for breast cancer therapy. Biomed Microdevices. 11(1):49-63. 2009 Feb.
4. Sharp PA, Langer R. Promoting convergence in biomedical science. Science; 333 (6042):527. 2011
5. Sunderland CJ, Steiert M, Talmadge JE, Derfus AM, Barry SE. Targeted nanoparticles for detecting and treating cancer. *Drug Development Research*. 67: 70-93; 2006
6. Triantafyllos S, Konstantinos S, Department of Mechanical and Manufacturing Engineering, University of Cyprus, Nicosia, Cyprus.. ISBN: 978-1-4673-4357-2. November 11-November 13

Nanotech Dubai 2013 International Conference and Exhibition

Synthesis of doxorubicin containing drug carriers and their in-vitro performance on HeLa and HCT116 cells

Christian Schmidt[1], Nurdan Doğangüzel[1,2], Stefanie Klöpzig[1], Sophia Rehfeldt[1], Sascha Behne[1], Raphael-Jose da Silva[1], Jens-Peter Krause[2], Mont Kumpugdee-Vollrath[2], Joachim Storsberg*[1]

[1]Fraunhofer Institute Applied Polymer Research (IAP), Geiselbergstrasse 69, 14476 Potsdam-Golm, Germany; [2]Department of Pharmaceutical Engineering, Beuth University of Applied Sciences Berlin, 13353 Berlin, Germany.

* Corresponding author: phone: +49331-568-1321; facsimile: +49-331 568-33-1321; email: joachim.storsberg@iap.fraunhofer.de.

Abstract

To further the options available for a more efficient anticancer therapy, we modified lipid carriers of the anticancer agent doxorubicin (Dox). In utilizing a previously reported differential sensitivity of HeLa and HCT116 cells to 1µM Dox, our results show a more than 50% decreased survival rate of the more resistant HeLa cells to 1µM Dox, delivered via our new carrier system; the blank carrier system does not impair the survival rate of the more sensitive HCT116 cells. This internally validated assay may be regarded as advantageous in determining the efficacy of drug delivery systems.

Keywords: drug carrier, efficacy, evaluation, cell culture, internal validation

Introduction

The delay-adjusted cancer death rate in the United States of America decreased more than 1% for both males and females in the time frame encompassing the years 2005 through 2009. Factors contributing to this decline include access to health care and advances in detection and/or treatment options for malignant lesions [1].

Leaving the issue of early-stage detection of tumors aside, delivery of the needed dosage of anticancer medication is a goal yet to be reached. Currently, much higher doses of drugs need to be administered to patients, leading to inconveniences caused by side effects. For example, patients have benefited from the anticancer activity of doxorubicin (Dox) for more than 30 years, although its inherent cardio-toxicity limits the dosages administered [2-4]. Concordantly, research efforts are directed at the development of systems to deliver drugs more efficiently to the target [5, 6]. One of these new formulations is a liposomal Dox formulation for intravenous injection purposes, which gained FDA approval [7, 8]. Caring physicians are, however, forced to reduce administered dosages of liposomal Dox due to profound to severe manifestations of the Palmar-Plantar Erythrodysesthesia [9, 10]. Examples of alternative nanoparticular-based Dox delivery systems already undergoing Phase III trials illustrate not only commercially viable

avenues but, more importantly, efforts to fully address the unmet clinical need of new drug delivery systems [11, 12].

How different dosages of Dox affect cancer cells is not fully understood. Complexity is added by observations where acute lymphoblastic leukemia cells (Molt-4) showed signs of apoptosis concomitant with RNA synthesis but no apparent sign of oxidative stress after twelve hours of exposure to the pharmacologically relevant concentration of 1μM Dox. Higher doses of Dox (> 3μM) led to a significyntly reduced apoptosis and administration of >100μM Dox resulted in inhibition of RNA polymerase and increased oxidative damage in the model system tested [13].

As our understanding of the molecular events leading to the development of cancerous lesions improves, more and more published evidence emerges in support of a so far not contested notion of an involvement of members of the p53 family in the many steps leading to the genesis of cancers, including but not limited to an aberrant function of p53 itself. As for p53, anomalous function of this tumor suppressor may be manifested in a wide range, including a functionally mutated form of p53 or even a complete loss of the p53 gene [14-17]. For example, degradation of p53 is targeted by the Human Papillomavirus (HPV) E6 oncogene in the case of invasive cervical cancers [18-21]. A direct consequence would be a reduced transcriptional activity of a p53 reporter plasmid in cells derived from such invasive cervical carcinoma. Using HeLa cells with their survival tied to the expression of E6, it was found that the p53 reporter plasmid appears to be more responsive to Dox treatment of the HPV negative HCT-116 cells in comparison to the HPV18 positive HeLa cells [22-26]. One logical extension of the above-discussed published evidence could be that HeLa cells are less susceptible to the effects of pharmacologically relevant doses of Dox (1μM) than HCT-116 cells.

To test this hypothesis, we treated HeLa and HCT-116 cells with Dox solubilized in growth medium or delivered via our new carrier system. Our results confirm a reduced sensitivity of HPV E6 positive HeLa to treatment with 1μM Dox in comparison to the HPV-negative HCT-116 cells. Furthermore, our results show that drug loaded nanoparticular carrier systems decrease the survival of HeLa cells by more than 50%, while unloaded nanoparticles do not impair the survival rate of the more sensitive HCT-116 cell line. In conclusion, our data support the notion of using an internally validated tissue culture system to test the efficacy of new anticancer drugs and/or delivery systems.

Body

1. Methods

We obtained all tissue culture plastic, from TPP, Trasadingen, Switzerland. The following sterile preparations were obtained from Biochrom AG, Berlin, Germany: DMEM [27], PBS without Mg^{2+}/Ca^{2+} [28], RPMI-1640 [29], FBS, ultrapure water, 100x stock solutions of sodium pyruvate, nonessential amino acids and Penicillin/Streptomycin and 10x stock solution of Trypsin/EDTA. HeLa and HCT116 cells (gifted by Dr. Norbert Nass, Otto-von-Guericke-University, Institute of Pathology, Magdeburg, Germany) were maintained in RPMI-1640 containing 10% heat-inactivated FBS [30], 4mM L-glutamin, 2mM sodium pyruvate and 500 U Penicillin and 500 U Streptomycin. Tissue culture, cryopreservation and thawing of cells were performed according to [31].

The following chemicals were used for the preparation of lipid-based carrier systems [32,33]: 2,6-di-tert-butyl-4-methylphenol (BHT, ACROS, Lot # A0203142), Soybean oil (Roth, Karlsruhe, Germany, Lot # 352187856), Cetyl palmitate (Roth; Lot # 452162569), Sodium tetradecyl sulfate (Alrdich, Munich, Germany, Lot # MKBK1230V), Miglyol 812 (Caesar & Loretz, Hilden, Germany, Lot # 12078605), Polysorbate 80 (Roth, Lot # 292187273 and 302187273), Lecitin (Roth, Lot # 312189810) and Doxorubicin (Molecula, Munich, Germany, Lot # 201249 and Sigma, Munich, Germany, Lot # SLBC8638V). We examined mean hydrodynamic particle size and zeta potential using samples diluted 1:2,500 in particle-free water as described [34]. For the in-vitro performance test of synthesized carrier systems on HeLa cells, we seeded 10^4 HeLa cells per cm^2 culture area on day -3 into a well of a 12-well plate and grew them for 3 days (until day 0) in 1ml of growth medium. On day 0, growth medium was replenished and supplemented with either Dox from a 10mg/ml stock solution in growth medium, or either loaded carrier system to deliver the amounts of Dox indicated in the figures or comparable amounts of unloaded carriers. Viable and dead cells were determined after incubation for 3 days (day 3) as described above. For tests involving HCT116 cells, we seeded $2.5x10^3$ HCT116 cells per cm^2 of culture area on day -2 into a well of a 12-well plate and grew them for 2 days (until day 0). On day 0, growth medium was replenished and supplemented as described above. Viable and dead cells were determined after incubation for 2 days (day 2) as described above. The relative survival rate of the cells is plotted in reference to untreated cells (set to 100%). All experiments were performed in triplicates with mean values and standard deviations plotted using Microsoft Excel®.

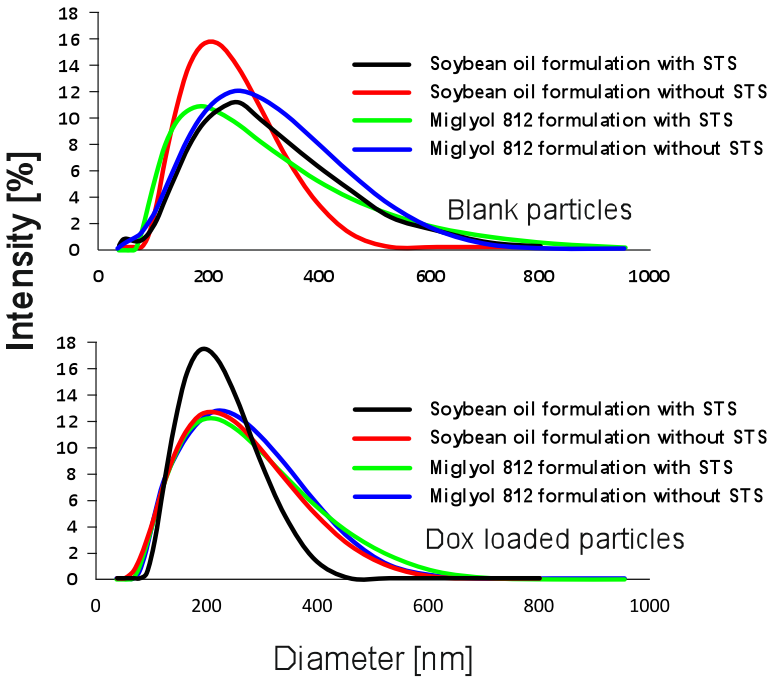

Figure 1: Mean hydrodynamic particle size distribution of freshly prepared delivery systems.

2. Synthesis and characterization of carrier systems

For carrier preparation, we followed [32] with modifications: The aqueous phase consisted of 15.2g water (supplemented to 0.1% Dox final concentration in the case of Dox loaded carriers), 2g polysorbate 80, whereas the lipid phase consisted of 300mg lecitin, 500mg BHT, 3.75g Cetyl palmitate and either 3.75g soybean oil or Migylol 812. Both phases were preheated in individual containers to 70°C under constant agitation on an IKA magnetic stirrer at 600 rpm. Over a time period of 15 min, we then added dropwise the aqueous phase to the lipid phase at a constant temperature of 70°C under constant agitation at 600 rpm, followed by 5 min of further agitation at 70°C. As preparation for the sonication step, we removed the heat source and stirred the mixture until room temperature (25°C) was reached. The mixture was sonicated 5 times for 5min each with a 10sec break between individual sonication steps (40%

amplitude on a Sonoplus Mini 20 from Brandt Electronics). Final adjustments of the pH to 8 ± 0.1 were performed with 1M NaOH followed by successive passages of the product through 1µm and 0.45µm membrane filters. STS was added to the preparation at a molar ratio of 1mol Dox to 1.25 mol STS followed by incubation for 3 days at 4°C in the dark and subsequent sonication for 3min (40% amplitude on a Sonoplus Mini 20 from Brandt Electronics), according to [33].
At first, we assayed for mean hydrodynamic particle size distribution [34] directly after completion

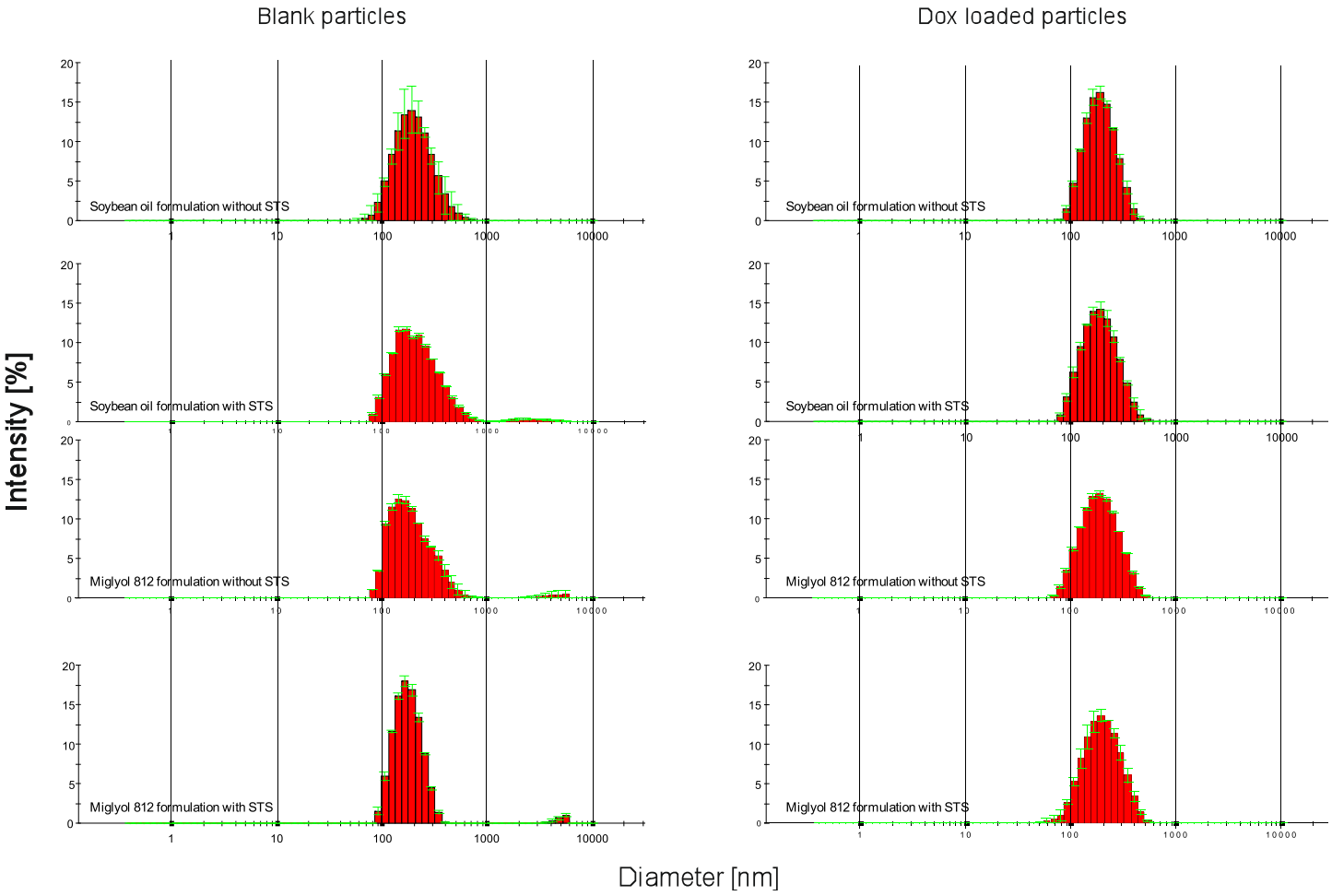

Figure 2: Mean hydrodynamic particle size distribution of delivery systems after 7 months of storage at 4°C in the dark.

of particle synthesis (Figure 1). In agreement with [33], the mean hydrodynamic particle size of the materials after synthesis was determined to be around 200 nm and of unimodal distribution (Figure 1). Another determination of the mean hydrodynamic particle size was performed to address one of the major limitations of drug delivery systems created by emulsion techniques, the susceptibility of the particles to Ostwald ripening [35, 36]. As shown in Figure 2, no profound changes in the mean hydrodynamic particle size of the particles was detected after 7 months of storage at 4°C in the dark. This virtually unchanged mean hydrodynamic particle size distribution of the filtration sterilized formulation of drug carriers lends support to the recommendation of [33] to use filtration through a 0.22µm membrane filter as sterilization method for this particular formulation of drug carriers. By extension, this result ties in nicely with the notion that sterilization methods of drug carrier formulations should be determined on a case-by-case manner [33].

The zeta potential of Dox loaded soybean-based carriers changed to -37.92 ± 0.86 mV from -52.36 ± 0.34 mV for unloaded particles. As for miglyol-based carriers, Dox-loading altered the zeta potential from -35.54 ± 0.26 mV from the blank reference to -27.98 ± 0.92 mV. These results suggest that loading of either carrier system with Dox resulted in a decreased negative charge with a calculated respective absolute difference of 14.44 mV for the soybean-based formulation and 7.96 mV for miglyol-based carriers. This decrease in negativity in response to Dox loading of carrier systems is also in agreement with observations of different carrier systems [35], although differences in the absolute numbers may be attributed to the properties of the individual system. Taken together, our results are in agreement with published evidence and support the notion that the synthesized carrier systems were successfully loaded with Dox.

To further describe the carrier formulations obtained, we assayed for the release of Dox by means of dialysis assays [36]. In brief, we placed 5ml of the indicated drug carriers (equal amounts of Dox loaded) in a dialysis bag (Mw cut off: 4 to 6Da, thickness: 28µm and with a nominal filter rate of 3.5, obtained from Roth) and dialyzed this against a constant volume of 25ml buffer (pH 7.4) consisting of 10 vol-% ethanol, 15 vol-% polysorbate 80 and 70 vol-% Sorensen buffer under constant agitation at 600 rpm at 37°C [37, 38]. At time points 1, 2, 4, 7, 24, 32 and 48h, 2ml of the medium was drawn to determine the amount of Dox by comparing the optical density of a reference to the sample. Plotting [Dox] in µM against time in hours resulted in the graph shown in Figure 3. As shown in Figure 3, both preparations displayed a sigmoidal drug release profile as assayed via a dialysis assay. This ties in well with published evidence of an observed sigmoidal release of a model compound, phenyl isothiocyanate, from chitosan-encapsulated solid lipid nanoparticles made of stearic acid, Tween-80 and sodium taurocholate [39]. Our observations indicate that the Dox release from miglyol-based carrier systems reached the first plateau of the release profile at approximately 7h compared to 4h in the case of soybean oil-based formulations. Both formulations showed a sigmoid Dox release between 24 and 32 h. Notably, an initial burst of released drug is seen in the release profile of both drug carrier systems. In agreement with published literature [40], our interpretation of this observation is that the unrestricted diffusion of the drug through the drug delivery system into the surrounding medium is the rate-limiting step.

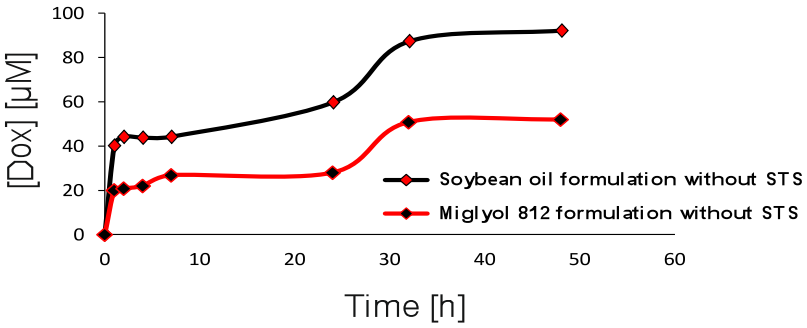

Figure 3: Release of Dox as a function of time in a dialysis assay.

3. In vitro performance of synthesized carrier systems on HeLa and HCT116 cells

Effects caused by recognition of and reaction with intravenously administered carrier systems by the phagocytic system may result in undesirable responses of a patient to treatment approaches [41]. Using solid lipid nanoparticles and primary mouse peritoneal macrophages, Schöler et al. [42] found that medium concentrations up to 0.1% of carrier formulations based on soybean oil, lecithin and tween 80 and with particle sizes ranging from around 200nm to 5µm did not reduce the viability of primary murine peritoneal macrophages after 20h incubation as assayed by MTT

tests. In support of [25], HeLa cells did not respond to 1μM Dox with a reduced survival rate in comparison to 0.1μM Dox throughout our assays, whereas HCT116 cells display a roughly 5 fold decreased survival in the presence of 1μM Dox in comparison to 0.1μM Dox (Figures 4 and 5). To account for the cytotoxic properties of empty carrier systems, we added comparable amounts of empty carriers as were needed to the delivery of the concentration of Dox in the indicated treatments with loaded nanoparticles. As shown in Figure 4 for soybean oil-based carrier systems, delivery of 0.1μM Dox increased the killing efficiency 3 fold in the case of HeLa cells and nearly 5 fold for HCT116 cells in comparison to free Dox in growth medium. Miglyol-based drug carriers, however, proved to be less effective in the killing of HeLa (decrease by 2 fold at 1μM Dox) and HCT116 cells (decrease by 2 fold at 0.1μM Dox) in comparison to free Dox in growth medium). In sum, the results depicted in Figure 4 suggest that soybean oil-based and Dox loaded carrier systems display a higher efficacy than miglyol-based drug delivery systems.

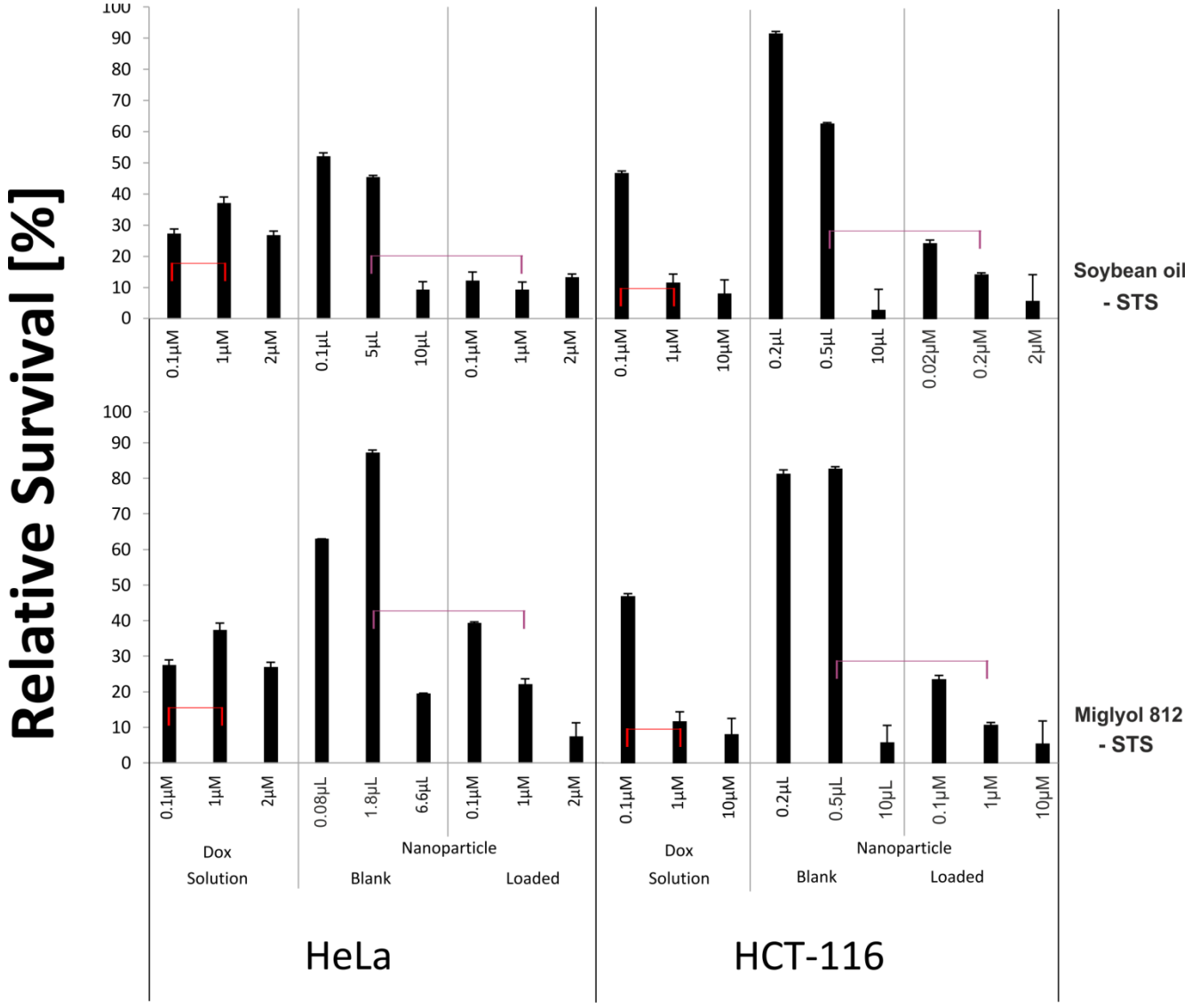

Figure 4: In vitro performance of soybean oil or miglyol-based carrier systems on HeLa and HCT116 cells.

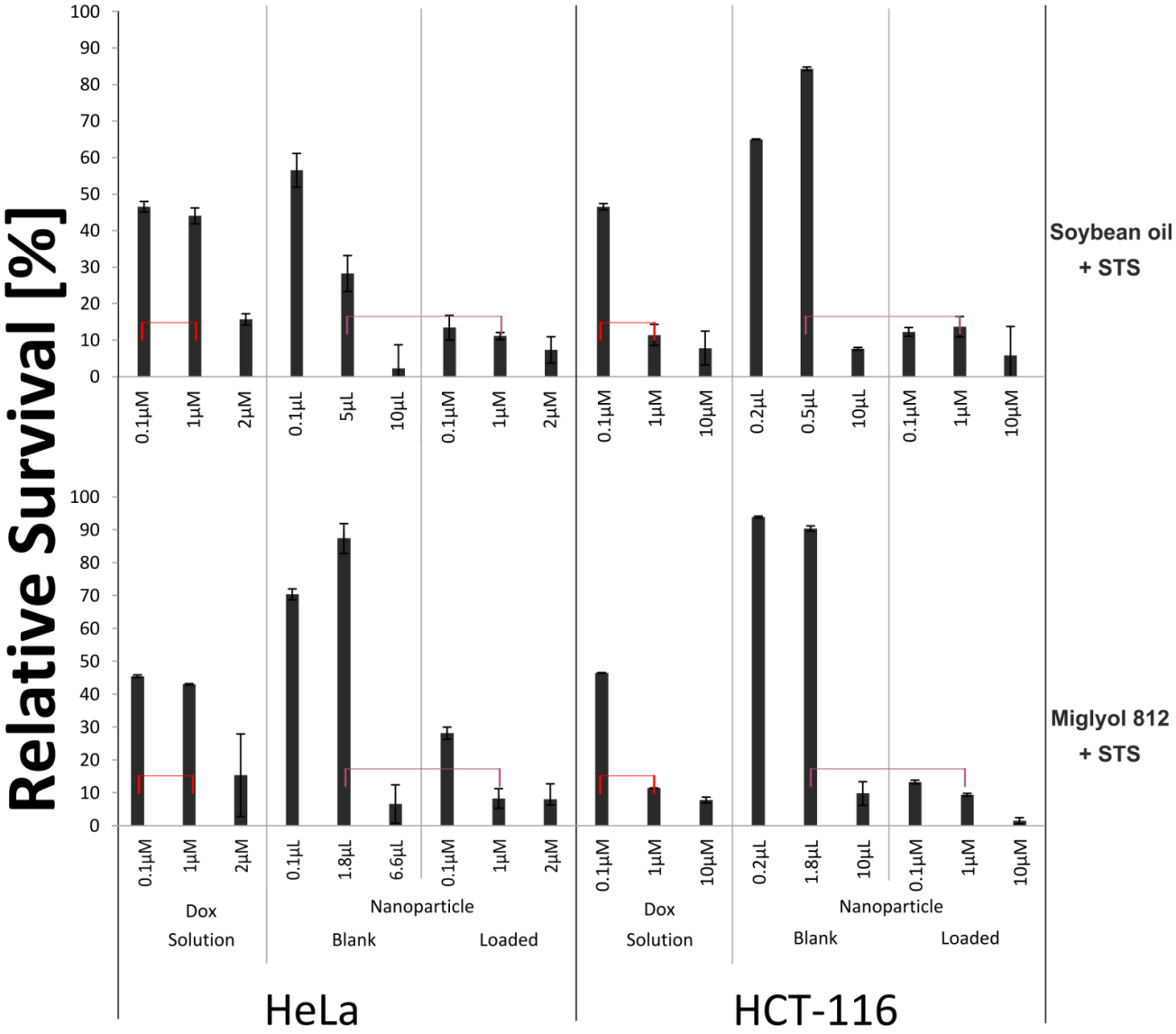

Figure 5: In vitro performance of STS containing soybean oil or miglyol-based carrier systems on HeLa and HCT116 cells.

As shown in Figure 5 for STS/soybean oil-based carrier systems, delivery of 0.1μM Dox increased the killing efficiency 5 fold in the case of HeLa and HCT116 cells in comparison to free Dox in growth medium. Miglyol-based drug carriers, however, proved to be less effective in the killing of HeLa (decrease by 2 fold at 1μM Dox) and HCT116 cells (decrease by 5 fold at 0.1μM Dox) in comparison to free Dox in growth medium). In sum, these results (Figures 4 and 5) suggest that the killing efficacy of HeLa cells by soybean oil-based carrier systems increased when STS is present in the carrier formulation. This, however, cannot be observed in the case of miglyol-based formulations.

Conclusion

Here we show the synthesis and characterization of sovbean oil or miglyol-based drug carrier systems with an unchanged particle size of around 200nm regardless of loading with doxorubicin and/or storage for 7 months at 4°C in the dark. Addition of STS at a molar ratio of 1mol Dox to 1.25 mol STS increased the killing efficacy of the doxorubicin-resistant cell line HeLa as well as a

doxorubicin-sesitive cell line (HCT116) using soybean oil-based carrier systems but not the miglyol-based drug delivery systems. These observations present an advantage over existing literature where a nontoxic drug carrier system is reported to overcome the doxorubicin resistance in MDA-MB 231 cells but appears to be less efficient in killing a doxorubicin-sensitive cell line (MCF-7) [43].

References:

[1] Siegel R, Naishadham D, Jemal A.Cancer statistics, 2013. CA Cancer J Clin 2013; 63: 11-30.

[2] Tacar O, Sriamornsak P, Dass CR. Doxorubicin: an update on anticancer molecular action, toxicity and novel drug delivery systems. J Pharm Pharmacol 2013; 65: 157-70.

[3] Ho J, Zhang L, Todorova L, Whillans F, Corey-Lisle P, Yuan Y.Budget impact analysis of ixabepilone used according to FDA approved labeling in treatment-resistant metastatic breast cancer. J Manag Care Pharm 2009; 15: 467-75.

[4] Bauer RL, Busch E, Levine E, Edge SB. Therapy for inflammatory breast cancer: impact of doxorubicin-based therapy. Ann Surg Oncol 1995; 2: 288-94.

[5] Galandrin S, Oligny-Longpré G, Bouvier M. The evasive nature of drug efficacy: implications for drug discovery. Trends Pharmacol 2007; 28: 423-30.

[6] Allen TM, Cullis PR. Drug delivery systems: entering the mainstream. Science 2004; 303: 1818-22

[7] Carlson RH. End of the line for Bevacizumab in breast cancer? Oncology Times 2013; 35: 24-5.

[8] Barenholz Y. Doxil®--the first FDA-approved nano-drug: lessons learned. J Control Release 2012; 160: 117-34.

[9] Farr KP, Safwat A. Palmar-plantar erythrodysesthesia associated with chemotherapy and its treatment. Case Rep Oncol 2011; 4: 229-35.

[10] Lokich JJ, Moore C. Chemotherapy-associated palmar-plantar erythrodysesthesia syndrome. Ann Intern Med 1984; 101: 798-9.

[11] Batist G, Barton J, Chaikin P, Swenson C, Welles L. Myocet (liposome-encapsulated doxorubicin citrate): a new approach in breast cancer therapy. Expert Opin Pharmacother 2002; 3: 1739-51.

[12] Needham D, Dewhirst MW. The development and testing of a new temperature-sensitive drug delivery system for the treatment of solid tumors. Adv Drug Deliv Rev 2001; 53: 285-305.

[13] Müller I, Jenner A, Bruchelt G, Niethammer D, Halliwell B. Effect of concentration on the cytotoxic mechanism of doxorubicin--apoptosis and oxidative DNA damage. Biochem Biophys Res Commun 1997; 230: 254-7.

[14] Wang X, Wang HK, McCoy JP, Banerjee NS, Rader JS, Broker TR, Meyers C, Chow LT, Zheng ZM. Oncogenic HPV infection interrupts the expression of tumor-suppressive miR-34a through viral oncoprotein E6. RNA 2009; 15: 637-47.

[15] Solomon H, Madar S, Rotter V. Mutant p53 gain of function is interwoven into the hallmarks of cancer. J Pathol 2011; 225: 475-8.

[16] Igney FH, Krammer PH. Death and anti-death: tumour resistance to apoptosis. Nat Rev Cancer 2002; 2: 277-88.

[17] Hanahan D, Weinberg RA. The hallmarks of cancer. Cell 2000; 100: 57-70.

[18] Parkin DM. The global health burden of infection-associated cancers in the year 2002. Int J Cancer 2006; 118: 3030-44.

[19] Hietanen S, Lain S, Krausz E, Blattner C, Lane DP. Activation of p53 in cervical carcinoma cells by small molecules. Proc Natl Acad Sci USA 2000; 97: 8501-6.

[20] Walboomers JM, Jacobs MV, Manos MM, Bosch FX, Kummer JA, Shah KV, Snijders PJ, Peto J, Meijer CJ, Muñoz N. Human papillomavirus is a necessary cause of invasive cervical cancer worldwide. J Pathol 1999; 189: 12-9.

[21] Crook T, Tidy JA, Vousden KH. Degradation of p53 can be targeted by HPV E6 sequences distinct from those required for p53 binding and trans-activation. Cell 1991; 67: 547-56.

[22] Kelley ML, Keiger KE, Lee CJ, Huibregtse JM. The global transcriptional effects of the human papillomavirus E6 protein in cervical carcinoma cell lines are mediated by the E6AP ubiquitin ligase. J Virol 2005; 79: 3737-47.

[23] Masters JR. HeLa cells 50 years on: the good, the bad and the ugly. Nat Rev Cancer 2002; 2: 315-9.

[24] Scherer WF, Sylverton JT, Gey GO. Studies on the propagation in vitro of poliomyelitis viruses. IV. Viral multiplication in a stable strain of human malignant epithelial cells (strain HeLa) derived from an epidermoid carcinoma of the cervix. J Exp Med 1953; 97: 695-710.

[25] Kochetkov DV, Il'inskaia GV, Komarov PG, Strom E, Agapova LS, Ivanov AV, Budanov AV, Frolova, EI, Chumakov PM. Transcriptional inhibition of human papilloma virus in cervical carcinoma cells reactivates functions of the tumor suppressor p53. Mol Biol (Mosk) 2007; 41: 515-23.

[26] Wang Y, Solt LA, Kojetin DJ, Burris TP. Regulation of p53 stability and apoptosis by a ROR agonist. PLoS One 2012; 7: e34921.

[27] Dulbecco R, Freeman G. Plaque production by the polyoma virus. Virology 1959; 8: 396-7.

[28] Dulbecco R, Vogt M. Plaque formation and isolation of pure lines with poliomyelitis viruses. J Exp Med 1954; 99: 167-82.

[29] Horwitz MA, Silverstein SC. Legionnaires' disease bacterium (Legionella pneumophila) multiples intracellularly in human monocytes. J Clin Invest 1980; 66: 441-50.

[30] Soltis RD, Hasz D, Morris MJ, Wilson ID. The effect of heat inactivation of serum on aggregation of immunoglobulins. Immunology 1979; 36: 37-45.

[31] Karlsson JO, Eroglu A, Toth TL, Cravalho EG, Toner M. Fertilization and development of mouse oocytes cryopreserved using a theoretically optimized protocol. Hum Reprod 1996; 11: 1296-305.

[32] Chinsriwongkul A, Chareanputtakhun P, Ngawhirunpat T, Rojanarata T, Sila-on W, Ruktanonchai U. Opanasopit P. Nanostructured lipid carriers (NLC) for parenteral delivery of an anticancer drug. AAPS Pharm Sci Tech 2012; 13: 150-8..

[33] Ma P, Dong X, Swadley CL, Gupte A, Leggas M, Ledebur HC, Mumper RJ. Development of idarubicin and doxorubicin solid lipid nanoparticles to overcome Pgp-mediated multiple drug resistance in leukemia. J Biomed Nanotechnol 2009; 5: 151-61.

[34] Burapapadh K, Kumpugdee-Vollrath M, Chantasart D, Sriamornsak P. Fabrication of pectin-based nanoemulsions loaded with itraconazole for pharmaceutical application. Carbohydr Polym 2010; 82: 384-93.

[35] Jain TK, Richey J, Strand M, Leslie-Pelecky DL, Flask CA, Labhasetwar V. Magnetic nanoparticles with dual functional properties: drug delivery and magnetic resonance imaging. Biomaterials 2008; 29: 4012-21.

[36] Cai S, Thati S, Bagby TR, Diab HM, Davies NM, Cohen MS, Forrest ML. Localized doxorubicin chemotherapy with a biopolymeric nanocarrier improves survival and reduces toxicity in xenografts of human breast cancer. J Control Release 2010; 146: 212-8.

[37] Sorensen B, Serjsen P. Saline solutions in the treatment of burn shock. Acta Chir Scand 1965; 129: 239-49.

[38] Realini N, Solorzano C, Pagliuca C, Pizzirani D, Armirotti A, Luciani R, Costi MP, Bandiera T, Piomelli D. Discovery of highly potent acid ceramidase inhibitors with in vitro tumor chemosensitizing activity. Sci Rep 2013; 3:1035.

[39] Dharmala K, Yoo JW, Lee CH. Development of chitosan-SLN microparticles for chemotherapy: in vitro approach through efflux-transporter modulation. J Control Release 2008; 131: 190-7.

[40] Huang X, Brazel CS. On the importance and mechanisms of burst release in matrix-controlled drug delivery systems. J Control Release 2001; 73: 121-36.

[41] Allen TM. Toxicity of drug carriers to the mononuclear phagocyte system. Adv Drug Delivery Rev 1988; 2: 55-67.

[42] Schöler N, Olbrich C, Tabatt K, Müller RH, Hahn H, Liesenfeld O. Surfactant, but not the size of solid lipid nanoparticles (SLN) influences viability and cytokine production of macrophages. Int J Pharm 2001; 221: 57-67.

[43] Aroui S, Ram N, Appaix F, Ronjat M, Kenani A, Pirollet F, De Waard M. Maurocalcine as a non toxic drug carrier overcomes doxorubicin resistance in the cancer cell line MDA-MB 231. Pharm Res 2009; 26: 836-45.

The importance of polar facets for gas sensing in ZnO nanostructures

Mohammad R. Alenezi[1,2], Abdullah S. Alshammari[1], K. D. G. I. Jayawardena[1], Michail J Beliatis[1], Simon J. Henley[1], and S. R. P. Silva[1]
1. Nanoelectronics Center, Advanced Technology Institute, University of Surrey, Guildford, GU2 7XH, (UK)
2. Department of Electronics, College of Technological Studies, PAAET, P.O. Box 42325, Shuwaikh, Kuwait
m.alenezi@surrey.ac.uk

Highly functional materials for use in technology applications can be fabricated by recognizing the importance of morphology, property, and application relationship. Gas sensors are of substantial interest amongst these applications because of their essential role in many important fields including; industrial process control, safety systems, disease diagnoses, and environmental monitoring. [1,2]

ZnO is a wurtzite-structured crystal and can be described as a number of alternating planes consisting of tetrahedrally coordinated O^{2-} and Zn^{2+} ions stacked alternatively along the c-axis.[17] Such structure type causes a divergence in the surface energy of polar (0001) surface, and a strong anisotropy in the growth rate *v*, such as *v* [0001] >> *v* [10$\bar{1}$0]. As a result, wurtzite-type ZnO nanostructures usually tend to minimize the exposed areas of the {0001} polar facets which possess high surface energy, and maximize the exposed areas of the {10$\bar{1}$0} nonpolar facets. However, by tuning the growth process, the exposed facets of the ZnO nanostructured can be controlled. [2]

Different groups studied the effect of morphology and size of metal oxide nanostructures on their ability to sense gases.[1-4] Nevertheless, the exact role of the exposed facets on the gas sensing properties is not well studied until now, which is believed is due to the limited ability over the morphology of metal oxide nanostructures.[5] Hence it is challenging to attribute and correlate the effect of the exposed crystal surfaces of metal oxide nanostructures to their gas sensing properties.

In this work, nanostructured gas sensors were fabricated based on hydrothermally synthesized single crystal ZnO nanostructures with different morphologies, including nanowires (ZNWs), NDs (ZNDs), and nanostars (ZNSs) as shown in figure 1(a)-(c), respectively. ZNWs are single crystals growing along the [0001] direction as confirmed by the selected area electron diffraction (SAED) pattern in the inset of figure 1(a) and their side surfaces are nonpolar {10$\bar{1}$0} planes. The SAED pattern of the ZNDs, shown in the inset of figure 1(b), confirms that they are single crystals.

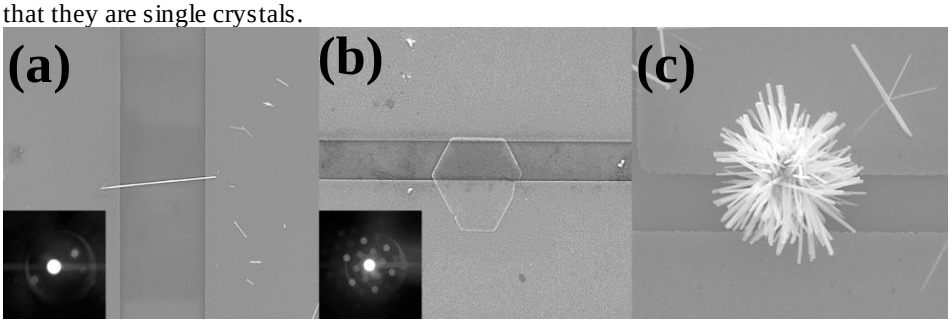

Figure 1. SEM images of (a) ZNWs (inset: SAED pattern), (b) ZNDs (inset: SAED pattern), and (c) ZNSs. (5 μm spacing between the electrodes)

The three gas sensors were tested at different temperatures to find out the optimum operating condition for ethanol detection. Figure 2(a) shows responses of the three the sensors to 200 ppm ethanol at different operating temperatures. All responses are found to increase with increasing operating temperature, with a maximum response for ZNW, ZND, and ZNS sensors being observed at 300, 350, and 300 °C respectively, and then decrease with a further rise of operating temperature. This effect of the operating temperature on the sensitivity can be explained with regards to the kinetics and mechanics of gas adsorption and desorption on the surface of ZnO.[6] At low operating temperature, the sensor chemical activation is small, which leads to small response. When the operating temperature is increased beyond a threshold value, some adsorbed gas molecules may escape before the charge transfer due to their enhanced activation, thus the response will decrease correspondingly. It is clear that the sensitivity of ZNDs is significantly higher than those of the ZNWs and ZNSs under all operating temperatures. For the example, the sensitivity of ZND sensor reaches 29 at 350 °C, while the sensitivities of ZNW and ZNS sensors are 11 and 17, respectively.

Response versus ethanol concentration curves of three thermally activated gas sensors at 350 ˚C are shown in figure 2(b). For ethanol at levels of 100, 300 and 500 ppm, the ZND sensor responses are 20, 37, and 48, respectively. The ZNW responses to the same ethanol levels are 6.5, 14.5 and 20.5, respectively, while the responses of the ZNS sensor to the same ethanol levels are 11, 22.5 and 32.5, respectively. Furthermore, we note that ZNW and ZNS sensors do not show any sensitivity to ethanol at levels below 20 ppm.

Figures 2(c) shows the responses of the ZND sensor to ethanol concentration levels from 1 ppm to 500 ppm. The response time and recovery time for the ZND sensor to 100 ppm ethanol are about 11 and 15 s, respectively. With the increase in ethanol concentration, the response time decreases gradually. The response times are calculated to be approximately 8 s for 300 ppm ethanol and 6 s for 500 ppm ethanol. The decrease in response time can be explained by the variation of the saturation time (the time required for complete coverage of the sensor surface by the ethanol molecules) and the mean residence period of ethanol molecules on the nanodisk surface. At

low ethanol concentrations, the time required for the complete reaction of the oxygen species and ethanol molecules is long, leading to a longer response time.

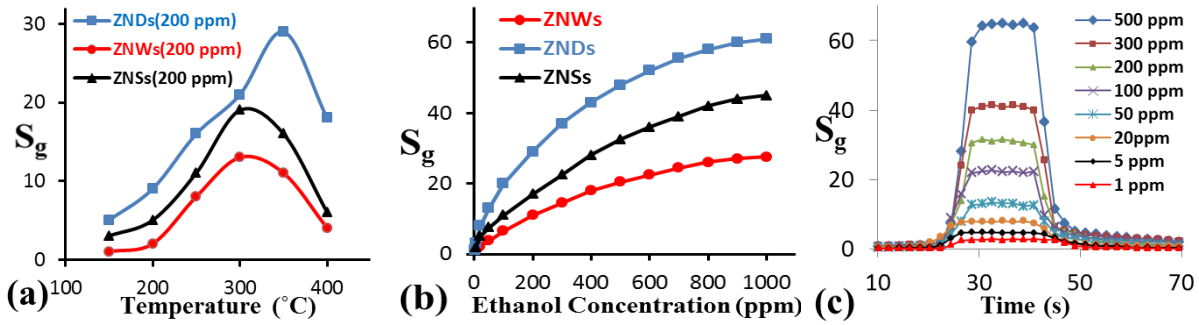

Figure 2.(a) Responses of ZNW, ZND and ZNS sensors to 200 ppm of ethanol at different temperatures, (b)) Response vs. time curves of ZNW, ZND and ZNS sensors to different ethanol concentrations at 350 °C, and (c) responses of the ZND sensor to ethanol concentration levels from 1 to 500 ppm at 350 °C.

Even though the surface-to-volume ratio of the ZND sensor (~ 10) is similar to that of the ZNW sensor (~ 10), our results clearly indicate that the performance characteristics of the gas sensor based on ZND are superior to those of the ZNW and ZNS sensors. Based on the morphological and structural analysis of the ZnO nanostructures and considering their different features, it is proposed that the gas sensing ability of ZnO nanostructures is closely related to those of exposed surface structures.

In general, gas sensing in metal oxides is a solid-gas interfacial reaction process that can affect its conductivity. Chemical adsorption and reaction of target molecules occurring on the surface of metal oxide semiconductors are important factors in its ability to sense gases. The O 1s XPS peaks of the three different ZnO nanostructures are found to be different. All peaks are asymmetric and present a visible shoulder. As shown in figure 3(a)-(d), each O 1s XPS peak can be decomposed into three Gaussian components centered at ~ 530.1 ± 0.15 eV (O_L), 531.5 ± 0.2 eV (O_V), and 532.5 ± 0.15 eV (O_C). As reported before,[7,8] the O_L component of O 1s spectrum is attributed to O^{2-} ions on wurtzite structure of hexagonal Zn^{2+} ion array, surrounded by Zn atoms with their full complement of nearest-neighbour O^{2-} ions. This means that the quantity of oxygen atoms in a fully oxidized stoichiometric surrounding can be measured by the intensity of this component. The medium binding energy component O_V is associated with O^{2-} ions in oxygen-deficient regions within the matrix of ZnO, while the O_C component is usually attributed to chemisorbed and dissociated oxygen species. Thus, the oxygen-chemisorbed ability of different exposed facets in ZnO crystal can be estimated based on the intensity of O_C component in the O 1s XPS peak. The relative percentages of the O_C component in the three nanostructures are approximately 3% (ZNWs), 15% (ZNDs), and 6.5% (ZNSs), which indicates that ZNDs may absorb more oxygen species than ZNWs and ZNSs. Apparently the gas sensing properties of ZnO are closely related to the chemisorption ability of the crystal surfaces.

Absorbing oxygen species and target molecules depend on the surface atomic structures. The Zn-terminated (0001) facet is capable of seizing atmospheric oxygen (O_2) through physical/chemical absorption due to unsaturated oxygen coordination and therefore possesses the highest chemsorption capability. The exposed facets of ZNDs are the (0001) facets and as a result show the highest gas sensing performance. On the other hand, the dominating exposed surfaces of ZNWs and ZNSs are the nonpolar {10$\bar{1}$0} planes with equivalent Zn atoms and O atoms in the same plane, so their gas sensing properties are not as good as the (0001) plane. Hence, the gas sensing properties of the ZnO crystal facets are (0001) > {10$\bar{1}$0}.

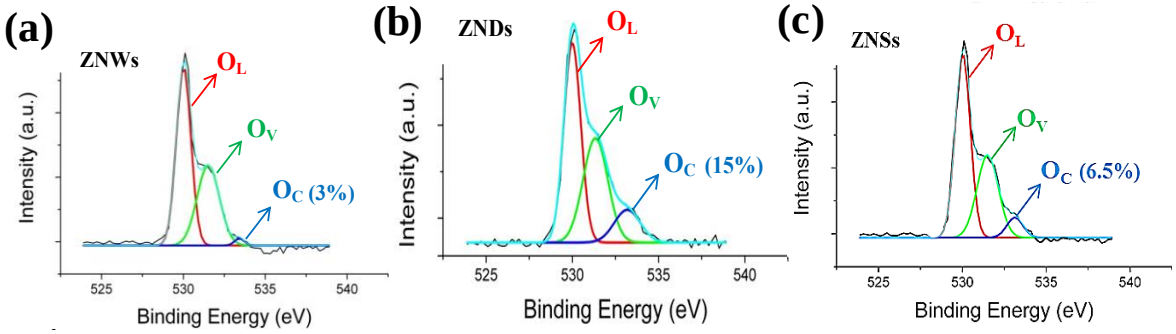

Figure 3. XPS spectra of (a) ZNWs, (b) ZNDs, and (c) ZNSs.

References

[1] Greene, L. E.; Yuhas, B. D.; Law, M.; Zitoun, D.; Yang, P. Inorg. Chem. **45**, (2006), 7535.
[2] Mohammad R. Alenezi, Simon J. Henley, Neil G. Emerson, S. Ravi P. Silva, Nanoscale, (2013) DOI: 10.1039/C3NR04519F
[3] Jayawardena, K. D. G. I.; Opoku, C.; Fryar, J.; Silva, S. R. P.; Henley, S. J. Applied Surface Science. **257,** (2010), 5274
[4] Rider, K. B.; Hwang, K. S.; Salmeron, M.; Somorjai, G. Am. J. Chem. Soc. **124**, (2002), 5588.
[5] Tillekaratne, A.; Siap, D.; Trenary, M. J. Phys. Chem. C **112**, (2008), 8682.
[6] Herrán, J.; Fernández-González, O.; Castro-Hurtado, I.; Romero, T.; Mandayo, G. G.; Casta˜no, E. *Sens. Actuators B Chem.* **149**, (2010),368–372.
[7] Xu, J. Q.; Pan, Q. Y.; Shun, Y. A.; Tian, Z. Z.; *Sens. Actuators, B* **66**, (2000), 277.
[8] A´. Ne´meth, E. Horva´th, Z. La´badi, L. Feda´k, I. Ba´rsony, *Sens. Actuators B* **127**, (2007), 157-160.

SETCOR International Nanotechnology conference 2013
NANOTECH DUBAI 2013

Preparation and Physicochemical characterization of Multi Walled Carbon Nanotube embedded SU-8 electrospun nanofibers

Durga Prakash M[1], Siva Rama Krishna V[1], Shivgovind Singh[1], Asudeb Dutta[1], and C. S. Sharma[2]
[1]*Department of Electrical Engineering, Indian Institute of Technology Hyderabad, Hyderabad, India*
[2]*Department of Chemical Engineering, Indian Institute of Technology Hyderabad, Hyderabad, India*
[1,2]E-mail: {ee10p005, svanjari, sgsingh, asudeb_dutta, cssharma}@iith.ac.in

Abstract We reported here the electrospinning preparation and physicochemical characterization of multi walled carbon nanotube (MWCNT) embedded SU-8 derived nanofibers. These nanofibers are deposited on a copper microelectrode array fabricated on a glass substrate using electrospinning technique, a simple, robust and yet a cost effective way of producing nanofibers. Specifically for biosensor applications SU-8 derived nanofibres are best suited as they combine the advantages of nanofibres viz high surface area abudance of active site with SU-8 biocompatibility and ability to functionalize its surface with simple chemical/plasma treatment. However their high resistivity hampers them from using in impedance based or ISFET based sensors. In this work MWCNTs were dispersed in chloroform and mixed with SU-8. The mixture is then electrospun onto copper electrode array which is fabricated using a standard lift off process. The parameters of electrospinning are optimized for placing nanofibers in between two electrodes of the array. The morphologies of the as-spun MWCNT embedded SU-8 derived nanofibers were observed by scanning electron microscopy. The interaction between MWCNTs and SU-8 in the electrospun nanofibers was studied by XRD spectra and Raman spectra analysis. Our study further heat treatment confirms the remarkable synergistic effect of MWCNTs and SU-8 on the significant improvement of the conductivity of electrospun, as well as the increase in hydrophilic nature of the nanofiber surface. Under an optimal experimental condition, the created after heat treatment of MWCNTs embedded SU-8 derived nanofiber has a conductivity of 73.8007 S/m, a wide linear range from -0.5 to 0.5 volts, which indicates that this novel and simple strategy for fabricating electrochemical sensor by an electrospinning technique has wide potential applications in bio-analysis and detection

Keywords: MWCNTs; SU-8; Nanofiber; Electrospinning; Microelectrode array

1. Introduction

One-dimensional nanomaterials, such as nanofibers, nanowires, nanobelts, nanoribbons, and nanorods, are a new class of nanomaterials that have been attracting a great research interest in the last few years. These materials have been demonstrated to exhibit superior optical, acoustic, electrical, magnetic, thermal, and mechanical properties, and thus, can be used as both interconnects and functional components in the fabrication of nanoscale electronic and biosensing devices [1]. Electrospinning is a simple method to produce nanofibers by applying a high electric field to a polymer solution which causes an ejection of polymer jet. The solvent in the polymer solution evaporates leading to nanofibers of precise dimensions based on the applied input conditions [2-6]. The schematic of electrospinning is shown in Fig.1. Typically a high voltage of the order of 5- 20 kV is applied between needle of a metal syringe containing the polymer solution and a rotating collector. This voltage charges the polymer solution. The surface tension force acting on the droplet at the edge of the needle is counteracted by the electrostatic repulsion force, resulting in the stretching of the droplet. Beyond a particular voltage, polymer jet erupts from the surface and the solvent of polymer solution gets evaporated before it gets collected on the collector. The dimensions of the fibers collected are in few hundreds of nanometers and it depends on number of parameters mainly, the viscosity and electric conductivity of the polymeric fluids, and the applied voltage.

Nanofibers can be produced with a variety of polymers depending on the application. SU-8 is a negative epoxy photoresist which is biocompatible and its surface can be easily functionalized [7]. Nanofibers derived out of SU-8 can potentially be used as high sensitive biosensors. However, the resistivity of SU-8 is really high which causes the nanofibers derived out of it to be highly resistive. Researchers have employed pyrolysis technique to carbonize SU-8 which results in enhanced conductivity [8]. These high temperature processes hinder integrating the nanofibers in various other technological domains, specifically CMOS compatible biosensor application which our group is targeting

to achieve. Alternatively conductivity can be enhanced by embedding nanofibers with MWCNTs. Researchers have successfully embedded nanotubes in various polymer derived nanofibers [9]. To the best of our knowledge, there is no report on enhancement of conductivity of SU-8 derived nanofibers using MWCNTs. This paper addresses the challenges involved in preparing these nanofibres.

2. Materials and methods

2.1 Materials

All chemicals were of the highest analytical grade, and were used without further purification. Aqueous Chloroform ($CHCl_3$) was obtained from Sigma-Aldrich. Standard multi-walled carbon nanotubes (MWCNTs) with diameter range of 5-20 nm used in this work were purchased from Reinste Nano Ventures Pvt. Ltd. (New Delhi, India). SU-8 (2015) was obtained from MicroChem Crop., USA. For photolithography, positive photoresist S1813 and its corresponding developer purchased from Shipley Inc, USA was used.

2.2 Preparation of Polymer Solutions

Initially MWCNTs 0.1% (w/v) were first prepared in 3:1Chloroform ($CHCl_3$) and sonicated for 30 min. Then 15 % (w/v) SU-8 (2015) was added to well dispersed MWCNTs in Chloroform solutions under vigorous stirring until uniform polymer solutions were attained

2.3 Preparation of copper microelectrode arrays

In order to perform electrical characterization of nanofibres it is essential that the fibers are positioned in between two conductive regions. Copper electrodes arrays were fabricated essentially for this purpose using standard lift off technique on a glass substrate. Patterning is a way to control the morphology/architecture of the electrospun fibers. The effect of collector geometry, particularly for the alignment of fiber, has been studied [8]. In present study we have used a mask aligner lithography system from SUSS Microtec Lithography GmbH. Germany. A schematic of the patterning process used in this study shown Fig. 1.

A glass wafer was cleaned by dipping in Acetone for 5 min following by a Isopropyl alcohol for 5 min. The wafer was dried using dry N_2 and then was put on a hot plate for 10 min at 120 °C in order to carry out dehydration Bake. Positive photoresist S1813 was spun on to this wafer at 500 rpm for 5 sec and 4000 rpm for 35 sec. The prebake was carried out on a hot plate at 95 °C for 60 sec. UV Exposure was carried out using mask aligner. After development, the wafer was loaded into the sputtering system (AJA instrumentation, USA.). 20nm of Ti was coated onto the wafer followed by 200nm of copper. Ti is used for the promotion of adhesion of copper to the glass substrate. To carry out the lift-off process, the processed wafer was dipped in Acetone solution and sonicated for 10 min. The wafer was then clean in Isopropyl alcohol for 5 min and then dried using dry N_2. The electrodes are of 100µm diameter and are separated by a distance of 50µm. Nanofibres were spun on this array using electrospinning process.

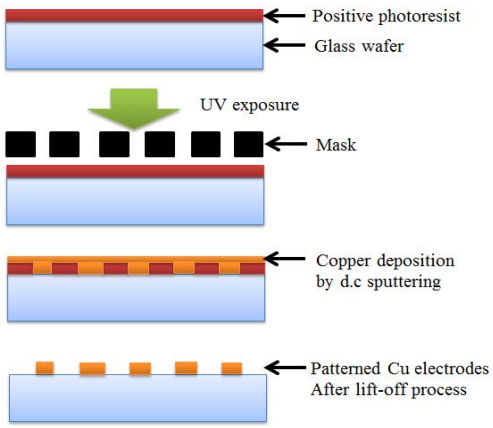

FIG.1. Schematic representing fabrication of micro-electrode array using lift off process.

2.4 Electrospinning of MWCNTs embedded SU-8 Fibers

The key challenge in this process is to spin a nanofibre between two electrodes of the microelectrode array. The electrospinning process parameters have to be optimized in order to achieve this goal. The key parameters are the voltage between the syringe and the collector, the distance between the syringe and the collector, the flow rate of the polymer solution and the time of deposition. The collector in this case is the patterned glass substrate.

Fig. 2a shows a schematic of the electrospinning method. The polymer solution was ejected from the syringe pump by the bias voltage applied between syringe and collector electrode. The polymer jet follows basically the field lines formed between two electrodes and is spread over the target surface. The electric current in the jet lines also plays an important role in determining the diameter of nanofibers [x]. Nanofibers formed on the surface of collector electrode were preferentially oriented along the winding direction, as shown in Fig. 2b. The degree of orientation could be evaluated by the electrical conductivity, as will be discussed below. The voltage was varied from 5 kV to 20 kV; the distance was varied from 5 cm to 20 cm. The flow rate was varied from 1 – 5 μL/h. The variation in flow rate was achieved using a microprocessor controlled motorized syringe pump.

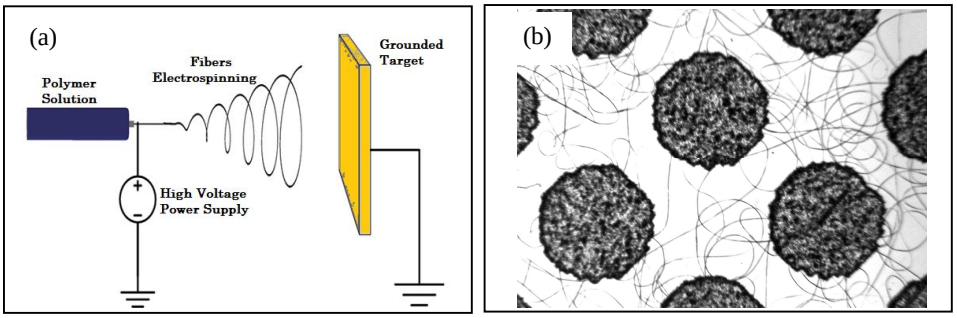

FIG. 2. (a) A schematic of electrospinning apparatus and (b) Microscopy image of microelectrodes array on partially aligned nanofibers that are electrospun.

In all experiments, the polymer solution was placed into a syringe for electrospinning. A high-voltage DC power supply was connected to a 25-gauge blunt-nosed needle attached to the syringe containing the electrospinning solution. The electrospun fibers were collected on a grounded copper plate covered with aluminum foil. Solutions were able achive a single fiber positioned between two electrode by applying a voltage of 16 kV, a tip-to-collector distance of 10 cm, and a solution flow rate of 3 μL/h and the deposition time was 3 sec. All of the electrospinning procedures were carried out at room temperature (~25 C) with a collection time of 10 min. Finally, the electrospun fibers on glass substrate copper microelectrode arrays were heat treatment in a hot plate at 200 C for 6 h to enhance the conductivity the trace solvent of fiber.

2.5 Characterization of MWCNTs embedded SU-8 nanofiber

Scanning electron microscopy (SEM) (Quanta 200, FEI, Frankfurt am Main, Germany; SUPRA 40 VP, Gemini, Carl Zeiss, Oberkochen, Germany) was used to observe the surface morphology of the nonwoven fiber meshes and to determine the range of diameters produced for all of the above studies. The electric conductivity of the single nanofiber was measured by using Cascade two-probe method, the current through the sample was measured with a Keithley's 4200 SCS. The sample was measured four times in different directions by applying the potential of -0.5 to +0.5 V and average value was calculated. XRD studies (X'Pert PRO) using Cu Kα radiation, were performed and Raman studies were carried on a Senterra inVia opus Raman spectrometer (Senterra, Bruker, UK) using 785 nm excitation and the optical power delivered onto the sample 50 mW/cm^2 were obtained for pure and composite MWCNTs embedded SU-8 derived fiber in order to change in the graphitic nature of the nanofiber as a function of the CNT weight fraction. And the wetting behavior of the MWCNTs embedded SU-8 nanofiber surfaces were before and after characterized by measuring static contact angles and contact angle hysteresis with a contact angle measurement (AST PRODUCTS.INC, VCA Optima). In most of the measurements, 5μL (~3-mm spherical drop diameter) water droplets were used.

3. Results and discussion

FIG. 3 illustrates the MWCNTs embedded SU-8 nanowire arrays over a relatively large area (few cm^2) as derived from polymer precursors on cylindrical geometries of the collector electrode arrays. Fig. 3a shows the SEM images of fabricated copper electrodes array. Fig. 3b shows a single nanofiber between two electrodes. Fig. 3c shows electrospun nanofiber material obtained from MWCNTs embedded SU-8 polymer solution. Fig. 3d Shows higher magnification image of 3c. The distortion in the electrode shape is due the low resolution printed sheet mask used for fabricating the array. The average diameter of the nanofibers was found to be of the order of 300 nm.

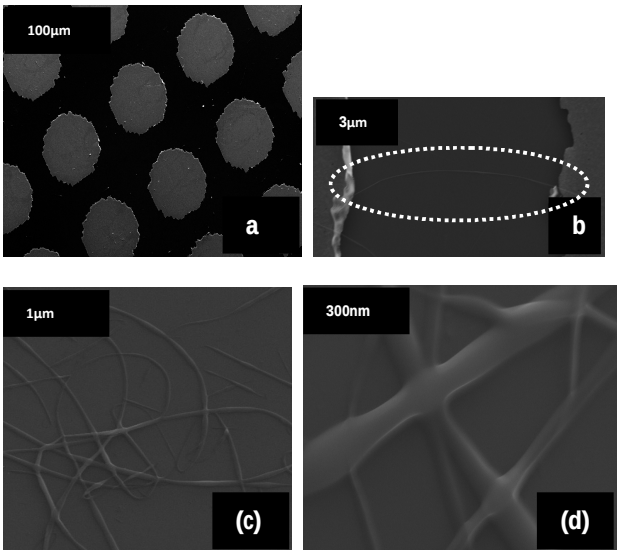

FIG.3. SEM images: (a) cylindrical geometry of Cu electrodes; (b) Single suspended nanofiber between two electrodes (c) electrospun material obtained from MWCNTs embedded SU-8 derived nanofiber; (d) higher magnification image of (c).

Fig. 4 summarizes the conductivity measurements performed on single suspended MWCNTs embedded SU-8 nanofiber before and after heat treatment process. As described earlier in the materials and methods section, polymer fibers were electrospun between two measuring electrodes made by a photopatternable mixture of SU-8 and MWCNTs. Fig. 4a and b shows the SEM images of an individual MWCNTs embedded SU-8 based nanofiber before heat treatment (average diameter 300 ± 10 nm) and after heat treatment (average diameter 280 ± 10 nm), respectively, suspended between the electrodes. I–V characteristics as shown in Fig. 4c were measured using two probes contacting the electrode posts. The linear behavior of I–V curve implies an ohmic contact between the electrodes and the suspended MWCNTs embedded SU-8 nanofiber. This is facilitated by a close integration of the wire with its base during heat treatment process to produce a carbon monolith. The testing voltage ranged from – 0.5 to 0.5 V, with step variations of 0.1 V. To ensure the repeatability of the results, the tests were repeated at least three times for a suspended nanofiber.

Table1. Summarizes the electrical properties obtained for suspended MWCNTs embedded SU-8 derived nanofiber before and after heat treatment, respectively. The conductance was calculated by measuring the slope of linear I–V curves. From the Table 1, we observe that electrical conductivity of a MWCNTs embedded SU-8 derived nanofiber before heat treatment was (5.54 ± 0.15) E -03 S/m. The conductivity of the MWCNTs embedded SU-8 derived nanofiber after heat treatment was calculated to be (73.8 ± 0.24) S/m, which is almost an order of magnitude less compared to that of MWCNTs embedded SU-8 derived nanofiber.

These results can be explained from Raman spectra indicate the carbon nanofibers to be of a polycrystalline nature, exhibiting broad D and G-band peaks at 1460 cm^{-1}, indicative of the fiber feature, and 1620 cm^{-1}, respectively (Fig. 4c). The small harmonic 2D peak (~2300 cm^{-1}) indicates that two phonon resonance conditions is achieved with the sample and confirms the crystalline nature of the MWCNTs derived nanofiber. However, the intensity and broadness of the D-band relative to the G-band indicate carbon nanofibers with a large amount of defects.

We also carried out XRD analysis to determine the enhancement in graphitization in MWCNTs embedded SU-8 derived nanofiber. The results are shown in fig. 5a. The broadening and increase in intensity of the peak at 2θ close to 24^0 for the 0 0 2 plane, and the graphitic peak for 0 0 4 plane at 2θ ~ 56^0 is much sharper which indicates better crystallinity in the case of the composite-MWCNTs embedded SU-8 derived nanofiber after heat treatment in comparison to the before MWCNTs embedded SU-8 derived nanofiber.

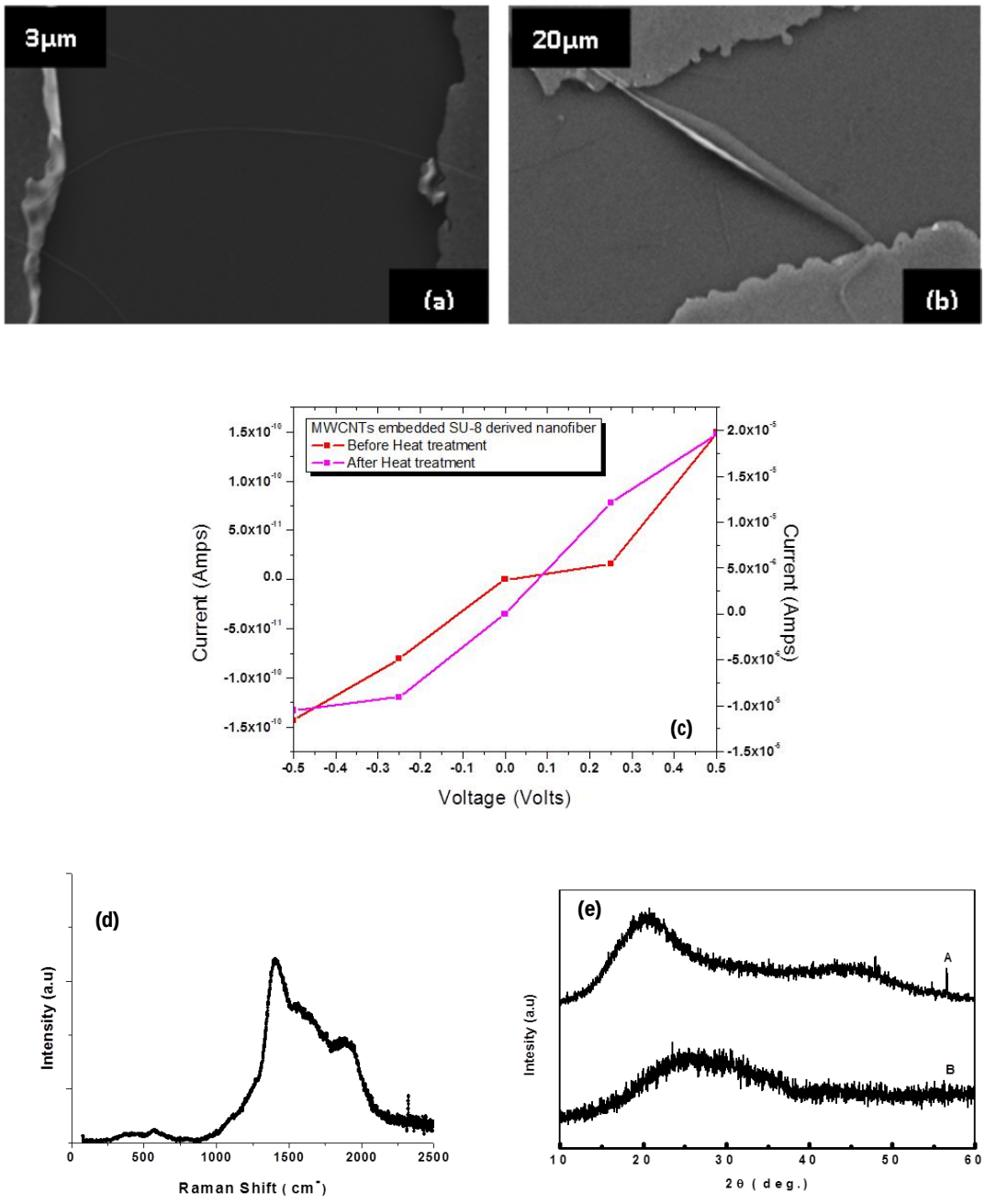

FIG. 4 – SEM images of single suspended nanofiber between two electrodes MWCNTs embedded SU-8 derived nanofiber (a) before heat treatment; (b) after heat treatment; (c) I–V curve for single suspended nanofiber for both cases; (c) Raman spectroscopy of MWCNTs embedded SU-8 derived nanofiber. (d) XRD spectra intensity for MWCNTs embedded SU-8 derived nanofiber of (A) after heat treatment (B) before heat treatment.

Table 1 – Electrical properties of suspended single nanofiber measured by I–V curve.		
Parameters	Samples	
	MWCNTs embedded SU-8 Nanofiber before heat treatment	MWCNTs embedded SU-8 Nanofiber after heat treatment
Length of the fiber (l) (μm)	55	55
Average diameter of the fiber (d) (nm)	300	280
Cross-sectional area of the fiber (A)(m^2)	16.5 E-12	15.4 E-12
Slope of I–V curve (conductance) (S)	6.5202 E-08	4.83 E-05
Resistivity (ρ) (ohm m)	180.04	13.55E -03
Conductivity (σ) (S/m)	5.54E -03	73.8007

To better understand the effects of MWCNTs embedded SU-8 derived nanofiber morphology on the surface roughness and thus on the wetting behavior of these fabrics, water contact angles (WCAs) was measured. Smooth films of SU-8 2015 photoresist was also prepared by spin coating at 3000 rpm and subsequent soft baking at 333 K for 20 min for comparison with the electrospun fabric. Smooth carbon films were obtained after UV exposure followed by low heat treatment at the same conditions as mentioned earlier.

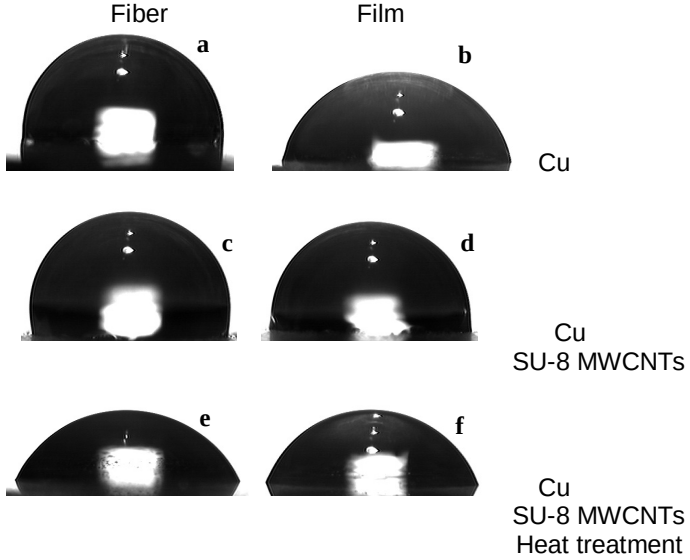

FIG. 5. Images of a water droplet on surfaces with various morphology and heat treatments: (a-b) Cu, (c-d) on Cu MWCNTs embedded SU-8-derived nanofiber, and (e-f) on Cu MWCNTS embedded SU-8 derived nanofiber after 6 hrs. Of low heat treatment. Morphology changes occurred in the following order (from left to right): fibers, and films. The drop volume was ~5μL for all samples.

Fig. 5. Shows images of water droplets on different surfaces (copper or MWCNTs nanofiber) with different morphologies, namely, fibers and smooth films, which are with and without surface treatment. The first row of images is for the Copper surfaces, the second row depicts untreated on copper MWCNTs embedded SU-8 derived nanofiber surfaces and third row is for the low temperature treated MWCNTs embedded SU-8derived nanofiber.

A smooth film of the Copper is weakly hydrophilic. The water contact angle of Copper smooth film increased slightly to 96.8° (±1.5°) (Fig. 5d) as compared to that of a Copper film, 85.7° (±1.2°) (Fig. 5b). There was a significant increase of the contact angle to 110.2°(±2.1°) (Fig. 5c) for copper MWCNTs embedded SU-8 fibers.

Thus, surface morphology and roughness were found to be important factors in controlling the wettability of the electrospun fibers. Interestingly, tailoring of the Cu MWCNTs embedded SU-8

nanofiber substrate morphology alone without any surface thermal modifications could control the wetting properties in a large ranges from mildly hydrophilic (<90°contact angle) on a smooth surface to nearly super hydrophobic on a film surface. There are only a few known instances of wettability transition across 90°contact angle with changing surface morphology.

The fact about the electrical conductivity of suspended MWCNTs embedded SU-8 derived nanofiber from low heat treatment process gives us another means of controlling the resulting suspended MWCNTs nanowires and this is vital for various applications. The versatility of this method not only makes it attractive tool for developing suspended nanowire array based electronic devices such as switches, memory elements but also for fabricating single nanowire based sensing devices. These MWCNTs embedded SU-8 derived nanofiber may, for example, be functionalized to interact with specific biomolecules. In all these cases conductivity, wire thickness, mechanical strength, etc. will be different.

4. Conclusions

The process described in this article to prepare MWCNTs embedded SU-8 derived nanofibers. Since there is a significant increase in electrical conductivity is achieved using a low heat treatment process. These nanofibers can potentially be used in impedance based or ISFET based biosensors by performing suitable surface functionalization based on the target analyte.

Acknowledgements

The authors wish to thank the Director, Indian Institute of Technology Hyderabad (IITH), India for encouragement.

References

[1] S. Ramakrishna, K. Fujihara, W. Teo, T. Lim and Z. Ma, World Scientific Publications **(2005)**.
[2] C. J. Buchko, L. C. Chen, Y. Shen, and D. C. Martin, *Polymer* 40,**(1999)** 7397.
[3] D. H. Reneker and I. Chun*, Nanotechnology* 7, **(1996)** 216.
[4] J. S. Kim and D. H. Reneker, *Polymer Eng. Sci.*39, **(1999)** 849.
[5] M. Bognitzki, W. Czado, T. Frese, A. Schaper, M. Hellwig, M. Steinhart, A. Greiner, and J. H. Wendorff, Adv. Mater. *(Weinheim, Ger.)* 13, **(2001)** 70.
[6] I. D. Kim and A. Rothschild, Polym. *Adv. Technol*, 22, **(201l)** 318.
[7] J. Moon, J. Park, S. Lee, and T. Zyung, *ETRI Journal*, 31, **(2009)** 636.
[8] C.S. Sharma, A. Sharma , M.J. Madou, *Langmuir,*26(4): **(2010)** 2218.
[9] C. S. Sharma, H. Katepalli, A. Sharma, M.J. Madou, *Carbon*, 49, **(2011)** 1727.
[10] C.X. Liu, J.W. Choi, *Nanomaterials*, 2, **(2012)** 329.
[11] Y.S. Lee, J. S. Im, , *InTech*, 6, **(2010)** 438.

Corrosion Study of Anodized Cobalt Oxide Nanotubes in Phosphate Solution

Zulkarnain Endut, Nor Akmaliza Rais, Nurulhaidah Daud, Ali Zaini Abdullah, Mohd Adam Mohd Noor, Nora'zah Abd Rashid

NEMS and Photonics Laboratory (NAPL), Industrial Electronic Technology, MIMOS Berhad, Technology Park Malaysia, 57000, Kuala Lumpur, Malaysia
Corresponding author. Tel No:+60199126114.
E-mail address: zulkarnain.endut@mimos.my

Abstract

In recent years, in situ monitoring of phosphate ion has remained a tremendous challenge in various applications such as aquaculture, agriculture, environmental and healthcare. Several analytical methods such as chromatography, optical fluorescent, colorimetric sensing and electrochemical methods are being developed to overcome the problem. However, better detection selectivity, stability, environmental insensitivity, miniaturization and operational simplicity have made electrochemical method as a better choice for field based monitoring of phosphate ion. In a potentiometric manner, cobalt is capable of sensing phosphate ion via a mixed potential corrosion mechanism. Mixed potential corrosion occurs when a nonequilibrium state exists at the electrode surface involving two or more electrochemical reactions. In this reaction, slow oxidation of cobalt and simultaneous reduction of both oxygen and Co^{2+} occur at the surface of the electrode. This paper describes electrochemical corrosion behavior of porous anodized cobalt oxide nanotubes in phosphate ion solution. The nanotubes were prepared by the electrochemical anodization method in fluoride containing electrolytes and were used directly as phosphate ion selective electrode. Based on the results, porous anodized cobalt oxide nanotubes responded well to different phosphate concentrations and better sensitivity towards phosphate was seen compared to compact anodized cobalt oxide.

Introduction

Phosphorus is an essential mineral for the human body and all other living organisms. Phosphorus level in fish ponds after fertilization could indicate plankton activities while excess phosphate levels in wastewater could impact water quality [1]. For soil engineering, monitoring phosphorus levels in soil during crop growth will have a significant impact on crop production yield [2]. However, a system that can be used for continuous monitoring and selective detection of phosphate levels in aqueous solution still has not been produced [1]. To date, the colorimetry method based on reagent [3] is still considered as a standard method for phosphate detection while measurement of phosphate levels in environmental water samples is usually achieved using laboratory-based automated flow apparatus [4].

Compared to chromatography, optical fluorescent and colorimetric sensing or other electrochemical methods like electrochromic devices and amperometric devices, electrochemical phosphate sensor using the method of potentiometry is a better choice for field based monitoring as it is more simply operated. In the literature, ion selective electrode (ISE) based phosphate sensors which are based on, for example, calixarene [5] or molybdenum acetylacetonate [6] have been used but they still give problems in terms of selectivity and stability.

To date, cobalt response towards phosphate ion has been studied using Co wire [7], Co rod [8] and Co electrodeposited thin film [9] but the effect of surface morphology such as porous surface has never been investigated in detail. Cobalt metal electrode was reported to have shown good potentiometric response and selectivity to dihydrogen-phosphate ion in an acidic medium [7,8]. According to the findings of Meruva and Meyerhoff [8], a Co-wire electrode responds well to hydrogen-phosphate and phosphate ions in different pH solutions. A Co-wire based hydrogen-phosphate ion sensor was discovered to have a low concentration detection limit and a broad detection range. A disposable on-chip hydrogen-phosphate ion sensor with planar cobalt microelectrodes on a polymer substrate was also discovered [10]. The sensing mechanism of the Co-based potentiometric sensor has still not been clarified but early findings mostly agreed that the mechanism is based on mixed potential corrosion.

Recently, Schmuki et al. [11] has created a new way to produce nanoporous cobalt oxide using the anodization method. In this method, cobalt was anodized in fluoride containing electrolyte such as in ethylene glycol and glycerol using DC supply in low temperature. As a result, nanoporous or nanotube cobalt oxide was obtained. Based on his study, the nanoporous cobalt oxide can be obtained by slowing

down the oxygen evolution kinetics. He used an electrolyte with a low but optimized water content and anodization is done at reduced temperature. Additionally, an optimized oxide dissolution rate through fluoride ion content and pH adjustment is needed to allow for self-organization. The nanoporous cobalt oxide can be considered similar to nanotubes because it contains nanotubular structure. This paper attempts to analyze the improvement that nanoporous cobalt offers in terms of its sensitivity towards phosphate ions. The discussion is based on the corrosion aspect of the cobalt materials using electroanalytical techniques. As for comparison, compact anodized cobalt oxide is used.

Experimental Procedures

Porous anodized cobalt nanotubes were grown using the same method as reported by Schmuki et al. which is by electrochemical anodization of cobalt foils (0.125 mm thick, 99.5% purity). Prior to anodization, the cobalt foils were ultrasonically cleaned in acetone and ethanol consecutively for 15 mins and rinsed with deionized (DI) water. The foils were anodized using a two electrode configuration connected to a DC power supply, with platinum used as the counter electrode. The distance between two electrodes was fixed at 2 cm for all experiments. The electrolyte is a mixed ethylene glycol and glycerol solvent (volume ratio of 1 to 3) containing 3 M H_2O and 0.54 M NH_4F at 50 V at 0 ^{o}C for 3 hours. After anodization, the samples were rinsed with DI water and annealed in a muffle furnace for 30 minutes at 350 ℃, operated at atmospheric pressure. Corrosion behavior of anodized cobalt were conducted in phosphate solution using a Potentiostat/Galvanostat model PGSTAT-302 N from Autolab (Netherlands), controlled by a USB_IF030 interface card and GPES software. The experiments were performed in a three electrode electrochemical cell at room temperature with Ag|AgCl as the reference electrode and platinum rod as the counter electrode. The as-prepared cobalt used as the binder-free working electrode had nominal surface area of 1 cm. The linear polarization was done in between – 0.3 V and – 0.6 V and cyclic voltammetry was scanned in between – 1.3 V to 0.3 V using a scan rate of 50 mV s^{-1}. Electrochemical impedance measurements were carried out at open circuit potential in galvanostatic mode by imposing a small amplitude sinusoidal perturbation of 5 mV peak to peak and in the 2 mHz – 50 kHz frequency range. Compact cobalt oxide layers were obtained via anodization of cobalt foil in 1 M KOH solution at 10 V for 1 min followed by heat-treatment in air at 350 ^{o}C for 30 minutes. Details of experimental procedures of cobalt anodization and their morphology and crystal structure can be found in Schmuki's paper [11].

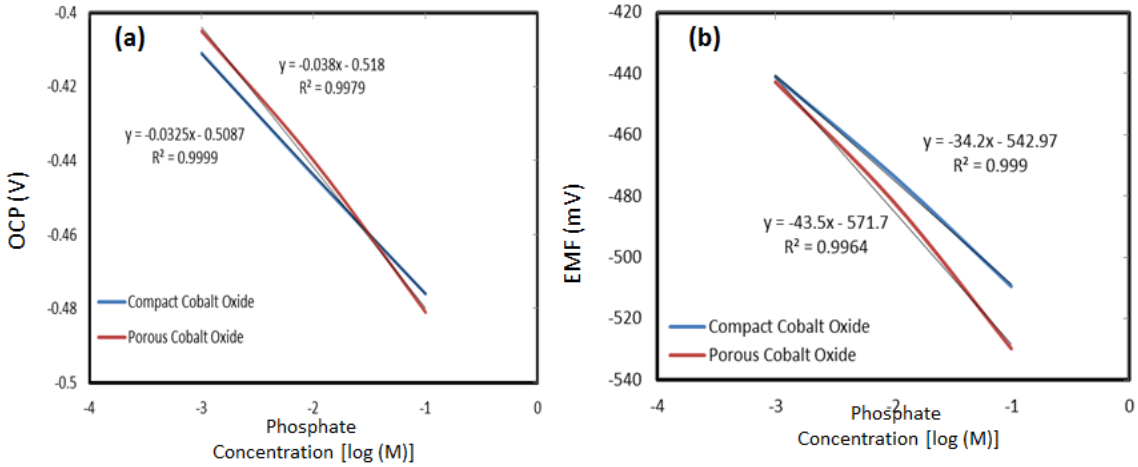

Figure 1 Sensitivity plots of anodized cobalt in phosphate solution at pH 4. (a) OCP measurement using linear polarization method, and (b) EMF measurement using Orion meter

Results and Discussions

The effect of surface area offered by anodized cobalt oxide nanotubes on its sensitivity towards phosphate ion were analyzed using EMF meter, cyclic voltammetry, linear polarization and electrochemical impedance spectroscopy. The results were compared with anodized compact oxide. Figure 1(a) and 1(b) show the sensitivity plot of anodized cobalt in different concentrations of phosphate

at pH 4. The sensitivity plots were taken from OCP values of linear polarization experiment (Figure 1a) and EMF values taken using Orion meter (Figure 1b). Porous anodized cobalt oxide showed superior sensitivity value up to – 43.5 mV/decade for sensitivity plot using EMF values (Figure 1b) compared to – 34.2 mV/decade obtained by compact anodized cobalt oxide using the same method. Sensitivity plot taken using OCP values (Figure 1a) also showed a similar trend. The sensitivity of porous anodized

Table 1 Comparison of sensitivity value for compact cobalt oxide and porous cobalt oxide

Sensitivity	Linear Polarization (mV/decade)	Orion Meter (mV/decade)
Compact Cobalt Oxide	32.5	34.2
Porous Cobalt Oxide	38.0	43.5

cobalt oxide obtained by OCP method is – 38 mV/decade compared with – 32.5 mV/decade for compact anodized cobalt oxide. Comparison of sensitivity value for both materials is summarized in Table 1. In terms of linearity, both materials have excellent R^2, more than 0.99 at linear region. Figure 2(a) and 2(b) are linear polarization plots for compact anodized cobalt oxide and porous anodized cobalt oxide, respectively in phosphate solutions at pH 4. From the plot, both materials show identical linear polarization plot response. The open circuit potential (OCP) value for higher concentrations of phosphate is located at the more cathodic region compared with lower concentration values. The more cathodic value indicates both materials will have larger corrosion rate [12] when exposed to higher concentrations of phosphate ion.

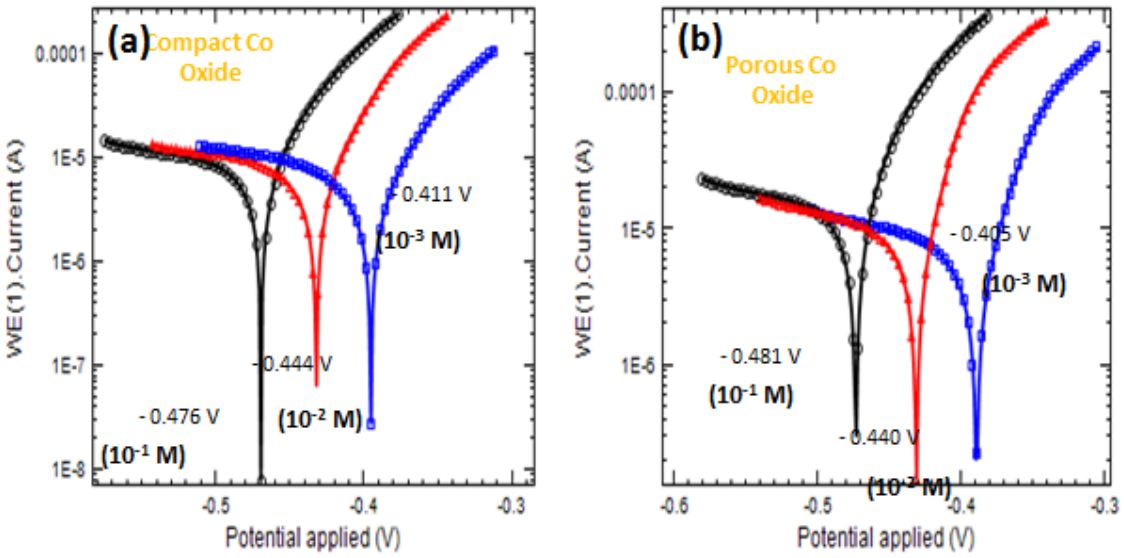

Figure 2 Linear polarization plots for compact anodized cobalt oxide and porous anodized cobalt oxide phosphate solutions at pH 4

Figure 3(a) and 3(b) are the cyclic voltammograms for compact anodized cobalt oxide and porous anodized cobalt oxide, respectively. Cyclic voltammetry (CV) is done in different phosphate concentrations to investigate the oxidation and reduction characteristics of cobalt that makes the OCP shift as found in linear polarization (Figure 2a and 2b). The CV is executed from -1.4 to 0.2 V vs Ag|AgCl using a scan rate of 50 mV/s. From the curves for both materials, the anodic wave seems to

start at approximately -0.4 Vs Ag|AgCl that indicates the oxidation of Co^0 to Co^{2+}. On the reverse scan, the cathodic wave at -1.1 V corresponds to the reduction of Co^{2+} to Co^0. The reduction and oxidation curves exhibited greater magnitude when exposed to larger concentrations of phosphate ion. By comparison, CV reduction peak at cathodic area for porous anodized cobalt oxide is larger than compact anodized cobalt oxide as shown in Figure 3(c). The larger reduction peak at the cathodic area for porous anodized cobalt oxide resulted in larger OCP values obtained in higher concentrations (10^{-1} M phosphate). As a result, a greater sensitivity plot for porous anodized cobalt oxide was obtained as shown in Figure 1 previously. Based on the CV results, the phosphate sensitivity of both cobalt materials are based on mixed potential mechanism. This mechanism happens as a result of a nonequilibrium state that exists at the electrode surface involving two or more electrochemical reactions. Usually, different oxidation and reduction reactions occurs on the electrode at the same time. The presence of species that alter the rate of cathodic or anodic reactions will modify the apparent electrochemical potential of the electrode as the algebraic sum of the partial currents for each reaction ($i_{cathodic} + i_{anodic}$) has to equal zero under open circuit conditions [8].

Figure 4 shows the impedance plots for both materials in phosphate solution for different concentrations. The impedance measurements were made at open circuit potentials in galvanostatic mode. There are two capacitive loops in all experimental conditions in the impedance plot or Nyquist plot of both materials. Between the two loops, the second loop seems to be bigger than the first, indicating that anodic polarization stimulates the formation and growth of the adsorbed species on the cobalt surface. The diameter of the second capacitive loop shifted at low frequency shows that the charge-transfer process kinetics is dependent on phosphate concentration. It is apparent that the decrease in charge transfer resistance is directly proportional to phosphate ion concentration, showing that the electrode reaction is aided by phosphate ions. The comparison of both Nyquist plots, either for

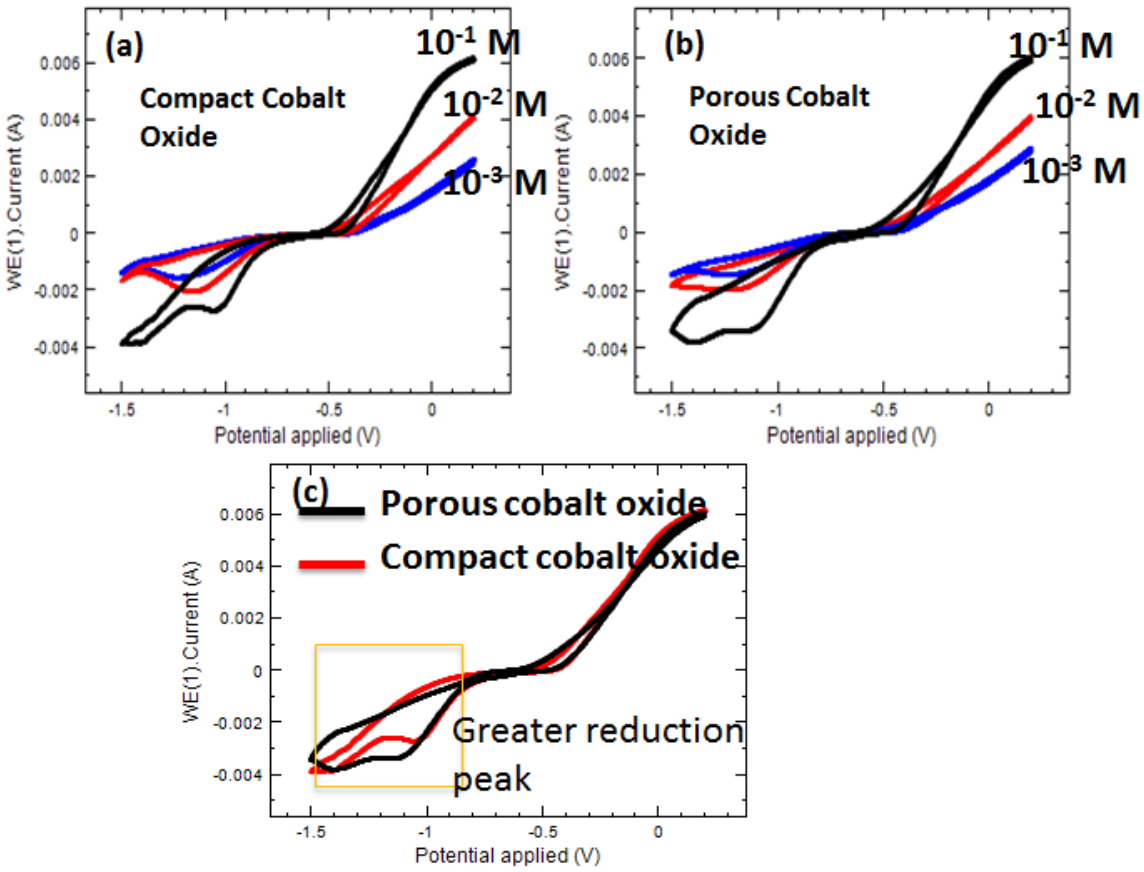

Figure 3. Cyclic voltammogram of anodized cobalt in phosphate solution at pH 4. (a) anodized compact cobalt oxide, (b) anodized porous cobalt oxide, and (c) comparison of compact and porous cobalt oxide for 10^{-1} M phosphate concentration.

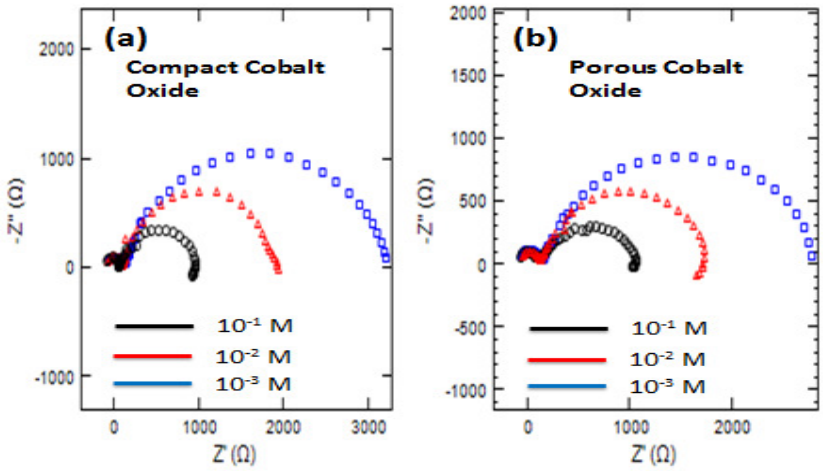

Figure 4. Nyquist plot of anodized cobalt oxide. (a) Compact cobalt oxide, and (b) Porous cobalt oxide

compact anodized cobalt oxide or for porous anodized cobalt oxide, both show similar charge transfer characteristics.

Conclusion

The corrosion behavior and sensitivity of porous anodized cobalt oxide was studied in phosphate solution and was compared with compact anodized cobalt oxide. The porous anodized cobalt oxide shows greater sensitivity towards phosphate ion either measured by the EMF method using Orion meter or OCP using linear polarization. The highest sensitivity slope obtained for porous anodized cobalt oxide is – 43.5 mV/decade. Based on the CV and linear polarization results, this superior sensitivity is due to greater surface area of porous electrode and greater reduction activity of porous cobalt oxide in phosphate solutions. As a result, OCP shifting will be more pronounced in porous electrode compared to compact electrode. However, the sensing mechanism and charge transfer characteristics of both materials are similar as shown in Nyquist plots and cyclic voltammograms.

References

[1] S. Berchmans, T.B. Issa, P. Singh, Analytica Chimica Acta 729 (2012) 7-20

[2] S.O. Engblom, Plant and Soil, 206 (1999) 173-179

[3] C. Warwick, A. Guerreiro, A. Soares, Biosensors and Bioelectronics 41 (2013) 1-11

[4] A.T. Law, S.B. Adeloju, Talanta 114 (2013) 191-203

[5] N.R. Modi, B. Patel, M.B. Patel, S.K. Menon, Talanta 86 (2011) 121-127

[6] M. Ganjali, P. Norouzi, M. Ghomi, M. Salavati-Niasari, Analytica Chimica Acta 567 (2006) 196-201

[7] D. Xiao, H.Y. Yuan, J. Li, R.Q. Yu, Analytical Chemistry 67 (1995) 288-291

[8] R.K. Meruva, M.E. Meyerhoff, Analytical Chemistry 68 (1996) 2022-2026

[9] W.H. Lee, Y. Seo, P.L. Bishop, Sensors and Actuators B: Chemical 137 (2009) 121-128

[10] J.H. Lee, W.H. Lee, P.L. Bishop, I. Papautsky, Journal of Micromechanical and Microengineering 19 (2009) 025022

[11] C.Y. Lee, K. Lee, P. Schmuki, Angewandte Chemie International Edition 52 (2013) 2077-2081

[12] W.A. Badawy, F.M. Alkharafi, J.R. Alajmi, Journal of Applied Electrochemistry 30 (2000) 693-704